UNIVERSITÀ DEGLI STUDI DI PADOVA

FACOLTÀ DI SCIENZE MM. FF. NN.

DIPARTIMENTO DI FISICA "G. GALILEI"

DOTTORATO DI RICERCA IN FISICA

XX ciclo

Heavy Flavours Production in DIS Events at HERA

Coordinatore: *Ch.mo Prof. Attilio Stella*

Supervisore: *Ch.mo Prof. Riccardo Brugnera*

Co-supervisore: *Ch.mo Dott. Alessandro Bertolin*

Dottorando: *Paolo Bellan*

31 Gennaio 2008

A mia madre

”Allora ho mirato tutta l’opera di Dio
e ho visto che l’uomo non può arrivare a scoprire
tutto ciò che si fa sotto il sole
anche se l’uomo si affatica a cercarne la spiegazione,
non può scoprirla
ed anche se il saggio pretende di saperla,
non può tuttavia conoscerla”.

Qo 8:17

”Distruggerò la saspienza dei sapienti
ed annullerò l’intelligenza degli intelligenti.
Non ha forse Dio dimostrato stolta
la sapienza di questo mondo?
Se qualcuno tra voi
si crede un sapiente in questo mondo,
si faccia stolto per diventare sapiente;
poiché la sapienza di questo mondo
è stoltezza davanti a Dio”.

1 Cor 1:19, 3:18

Riassunto

La misura effettuata in questa tesi concerne l'estrazione della percentuale di eventi in cui un *quark* pesante viene prodotto nel contesto di collisioni elettrone-protone profondamente anelastiche. L'insieme di dati analizzato, corrispondente a circa $130\ pb^{-1}$, è stato raccolto dal rivelatore ZEUS, situato in uno dei punti di interazione del collisore HERA ad Amburgo, durante l'anno 2005.
Le percentuali misurate sono direttamente collegate alla struttura del protone, descrivibile tramite il formalismo delle funzioni di struttura, ed in particolare di F_2. L'identificazione di eventi in cui si produce un *quark* pesante è avvenuta tramite il metodo del parametro d'impatto: la correlazione tra vita media degli adroni prodotti nell'adronizzazione dei *quark* pesanti e proprietà geometriche delle relative tracce consente infatti di distinguere la produzione di sapori pesanti dal fondo da *quark* leggeri.
L'utilizzo di questo metodo "topologico" ha previsto un massiccio impiego del rivelatore di Micro Vertice al silicio dell'esperimento ZEUS. Quest'essenziale componente del sistema di tracciameno del rivelatore ha costituito la principale miglioria realizzata nella seconda parte del periodo di presa dati dell'esperimento. Per il raggiungimento dell'obbiettivo fisico dell'analisi si ha fatto profondo affidamento sulle sue prestazioni e sulla sua affidabilità; pertanto una parte consistente del lavoro è stata rappresentata da studi di fattibilità, raffinamenti e successive ottimizzazioni.

Abstract

The estimation of the fraction of events in which an heavy quark is produced in the deeply inelastic electron–proton collisions is the measurement performed in the present analysis. The analysed data sample corresponds to about $130\ pb^{-1}$ collected during the years 2004-2005 by the ZEUS detector, located in one of the interaction points of the HERA collider in Hamburg.
The measured percentages are directly related to the proton structure, formally encoded by the contribution of the heavy quarks to the structure functions F_2.
The tagging of the events in which an heavy quark is produced is achieved by means of the Impact Parameter method. The correlation between the lifetime of the hadrons and the geometrical properties of the relative tracks makes possible to pick out the heavy flavours production form the background.
This kind of 'topological' method makes an extensive use of the silicon Micro Vertex Detector (MVD). This essential component of the tracking suite of the ZEUS detector has been the major upgrade realized in the second half of the ZEUS experiment data taking period. The achievement of the physical goal has strongly leaned on its performance and reliability, so a considerable part of the work consisted in feasibility, refinement and optimization studies.

Introduction

Experimental results in the field of High Energy Physics are currently interpreted in the framework of the *Standard Model* of particle physics (SM). This theory predicts matter to be made up of elementary constituents: *quarks* and *leptons*. Six kinds of quarks are present being different in virtue of the quantum number called *flavour*. From the lightest to the heaviest they are called: *up*, *down*, *strange*, *charm*, *beauty* (or *bottom*) and *top*. Six leptons exist as well, three being electrically charged, the *electron* (e), *muon* (μ) and *tau* (τ) and three being neutral (*neutrinos*: ν_e ν_μ ν_τ).

The formalism of the SM provides a unified description of the *electromagnetic* and *weak* forces. The strong forces are described by the part of the theory called *Quantum CromoDynamics* (QCD). Each interaction is mediated by specific particles called *vector bosons*, the massless *photon* and the massive W and Z^0 for the electro–weak force and the *gluon* for the strong force. QCD describes how quarks are bound together to form *hadrons*. The quarks are not detected as free particles but they are always bound with an antiquark to form *mesons* (as the *pion* or *kaon*) or with two other quarks to form *baryons* (as the *proton* and the *neutron*). The quark masses range from few MeV for the up quark to hundreds of GeV for the top quark. These values are not predicted by the SM.

All the particles needed by the SM have been detected by the experiments except the so called *Higgs boson* which is responsible for the generation of the mass. The search for this particle as well as other particles appearing in extensions of the SM is the main motivation for the collider with the highest centre–of–mass energy ever realized, the *Large Hadron Collider* at CERN in Geneva.

Ordinary matter is essentially composed by protons, neutrons and electrons. Protons and neutrons are built by *up* and *down* quarks. The *charm*, *beauty* and *top* quarks are generally called *heavy quarks*, since their mass is larger than the energy scale at which the quarks are confined into hadrons, $\Lambda \sim 250\,\mathrm{MeV}$. In nature at present, heavy quarks are only produced in high energy collisions, e.g. in the interactions induced by cosmic rays, and their existence is ephemeral. Hadrons containing heavy quarks are not stable. They decay very rapidly to lighter hadrons and leptons in about 10^{-12} s. Therefore, to study their properties they are produced in a controlled environment in which their decay products can be detected, e.g. particle accelerators and detectors.

Generally speaking, heavy quark production in deep inelastic scattering (i.e. at high virtualities of the exchanged photon) is calculable in QCD and provides information on the gluonic content of the proton which is complementary to that obtained from other measurements (as from the measurements of the scaling violation of the proton structure function). In addition, the scale of the hard scattering may be large relative to the mass of the heavy quark, thus allowing to study whether and when to treat the heavy quark as a massless parton.

Nowadays, heavy quarks are produced in several experiments of high energy physics. *Production* and *decay* properties of the heavy quarks are extremely interesting. Decays of both c and b-hadrons are used to measure the violation of CP symmetry, a combination of two symmetry transformations: the charge conjugation (C) which transforms a particle in its antiparticle and the parity (P) which is equivalent to reflection in space. Indeed two "factories" of B mesons, PEP II at SLAC (USA) and KEK B at KeK (Japan), have confirmed CP violation in the B system.

Heavy quark production also provides an excellent ground to test the predictions of QCD. This interesting aspect of heavy flavour physics is faced by this thesis: testing the different behaviour of beauty or charmed hadrons is the main way in order to get information about the reliability of the perturbative QCD calculations, on threshold effects and on highr order corrections. It is generally believed that the mass of the beauty quark, being around three times larger than that of the charm quark, allows perturbative QCD predictions to be more reliable. Due to a phenomenon called "asymptotic freeedom" the strong force becomes, in a certain sense, "less strong" in the presence of a large energy scale (the beauty quark mass in our case) and thus the mathematical approach used in the calculations is on a firmer ground.

In the last years the study of b-quark production has been an intriguing topic since several experiments at proton-antiproton ($p\bar{p}$) colliders (like UA1, CDF and D0) have measured production rates higher than those predicted by the most precise QCD calculations available. Similar measurements are also performed in $\gamma\gamma$ processes at electron-positron (e^+e^-) colliders (as LEP) and at the HERA electron-proton (ep) collider. Also in these very different environments QCD seems to be underestimating beauty production. As we will discuss in this dissertation, the correct description in terms of QCD of the b-quark production rate is still on its way towards a complete clarification.

The purpose of this dissertation is to perform an original measurement of beauty and charm quark production in ep collisions at HERA.

HERA (*Hadron Electron Ring Anlage*) was the first and so far only ep collider ever built. At the centre–of–mass energy available at HERA, $\sqrt{s} = 318$ GeV, the cross section for beauty production is much higher than at the previous fixed–target experiments, having centre–of–mass energies two orders of magnitude lower: there, beauty production could not be observed. Heavy quarks production in ep interactions proceeds through two main processes: *deep inelastic scattering*, where the virtuality of the exchanged photon goes from some GeV^2 to the kinematic limit of $10^5\ GeV^2$, and *photoproduction* processes, in which the exchanged particle is an almost real photon, whose virtuality has a mean value of $\sim 10^{-3}\ \mathrm{GeV}^2$.

The data sample used for this analysis corresponds to an integrated luminosity of $130\ pb^{-1}$ collected by the ZEUS experiment in a period between the end of year 2004 and year 2005.

***

This dissertation has the following structure.
In **Chapter1** we give an introduction to the theoretical background of the ep collisions, with particular emphasis on the theory of the heavy quark production in the contest of QCD and phenomenological model for the hadronisation. An overview of the main experimental results on heavy quark production at HERA will be also reported.

In **Chapter 2** the HERA collider and the ZEUS detector are presented, with particular attention to the detector components directly involved in this analysis: the inner tracking devices, the Calorimeter and the LUMI monitor, together with an illustration of the event generator structure and the detector simulation.

In **Chapter 3** the physics goal of this analysis is presented and the measurement technique are illustrated. The physical observables and the experimental tools to deal with are here described in details.

Chapter 4 illustrates the analysed data sample, in terms of data or Monte Carlo events. A brief description of the Monte Carlo event generators used in this work is also reported, highlighting features and settings for each of them. The selection criteria and the reconstruction methods for DIS events are then illustrated and motivated. Particular emphasis is put on the track quality requirements, since they play a fundamental role in the performed measurements. Finally, the agreement between data and Monte Carlo predictions is presented with some control distributions.

To the physical results is dedicated the whole **Chapter 5**. The fit techinque, its implementation, sensitivity and stability are described, then the main results of the analysis are reported together with the values obtained. The measured quantities are directly compared with an analogous result obtained with the D^* mesons, previously published by the ZEUS Collaboration. The different sources of systematic errors are also discussed.

Then, in **Chapter 6**, one finally summarizes what has been done and some conclusions are drawn.

Contents

Chapter 1

Theory

In this chapter the theoretical framework for this analysis will be described. Starting with a short introduction into the Standard Modelof particle physics the properties of electron proton scattering, in particular the deep inelastic scattering, will be characterized. An overview of QCD, the theory of strong interactions, will follow. The production of heavy quarks and its relevance as a precise test of QCD is outlined. Finally the experimental results concerning heavy flavour measurements will be reported

1.1 The Standard Model

The *Standard Model* (SM) [1, 2] of particle physics is a theory to describe the elementary particles and their interactions. In the SM, all matter is made out of two kinds of elementary particles: leptons and quarks and their anti-particles, spin-$1/2$ fermions. They are grouped into three generations. The leptons are: electron with electron-neutrino, muon with muon-neutrino and tau with tau-neutrino. The quarks are similarly ordered into up (**u**) and down (**d**), strange (**s**) and charm (**c**) and beauty (**b**) and top (**t**) (see Tab. 1.1).

	Generations			Interactions		
				el.magn.	weak	strong
Leptons	$\begin{pmatrix} e \\ \nu_e \end{pmatrix}$	$\begin{pmatrix} \mu \\ \nu_\mu \end{pmatrix}$	$\begin{pmatrix} \tau \\ \nu_\tau \end{pmatrix}$	-1 no	yes yes	no no
Quarks	$\begin{pmatrix} u \\ d \end{pmatrix}$	$\begin{pmatrix} c \\ s \end{pmatrix}$	$\begin{pmatrix} t \\ b \end{pmatrix}$	$+2/3$ $-1/3$	yes yes	yes yes

Table 1.1: *The fundamental particles in the Standard Modeland their interactions*.

These particles interact by three fundamental interactions, described by exchanges of (virtual) gauge vector bosons (see Tab. 1.3). Gravitation is not incorporated into the Standard Model.
The group structure of the Standard Model is

$$SU(3)_C \times SU(2)_L \times U(1)_Y, \tag{1.1}$$

where $U(n)$ denotes the group of all unitary $n \times n$ matrices and $SU(n)$ is the group of all unitary $n \times n$ matrices with determinant 1. The weak and electromagnetic interaction are unified in the gauge group $SU(2)_L \times U(1)_Y$. The masses of the exchange bosons of the weak interaction are described by a process called *spontaneous symmetry breaking*. The masses are [3]: $M_W = 80.43\,\text{GeV}$ and $M_{Z^0} = 91.19\,\text{GeV}$[1]. All charged particles can exchange virtual photons, the mediators of electromagnetism, described by *quantum electrodynamics* (QED). The strong force is described by *quantum chromodynamics* (QCD) as a $SU(3)_C$ gauge group. The charge of the strong force, denoted as *color*, is carried by the massless gluons. Each quark has a color state assigned, a linear combination of three colors

[1] in this thesis the convention $c = 1$ and $\hbar = 1$ is used, unless stated explicitely otherwise

	particle	mass/ MeV
quarks	u	1.5 to 4
	d	4 to 8
	s	80 to 130
	c	1150 to 1350
	b	4100 to 4400
	t	174300 ± 5100
leptons	e	0.51100
	μ	105.66
	τ	1777.0
	ν_e	< 0.003
	ν_μ	< 0.19
	ν_τ	< 18.2
bosons	γ	$< 6{\cdot}10^{-20}$
	g	0
	$W^\pm$	80425 ± 38
	Z^0	91188 ± 2

Table 1.2: *Masses of Standard Model particles*.

and anti-colors. Bare quarks are not seen experimentally, all particles observed are colorless doublets (quark and anti-quark) or triplets (three quarks). The doublets are called mesons, the triplets denoted as baryons [2]. If one of the quarks or gluons carrying color is, in a hard interaction, kicked out of the meson or baryon, quark anti-quark pairs are produced in order to keep the resulting particles colorless. Leptons do not carry any color and are not directly affected by the strong interaction. The weak interaction affects all quarks and leptons.

Interaction	boson	$Q_{\rm EM}$	related group	typical coupling
strong	8 g	0	$SU(3)_C$	1
el.magn.	γ	0	$SU(2)_L \times U(1)_Y$	10^{-2}
weak	Z^0	0	$SU(2)_L \times U(1)_Y$	10^{-6}
	$W^\pm$	1		

Table 1.3: *The fundamental interactions in the Standard Model. The strength of the interactions is given by their couplings at very low energies $E \ll m_p$.*

1.2 Kinematics of ep-scattering

In the Standard Model the interaction between particles like electrons and protons can be described by the exchange of a vector boson. In the case that the exchanged boson is a photon (γ) or a Z^0 the interaction is called neutral current scattering (NC); if the boson is a $W^\pm$ the reaction is called charged current scattering (CC) (Figure 1.1).

The four-momenta of the incoming and outgoing electron are denoted k and k' respectively, the momentum of the proton is denoted P. The exchanged boson has the four-momentum q, given by

$$q = k - k'. \tag{1.2}$$

The scattering is described by the following variables:

$$Q^2 = -q^2 \tag{1.3}$$

$$s = (k+P)^2 \tag{1.4}$$

$$y = \frac{P\cdot q}{P\cdot k}, \quad 0 \le y \le 1 \tag{1.5}$$

$$x = \frac{Q^2}{2P\cdot q}, \quad 0 \le x \le 1 \tag{1.6}$$

[2] also states of five quarks, called *pentaquarks* may have been observed [4].

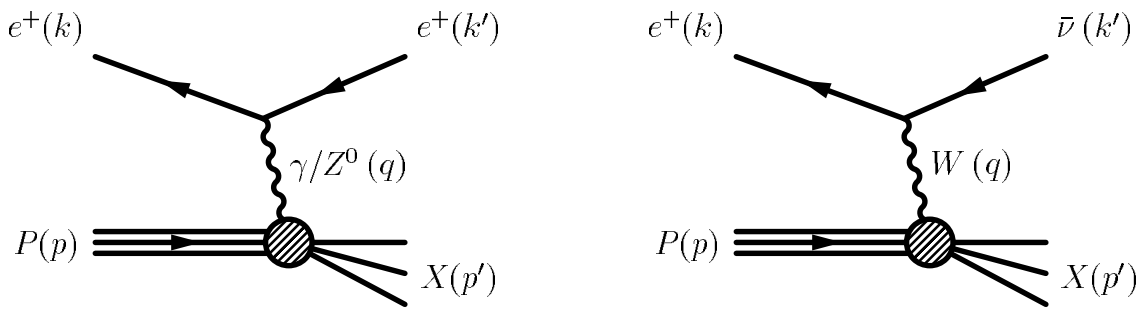

Figure 1.1: *Electron–proton scattering in Neutral Current (NC) (***Left***) and Charged Current (CC) (***Right***) processes. The four-vectors of the particles are indicated in parentheses.*

with Q^2 as the virtuality of the exchanged boson. s is the total center-of-mass energy squared, the *inelasticity* y describes the relative energy transfer from the lepton to the hadronic system in the proton rest frame. x is called *Bjørken scaling variable*. In the Quark Parton Model (see Sec. 1.3.2) x can be interpreted as the fraction of the proton momentum carried by the interacting parton. In the case the proton and electron masses are neglected Equation 1.4 and 1.5 can be simplified to:

$$s = (k+P)^2 \approx 2k\cdot P \tag{1.7}$$

$$y = \frac{P\cdot q}{P\cdot k} \approx \frac{2P\cdot q}{s} \tag{1.8}$$

$$\tag{1.9}$$

and the boson virtuality Q^2 can be expressed as the product of x, y and s:

$$Q^2 = sxy. \tag{1.10}$$

The center-of-mass energy $\sqrt{s}$ is fixed at HERA to a value of 318 GeV by the beam energies. Thus only two of the four variables are independent. The variable W, the invariant mass of the hadronic system recoiling against the scattered lepton, can be expressed as

$$W^2 = (P+q)^2 = P^2 + q^2 + 2P\cdot q \approx -Q^2 + ys. \tag{1.11}$$

Scattering processes are experimentally divided into two regions of phase space. Events with a virtuality of the exchanged photon $Q^2 \approx 0$, i.e. quasi-real photons, are classified as *photoproduction* (PHP) events. Events of Q^2 above a few GeV^2 and $W^2 \gg m_P^2$ (with the proton mass m_P) are referred to as *deep inelastic scattering* (DIS).

1.3 Deep Inelastic Scattering

This thesis focuses on heavy flavour production in *neutral current deep inelastic scattering* (NC DIS). The term *deep* refers to $Q^2 \gg m_P^2$, whereas *inelastic* means $W^2 \gg m_P^2$. The process can be seen as the probing of an object (the proton) with very short wavelength (of the photon) to detect very small details (quarks and gluons) of the object. The Q^2 range at HERA up to about $40000\,\mathrm{GeV}^2$ is equivalent to a resolution of $1/1000$ of the proton radius, applying $\lambda \approx \hbar c/\sqrt{Q^2} = 10^{-18}\,\mathrm{m}$.

1.3.1 InclusiveDIS cross section

The inclusive cross section for NC DIS can be expressed as a function depending on Q^2 and x [5]:

$$\frac{d^2\sigma_{NC}}{dxdQ^2} = \frac{2\pi\alpha_{em}^2}{xQ^4}\left[\tilde{F}_2(1+(1-y)^2) + x\tilde{F}_3(1-(1-y)^2) + y^2\tilde{F}_L\right] \tag{1.12}$$

$\tilde{F}_2(x,Q^2)$, $\tilde{F}_3(x,Q^2)$ and $\tilde{F}_L(x,Q^2)$ are generalized *Structure Functions*, which include coupling constants, propagator terms and Structure Functions for exchange of γ, Z^0 and γZ^0 interference terms respectively. For CC DIS similar equations can be derived. The *Structure Functions* F_i are functions of the variables x and Q^2 describing the distribution of electrical charge within the proton. The unpolarized cross sections for NC and CC DIS, differentiated in x and y are [3]:

$$\begin{aligned}\frac{d^2\sigma_{NC}}{dxdy} &= \frac{4\pi\alpha_{em}^2}{xyQ^4} \\ &\left[\left(1-y-\frac{x^2y^2M^2}{Q^2}\right)F_2^{NC} + y^2xF_1^{NC} \mp \left(y-\frac{y^2}{2}\right)xF_3^{NC}\right] \qquad (1.13)\\ \frac{d^2\sigma_{CC}}{dxdy} &= \frac{4\pi\alpha_{em}^2}{xyQ^4}(1\pm\lambda^2)\frac{1}{2}\left(\frac{G_FM_W^2}{4\pi\alpha_{em}}\frac{Q^2}{Q^2+M_W^2}\right)^2 \\ &\left[\left(1-y-\frac{x^2y^2M^2}{Q^2}\right)F_2^{CC} + y^2xF_1^{CC} \mp \left(y-\frac{y^2}{2}\right)xF_3^{CC}\right] \qquad (1.14)\end{aligned}$$

where α_{em} is the fine structure constant and G_F the Fermi constant. The charged current Structure Functions F_1^{CC}, F_2^{CC} and F_3^{CC} are the result of $W^\pm$ exchange. The neutral current Structure Functions F_1^{NC}, F_2^{NC} and F_3^{NC} are determined by photon and Z^0 exchange and by their interference. The Z^0 exchange, or $W^\pm$ for CC, is suppressed

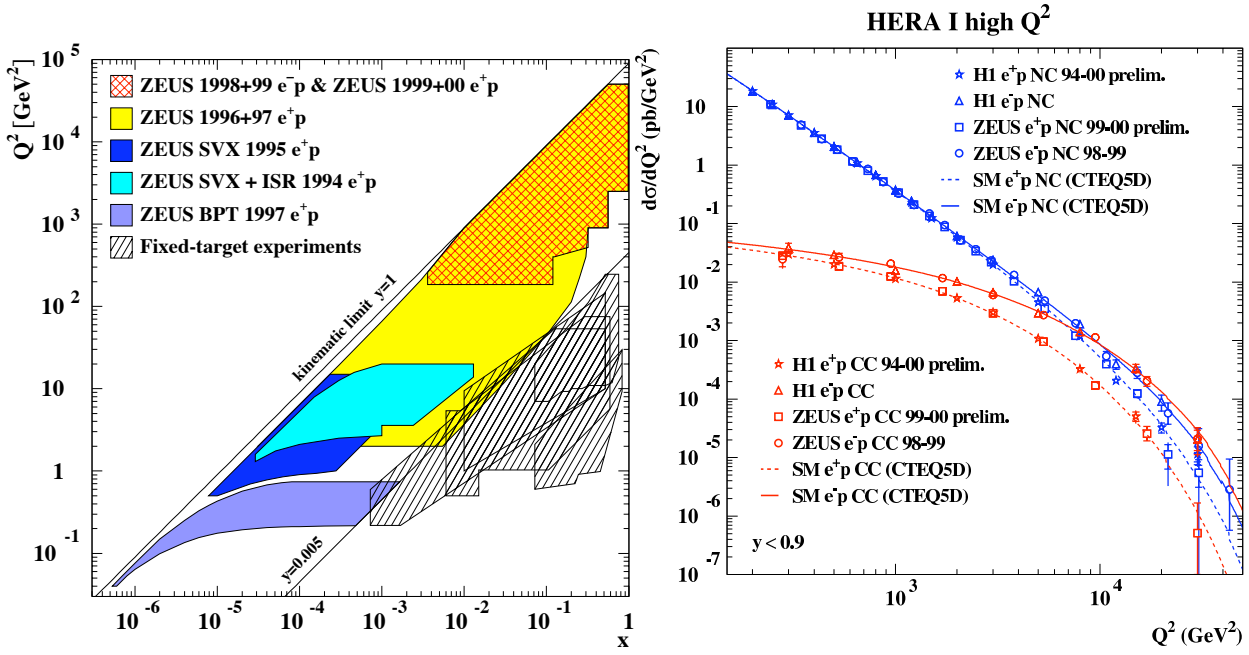

Figure 1.2: **Left**: *(x,Q^2) plane covered by HERA in comparison to fixed target experiments. The coverage of x and Q^2 is extended by about two orders of magnitude.* **Right**: *Neutral Current and Charged Current cross sections as a function of Q^2 from the ZEUS and H1 collaborations [6].*

relative to the γ exchange for Q^2 lower than the squared mass of the exchanged boson:

$$\frac{\sigma(Z^0,W^\pm)}{\sigma(\gamma)} \sim \left(\frac{Q^2}{Q^2+M_{Z^0,W^\pm}^2}\right)^2 \tag{1.15}$$

with M_{Z^0} and $M_{W^\pm}$ as the mass of the Z^0 and $W^\pm$ respectively. In this Q^2 regime the photon mediated NC DIS process dominates, the term $x\tilde{F}_3$ in Equation 1.12 becomes negligible and $\tilde{F}_2$ can be reduced to the electromagnetic Structure Function F_2^{em}. Without the small contribution of longitudinal polarized photons, included in the term $y^2\tilde{F}_L$, the cross section becomes:

$$\frac{d^2\sigma^{NC}}{dxdQ^2} = \frac{2\pi\alpha^2}{xQ^4}\left[F_2(x,Q^2)(1+(1-y)^2)\right]. \tag{1.16}$$

1.3.2 Quark Parton Model

A simple model, useful to understand many aspects of deep inelastic scattering, is the *Quark Parton Model*. In 1969 two models, the *Quark Model* [7] and the *Parton Model* [8] were developed to describe the proton. In the Parton Model the constituents of the proton are quasi-free point-like *partons*. The momentum of the proton p is carried by the partons: $p_i = \xi_i \cdot p$, where ξ_i $(0 \leq \xi_i \leq 1)$ is the fraction of total proton momentum carried by parton i. In this model the DIS cross section is the incoherent sum of elastic scattering processes of the electron off the partons:

$$\frac{d^2\sigma}{dxdQ^2} = \sum_{i=\text{partons}} e_i^2 \cdot f_i(x,Q^2)\left(\frac{d^2\sigma_i}{dxdQ^2}\right). \tag{1.17}$$

where e_i is the charge of parton i and $f_i(x,Q^2)$ is the probability of probing parton i carrying a momentum fraction between x and $x+dx$ in the proton. A prediction of this model is the independence of the proton structure of Q^2. This effect is called *scale invariance* and was predicted by Bjorken [9]. Only three partons are constituents of the proton in the Parton Model, even at higher momentum transfer no new substructure of the proton becomes visible. In the high Q^2 limit ($Q^2 \to \infty$) but x finite, referred as *infinite momentum frame*, the partons can be considered massless and all transverse momenta are negligible. In the proton infinite momentum frame, the interactions between partons can be ignored, due to the Lorenz time dilatation. The other partons do not participate in the hard interaction and are called *spectator partons*. In this model the Structure Functions $F_{1,2}$, are functions of x (the Bjørken scaling variable) but not of Q^2. In this frame x can be interpreted as the longitudinal momentum fraction of the proton ξ carried by the interacting parton.

The identification of quarks as the partons of the Parton Model, led to the Quark Parton Model (QPM). In the QPM $F_{1,2}$ can be expressed as a sum of quark and anti-quark densities. They are related to each other by the Callan-Gross relation [10]

$$F_2 = 2xF_1. \tag{1.18}$$

This equation was experimentally confirmed at SLAC [11] and it proved that the charged partons of the proton are spin $1/2$ particles (for spin 0 the prediction $2xF_1/F_2 = 0$ leads to an inconsistency with the data).

The Structure Functions are not yet calculable from first principles but have to be measured in experiments. The QPM predicts the independence of the Structure Functions from the virtuality of the photon Q^2 at high energies and that $F_{1,2}$ depends only on the scaling variable x. Later the violation of this prediction was found (see Fig. 1.7). Only about half the momentum of the proton is carried by the *valence quarks*. Valence quarks are the three quarks (uud) in the proton, mentioned earlier. For $x \ll 0.1$ the Structure Functions increase for increasing values of Q^2. This behavior was later explained by quantum chromodynamics (QCD).

1.3.3 Quantum Chromodynamics

In the theory of QCD the quarks can not be treated as free particles, but they exchange gluons. QCD is a renormalizable non-Abelian gauge theory, describing the strong interaction as exchange of gluons. The gluons and the quarks couple via color charges. Each quark or anti-quark holds one of the three colors or anti-colors respectively. The symmetry of QCD is therefore $SU(3)$. 8 independent linear combinations of color-anti-color exist, represented by 8 different gluons.

Perturbative QCD (pQCD) offers a method to calculate cross sections as power series in the coupling constant of the strong interaction α_s. The 0-th order are QPM-like processes. Higher orders include gluon and quark loops, called *virtual corrections* (see Fig. 1.3).

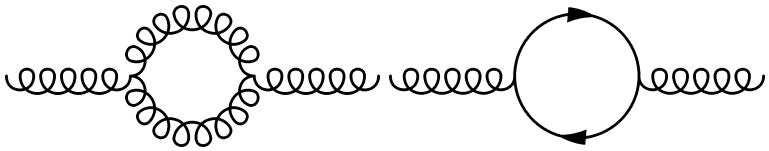

Figure 1.3: *One-loop corrections to the gluon propagator.*

To calculate cross sections, integration over the full phase space of virtual and real quarks and gluons is needed. This integration introduces divergencies caused by infinite momenta of the virtual particle loops, referred to as *ultraviolet divergencies*. The soft or collinear emission of massless gluons, causes *infrared divergencies*.

To remove these divergencies, first a procedure called *dimensional regularization* introduces additional dimensions ε to the integration. In a second stage, a procedure called *renormalization* replaces divergent integrals by finite expressions. This procedure introduces a new mass μ, the *renormalization scale*. All measurable quantities of the final state particles have to be independent of the choice of the arbitrary scale μ. Thus an effective coupling "constant" $\alpha_s(\mu)$ depends on the scale μ [3]:

$$\mu \frac{\partial \alpha_s(\mu)}{\partial \mu} = 2\beta(\alpha_s). \tag{1.19}$$

The β-function is a perturbative expansion in α_s, covering the dependency of α_s on the scale μ^2:

$$\beta(\alpha_s) = -\frac{\beta_0}{4\pi}\alpha_s^2 - \frac{\beta_1}{8\pi^2}\alpha_s^3 - \ldots \tag{1.20}$$

with

$$\begin{aligned} \beta_0 &= 11 - \frac{2}{3}n_f, \\ \beta_1 &= 51 - \frac{19}{3}n_f. \end{aligned}$$

n_f is the number of quark flavors with a mass lighter than the scale μ. The solution of Eq. 1.19 in the first order of α_s is:

$$\alpha_s(\mu) = \frac{12\pi}{(33 - 2n_f)\ln(\mu^2/\Lambda^{n_f}_{\mathrm{QCD}})}. \tag{1.21}$$

$\Lambda^{n_f}_{\mathrm{QCD}}$ is the scale of QCD and represents the energy at which α_s becomes large and perturbative QCD is not longer valid.
Figure 1.4 shows the dependence of α_s on the scale μ. The rise of α_s for small values of μ corresponds to soft

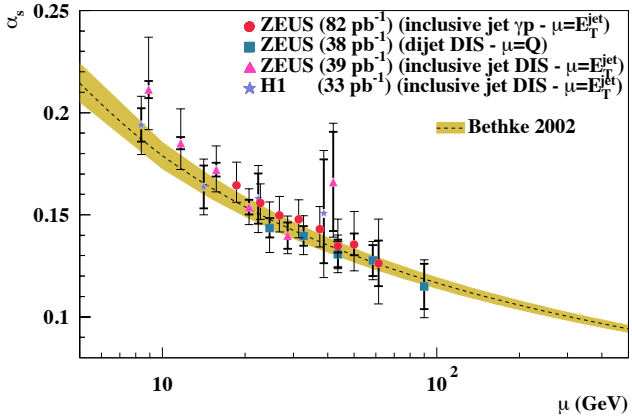

Figure 1.4: *Running of α_s with the scale μ measured at* HERA. *The data are compared with* QCD *predictions (shaded band) [12].*

interactions and large distances. At large scales $\mu \to \infty$ the value of α_s vanishes and the quarks are quasi-free. In this region of *asymptotic freedom*, perturbative QCD is applicable. The region of soft interactions has to be treated in a different approach.

1.3.4 Factorization

Factorization is the separation of the ep-scattering process into two parts. One part is the hard process, the interaction of high energy particles, the second is the long range part of low energy processes. The hard process is calculable by pQCD. The low energy part is not covered by pQCD. The Structure Function F_2 can be expressed as the convolution of a perturbative part, the *coefficient functions* (C_2^i) and the non-perturbative *parton density functions* (PDFs) $f_i(\xi, \mu_f, \mu)$. The PDFshave to be measured experimentally, while the coefficient functions are calculable. The factorization introduces a scale μ_f defining the boundary between the perturbative and the non-perturbative regime. The $f_i(\xi, \mu_f, \mu)$ are the probabilities of finding a parton i with a proton momentum fraction ξ (see Fig. 1.5):

$$F_2 = \sum_{i=parton} \int_x^1 C_2^i \left(\frac{x}{\xi}, \frac{Q^2}{\mu^2}, \frac{\mu_f^2}{\mu^2}, \alpha_s(\mu) \right) f_i(\xi, \mu_f, \mu) d\xi. \tag{1.22}$$

The evolution of the PDFsin μ is described by the Dokshitzer-Gribov-Lipatov-Altarelli-Parisi equations [14, **?**] or

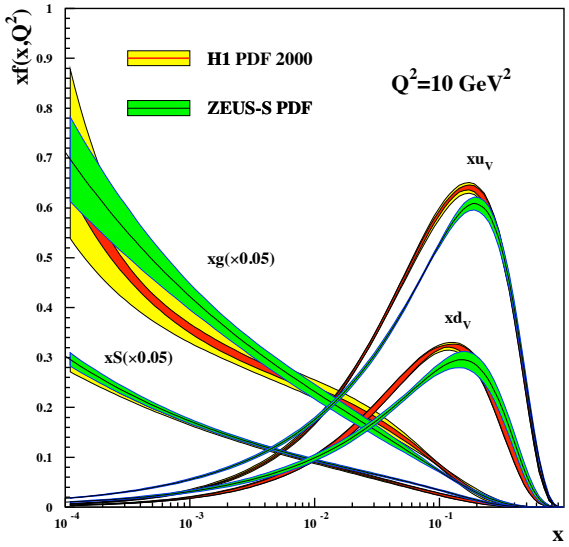

Figure 1.5: *Parton density functions [13] of the valence u and d quark, the gluons and the s quark content of the proton.*

DGLAP equations. They have the form:

$$\frac{df_{q_i}(x,Q^2)}{d\ln(Q^2)} = \frac{\alpha_s(Q^2)}{2\pi} \int_x^1 \frac{d\xi}{\xi} \left[P_{qq}(x/\xi) f_{q_i}(\xi, Q^2) + P_{qg}(x/\xi) f_g(\xi, Q^2) \right] \tag{1.23}$$

$$\frac{df_g(x,Q^2)}{d\ln(Q^2)} = \frac{\alpha_s(Q^2)}{2\pi} \int_x^1 \sum_i \frac{d\xi}{\xi} \left[P_{gq}(x/\xi) f_{q_i}(\xi, Q^2) + P_{gg}(x/\xi) f_g(\xi, Q^2) \right] \tag{1.24}$$

The functions $P_{ba}(x/\xi)$ are the DGLAP *splitting functions*. They describe the probability of a parton a to emit a gluon or quark and become parton b carrying a fraction $z = x/\xi$ of the momentum of parton a:

$$P_{qq}(z) = \frac{4}{3} \left[\frac{1+z^2}{1-z} \right] \tag{1.25}$$

$$P_{gg}(z) = 6\left[\frac{1-z}{z} + \frac{z}{1-z} + z\,(1-z)\right] \quad (1.26)$$

$$P_{q\bar{q}}(z) = \frac{1}{2}(z^2 + (1-z)^2) \quad (1.27)$$

The emission of soft gluons causes problems, because P_{qq} and P_{gg} diverge for $z \to 1$. An upper but-off z_{max} solves this issue. Although pQCD can predict the evolution of the PDFsfrom the scale μ_0 to any other scale, a measurement at a particular μ_0 is required to derive values at other scales μ.

As mentioned before, the Structure Functions can be expressed as a power series in α_s. The series contain terms of $\ln \mu^2$ and $\ln(1/x)$. The leading $\ln \mu^2$ term emerges from the evolution along the chain of partons, emitted from the quark before entering the hard interaction with the photon (see Fig. 1.6). By construction, the chain is strongly ordered in transverse momenta, i.e. $\mu^2 \gg k_{t,n}^2 \gg k_{t,n-1}^2 \gg ...$ where k_t denotes the transverse momentum of the parton in the nth position in the ladder. The leading-order (LO) sums up all $\alpha_s \ln \mu^2$ terms. The next-to-leading order (NLO) sums up terms of $\alpha_s(\alpha_s \ln \mu^2)^{n-1}$. This is important, if the construction of a strongly k_t ordered ladder is not an appropriate approach. Problems with this method emerge at very low values of x, due to the $\ln(1/x)$ terms.

A different approach is followed by the Balitsky-Fadin-Kuraev-Lipatov (BFKL) equation [16]. The $\ln(1/x)$ terms are important in particular in the low x regime. The BFKL equation sums up $\alpha_s(\ln(1/x))^n$, coming from strong ordering in x at leading order (LO).

The attempt of a unification of the DGLAP evolution, based on Q^2 ordering, and the BFKL evolution, based on ordering in x, led to the development of the Ciafaloni-Catani-Fiorani-Marchesini [17] (CCFM) evolution equations.

However so far the measurements show no significant evidence of deviations from the DGLAP equations. Figure 1.7 shows inclusive HERA F_2 data in excellent agreement with with DGLAP-based NLO QCD fits.

1.4 Heavy quark production

The production of heavy quarks, like the charm or the beauty quark, can not easily be explained in the naïve picture of the QPM. The mass of the proton is lower than the mass of the heavy quark ($m_c \approx 1.35\,\text{GeV}$ and $m_b \approx 4.4\,\text{GeV}$[3] [3]) and no heavy quarks on their mass shell can be constituents of the proton. The lowest order process of heavy quark production is the boson-gluon-fusion (BGF) (see Fig. 1.8).

This process ($\gamma^* g$) can produce a pair of quark and anti-quark if the center-of-mass (CMS) energy squared $\hat{s}$ of the photon-gluon system exceeds the squared mass of the $q\bar{q}$-pair:

$$\hat{s} = (\gamma^* g)^2 = (q + \xi P)^2 > (2m_{q,heavy})^2, \quad (1.28)$$

with the mass of the heavy quark $m_{q,heavy}$ and the four-vectors γ and ξP of the photon and gluon respectively. The high quark mass sets a hard scale for the process and a reliable description by pQCD calculations should be possible, e.g. demonstrated by the low value of the running coupling α_s at a scale corresponding to heavy flavour mass (see Fig. 1.4). Thus the heavy quark production is an excellent test of pQCD. Furthermore heavy flavor measurements provide insights into the gluon contribution of the proton, due to the dominating photon-gluon production process. Two kinematic regions can be distinguished for heavy quark production. In the region of $Q^2 \leq (2m_{q,heavy})^2$, BGF is the lowest order production process of a quark, anti-quark pair of mass $2m_{q,heavy}$. For high $Q^2 \gg (2m_{q,heavy})^2$ the splitting of a gluon into a virtual $q\bar{q}$-pair can be reinterpreted to occur inside the proton and the QPM picture is applicable for the production mechanism. In Figure 1.9 ep-scattering processes up to order α_s are symbolized by Feynman diagrams. The leading order processes in ep-scattering are QPM-like events. In addition virtual corrections to this process have to be taken into account. The next process shown is BGF, the dominant process of heavy quark production at low to medium Q^2. The radiation of a gluon before or after the scattering is called QCD *Compton-scattering* (QCDC).

[3] estimated in the $\overline{\text{MS}}$scheme

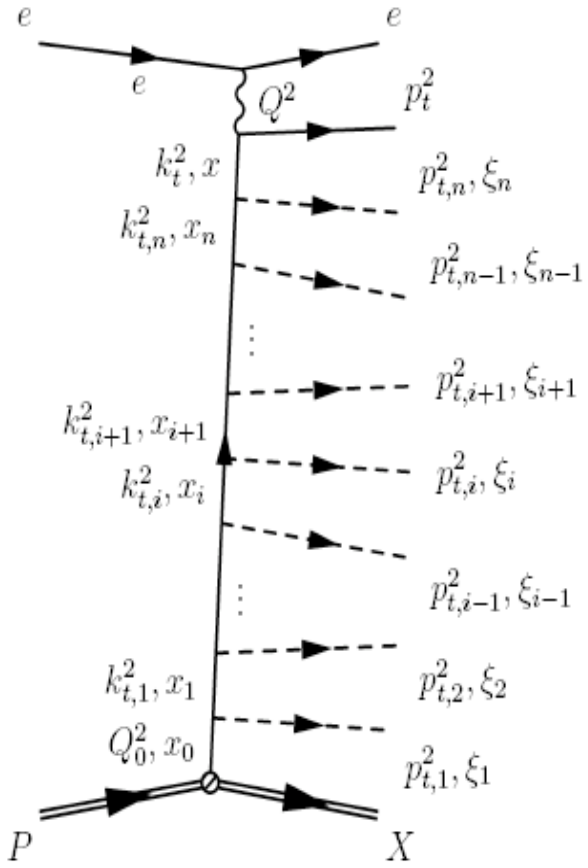

Figure 1.6: *Diagram of the k_t-ladder. A quark from the proton interact with a virtual photon from the electron after radiating n partons (dashed lines). Each parton is characterized by a longitudinal momentum fraction x_i and a transverse momentum $k_{t,i}$. Strong ordering corresponds to $Q^2 \gg k_{t,n}^2 \gg k_{t,n-1}^2 \gg ... \gg k_{t,1}^2$.*

1.4.1 BGF cross sections

The cross section of the production of a heavy $q\bar{q}$-pair in BGF can be calculated [18]:

$$\hat{\sigma}_{\mathrm{BGF}} = \frac{\pi e_b^2 \alpha \alpha_s}{\hat{s}} \left[(2 + 2\omega - \omega^2) \ln \frac{1+\chi}{1-\chi} - 2\chi(1+\chi) \right], \tag{1.29}$$

where e_b denotes the electromagnetic charge of the beauty quark, ω and χ are defined as

$$\omega = \frac{4m_b^2}{\hat{s}}, \quad \chi = \sqrt{1-\omega}. \tag{1.30}$$

In the same way the charm cross section can be calculated using the charm mass and charge respectively. The production of charm is favored with respect to beauty production due to the different charge and mass of b and c quarks. At the energy of the HERA collider, the beauty quark is mainly produced near the mass threshold. In this kinematic region the cross section of beauty quark production is about two orders of magnitude lower than the charm cross section.

1.4.2 Resolved photon process

For low Q^2, the exchanged photon is quasi-real and the probability to fluctuate into a quark, anti-quark pair is significant. The processes where a part of the hadronic structure of the photon interacts with a gluon from the proton are referred to as *resolved processes* (see Fig. 1.10). The strict definition of resolved processes is only possible at LO

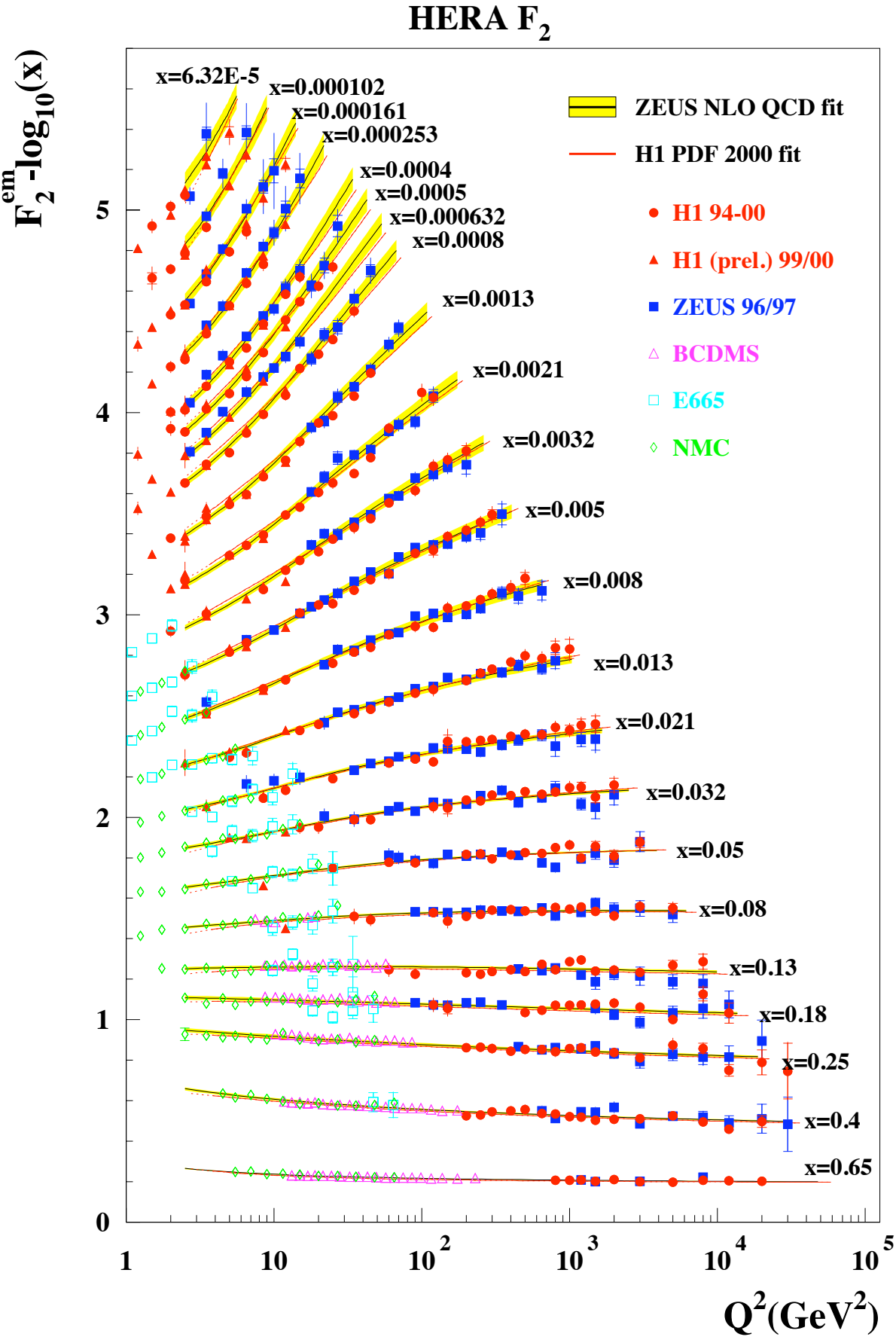

Figure 1.7: *Dependence of the proton Structure Function $F_2^{em}(x, Q^2)$ on Q^2 at different values of x measured at* HERA *and fixed target experiments. While the Structure Function is constant in Q^2 for high values of x, it is rising with Q^2 at lower x values, denoted as* scaling violation.

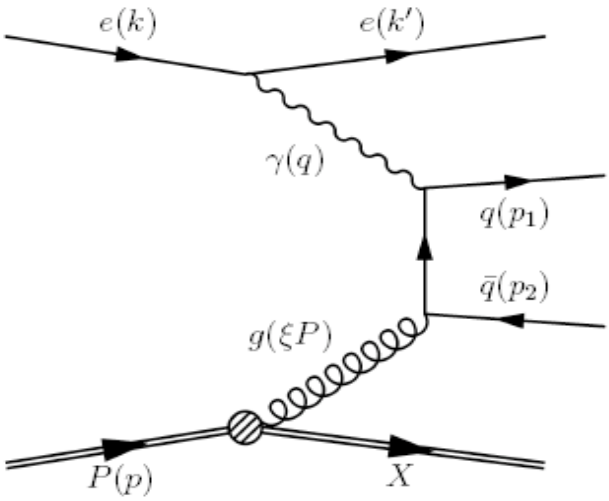

Figure 1.8: *Boson-gluon-fusion. At low Q^2 the lowest order mechanism to produce heavy quarks in ep-scattering*

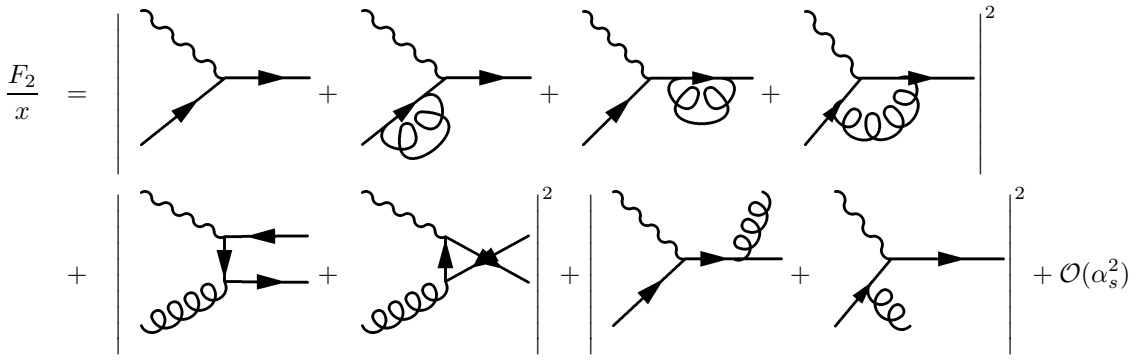

Figure 1.9: *Feynman diagrams of processes contributing to F_2 up to $\mathcal{O}(\alpha\alpha_s)$. The diagrams in the upper line are the* QPM *diagram and virtual corrections. The* BGF *contribution is shown in the lower left while* QCDC *graphs are shown on the lower right.*

QCD. At NLO, the definition depends on the technical implementation (see also Fig. 1.14). The point-like process (Fig. 1.10, left) is suppressed by the high mass of the heavy quark, whereas adron-like events contribute significantly to the cross section of heavy quarks production in PHP. In DIS, hadron-like events are suppressed due to the high virtuality of the exchanged photon.

1.4.3 Next-to-Leading order processes

Perturbative QCD calculations of heavy quark production are available also in next-to-leading order (NLO). The NLO contributions to the cross section are found to be significant. Feynman graphs of real corrections, emission of gluons, are given in Figure 1.11. In Figure 1.12 virtual corrections, contributing to the interference term with LO, are shown. Two conceptually different calculation approaches can be distinguished

massive scheme : In the massive scheme, only light quarks and gluons are considered as active initial state partons. In the perturbative expansion of the hard scattering cross section $\hat{\sigma}$ all terms up to $\mathcal{O}(\alpha_s^2)$ are taken into account (fixed order approach). This method is reliably applicable in the phase space region where the transverse momentum p_t of the heavy quark is less than or similar to its mass. This scheme is thus particularly relevant for the low Q^2 region.

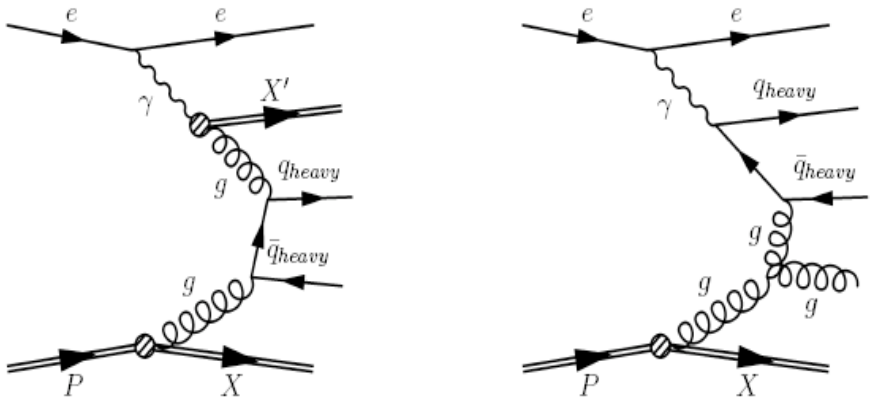

Figure 1.10: *Gluon-gluon-fusion in resolved processes. Resolved hadron-like event (left) and point-like (right) in heavy quark production.*

massless scheme : For $p_t \gg m_q$ (or $Q^2 \gg m_b^2$), large terms proportional to $\ln(p_t^2/m_q^2)$, accounting for collinear gluon emission from a heavy quark and gluon or photon splitting into a heavy $q\bar{q}$-pair, might spoil the convergence of the perturbation series. In so called *resummed calculations*, these contributions are included also beyond $\mathcal{O}(\alpha_s^2)$. Technically, this can be achieved by absorbing the heavy quark associated collinear singularities into fragmentation functions and PDFs. As this requires to set the quark mass to zero, this approach is denoted *massless scheme*. In contrast to the massive scheme, where the heavy flavors can only be produced dynamically in the hard subprocess, the massless approach treats the heavy quarks as intrinsic photon and proton constituents, which can appear in the final state through heavy quark excitation processes.

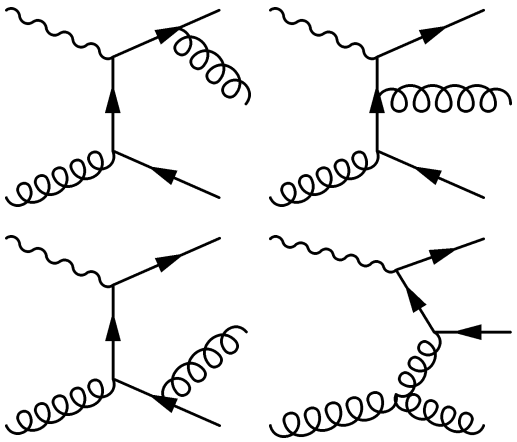

Figure 1.11: *Real* NLO QCD *contributions to heavy quark production*

1.5 Hadronization

As a consequence of the color confinement in QCD, the colored partons have to form colorless hadrons. The transformation of strongly interacting particles to hadrons is referred to as *hadronization* or *fragmentation*. The usual approach is to use *event generators* to model this process explicitly. The fixed order hard subprocess is calculated using QCD. The radiation of additional partons before and after the hard subprocess is perturbatively calculable (see Fig. 1.13).

The production of hadrons from these *parton showers* has to be treated in a non-perturbative step using phenomenological *hadronization models*. Both stages are described in the following sections.

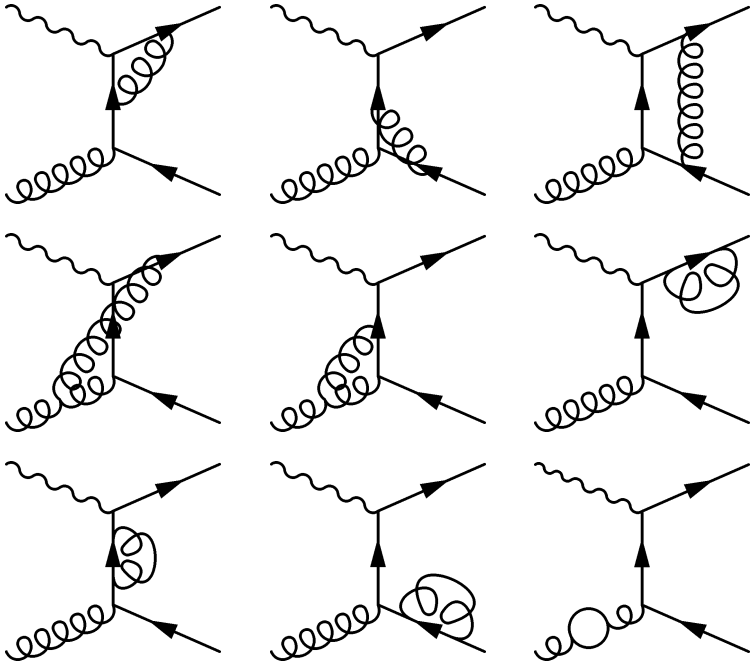

Figure 1.12: *Virtual* NLO QCD *contributions to heavy quark production*

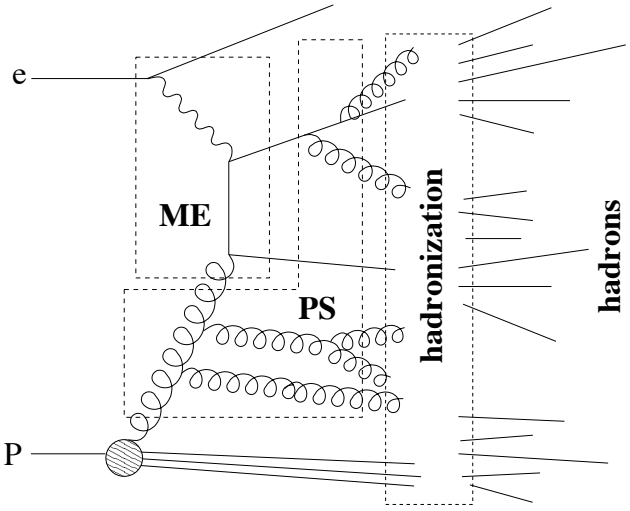

Figure 1.13: *Elements of the hadronization process as they are simulated in some Monte Carlo generators. The matrix element (ME), the parton showering (PS) and the hadronization are sketched.*

1.5.1 Parton shower

The parton shower (PS) approach models the evolution equation as a sequence of particle branchings $a \rightarrow bc$. The probability that one of these branchings occurs depends on the corresponding splitting function and the virtuality of the initial and final state partons. The parton shower algorithm starts from a parton of the proton and models the radiation of space-like parton showers until the parton reaches the hard subprocess. The Q^2 of radiated partons is ordered, going towards lower values. Any parton with positive virtuality can be the starting point of a time-like shower. Showers before the photon vertex and after the vertex are separated, neglecting any interference. The branching sequence is stopped when the virtuality of the outgoing partons reaches a cut-off value. Usually this cut-off is chosen to be 1 GeV ^{2}. Below this value pQCD becomes unreliable.

A distinct assignment of a process to LO plus parton shower or NLO is not always possible. As shown in Figure 1.14, the LO plus PS model simulates higher order processes, for instance NLO, in the parton showering.

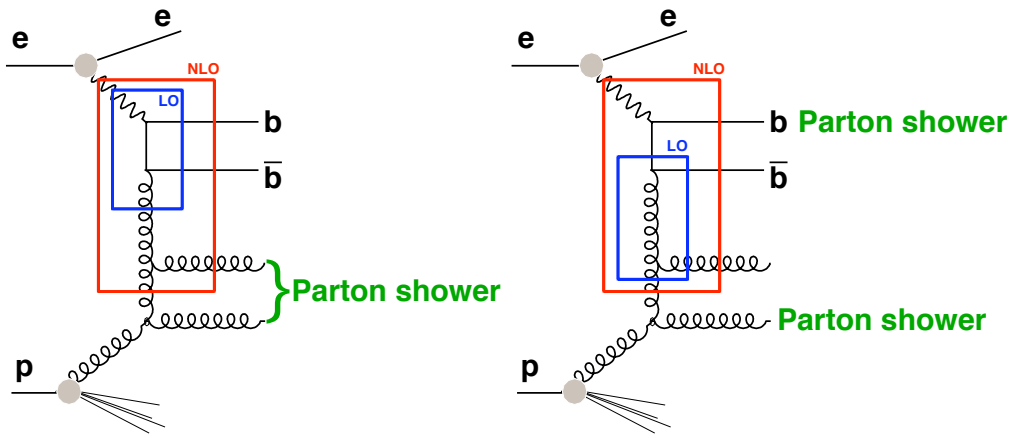

Figure 1.14: LO, NLO *and PS in heavy quark production. A part of the parton shower applied to initial and final state partons in* LO *plus PS is part of the hard scatter in* NLO *[19].*

1.5.2 Hadronization models

The hadronization models are phenomenological models to describe the formation of hadrons from partons. The two main hadronization models used in event generators are the *independent fragmentation* and the *string model*.

Independent fragmentation: The partons from the parton cascade fragment in this model independently. Each parton i transforms to a hadron h carrying a fraction of the longitudinal momentum z of the parton, characterized by *fragmentation functions* $D_i^h(z)$. The transverse momentum of the hadrons is assumed to be distributed Gaussian around the parton momentum. The additional quarks and anti-quarks needed to form the hadron are produced as $q\bar{q}$-pairs until the available energy is spent (see Fig. 1.15, left).

String fragmentation: In the string model the color dipoles of $q\bar{q}$-pairs form *color strings*. As the partons get separated, the string is pulled apart until the energy stored in the string is sufficient to produce a quark/anti-quark pair (see Fig. 1.15, right). The energy in the string rises proportional to the distance of the $q\bar{q}$-pair. This process goes on until the string energy is too low to form additional particles. The string fragments are combined into hadrons using fragmentation functions $D_i^h(z)$.

A widely used fragmentation function is the *Peterson fragmentation* [20]:

$$\mathcal{D}_q^h(z) \propto \frac{1/z}{(1 - 1/z - \epsilon/(1-z)^2)}. \tag{1.31}$$

ϵ has to be determined by measurements, while the value of ϵ depends on the treatment of parton showering. For beauty quark production ϵ has been extracted from a fit of B mesons in e^+e^- collisions [21] to be $\epsilon = 0.0033$. For charm fragmentation the ϵ is significantly higher at $\epsilon = 0.040$. Thus the fragmentation function for charm peaks at lower values of z, i.e. the fragmentation of beauty quarks is *harder* (see Fig. 1.16).

The *Lund string model*, used by MC involved in this analysis, combines the string fragmentation with the *Lund fragmentation function* [22].

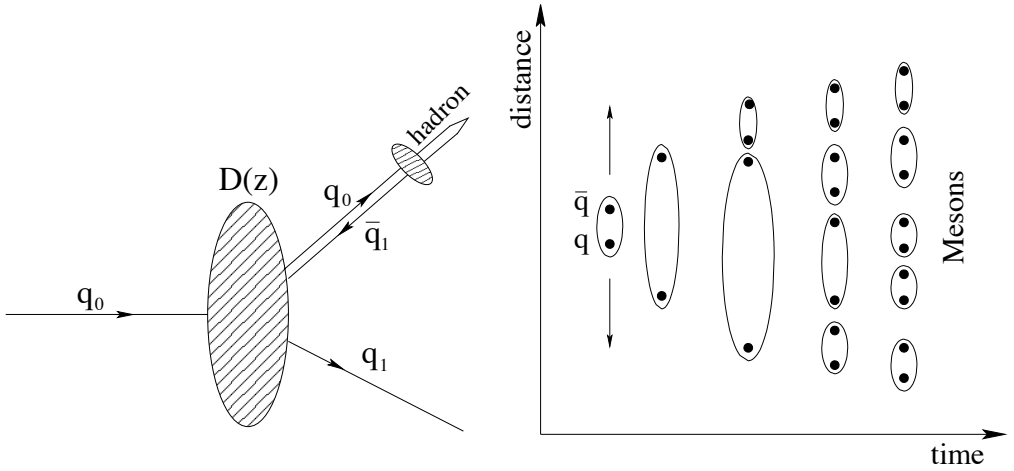

Figure 1.15: *Parton fragmentation models: independent fragmentation (left) and the string model (right).*

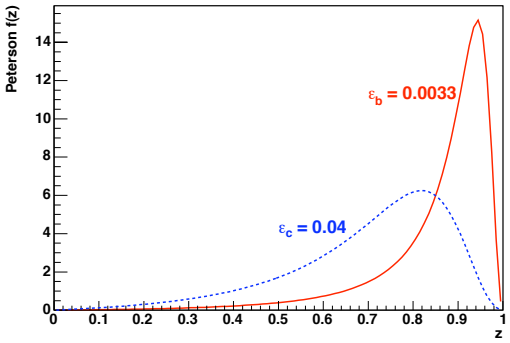

Figure 1.16: *Shapes of the Peterson fragmentation functions for charm (dotted line) and beauty (solid line) quarks. The beauty fragmentation function peaks at higher values of z.*

1.5.3 Jets

According to the hadronization, each strongly interacting final state parton from the hard subprocess results in a group of outgoing hadrons. In high-energy processes, where the momentum of the original parton is sufficiently high, these hadrons form a collimated flow of particles, called *jet*. Each jet is usually geometrical well separated from the other final state particles.

A strict correspondence of partons to jets is in general spoiled by higher order QCD processes and fragmentation connecting also particles originating from different partons. Nevertheless the jet topology is expected to reflect important properties of the underlying partonic process. In order to exploit this feature using observables based on jets, it is necessary to have a well defined procedure to group final state particles into jets. Furthermore, a rule has to be given to construct a jet momentum from the corresponding set of particle momenta, called *recombination scheme*.

Jets are not considered fundamental QCD objects and the jet structure depends on the reconstruction method used. To be able to compare jet observables with pQCD predictions, some theoretical aspects have to be considered. Results based on jet variables should be *collinear* and *infrared safe*, i.e. safe against collinear radiation or emittance of soft partons. The jet topology should be closely correlated to the partonic final state and *hadronization corrections*, connecting observables on hadron level with the corresponding parton level quantities, are preferred to be small.
The coefficient functions C_2^i, introduced by factorization (see Sec. 1.3.4), depend on Bjørken x and the momentum fraction ξ of the parton involved in the hard interaction only via the ratio x/ξ. Thus they are calculable at parton level without reference to the incoming hadron momentum. The jet algorithm should not destroy this dependency.

The algorithm used in this analysis, the k_t-algorithm [23] meets these requirements. The jet algorithm is Lorentz invariant, so it is possible to use not only the laboratory frame but the *Breit frame* to combine particles to jets.

1.6 The charm and beauty structure functions

The structure functions more frequently studied (F_2 and xF_3) are inclusive objects and thus contain contributions from both valence and sea quarks. The H1 and ZEUS detectors have the ability to provide identification of a particular quark flavour opening so the possibility of studying the contribution of that flavour to F_2. This is particularly important in the case of heavy flavours, as they are likely produced in the hard scattering and not in the subsequent hadronisation of the struck parton. In other words very precise theoretical predictions can be done as explained in the previous theoretical sections. Due to the fact that at order α_s heavy quark production in DIS occurs through boson-gluon fusion process, this process involves the gluon density xg directly so it gives an experimental handle on this quantity.

1.6.1 Charm production: tagging methods

The main method used for charm tagging is the identification of the D^* mesons using the decay channel $D^{*+} \rightarrow D^0 \pi_s^+$ with the subsequent decay $D^0 \rightarrow K^- \pi^+$, where π_s refers to the low momentum π in the decay. The decay particles of the D^* meson are reconstructed in the central detector, usually without particle identification. In Fig. 1.17 it is shown a distribution of the mass difference $\Delta M = M(K\pi\pi_s) - M(K\pi)$ from the ZEUS Collaboration. A clear signal is seen around the nominal value $M(D^*) - M(D^0)$. In order to mantain under control the combinatorial background, various cuts are made on the p_t of the tracks and on the energy of the event. Of course also other charmed hadrons were identified and analyzed, such as D^+, D_s, Λ_c, but with less statistics. Finally, the sistematic use of the vertex detectors, first implemented in H1 and now also in ZEUS, is changing dramatically the perspective of the physical analysis in the charm sector as it already happened in the beauty one.

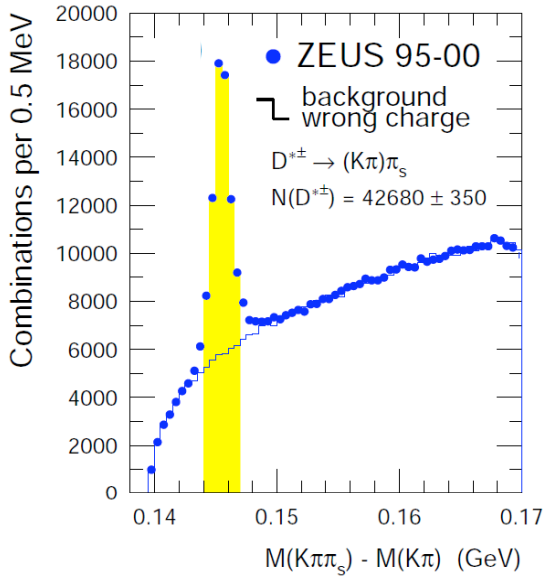

Figure 1.17: *The distribution of the mass difference, $\Delta M = M(K\pi\pi_s) - M(K\pi)$, for D^* candidates. The $D^{*\pm}$ candidates (dots) are shown compared to the wrong charge combinations (histogram). The shaded region shows the signal region. The number of D^* mesons is determined by subtracting the wrong charge background.*

1.7 Beauty production: tagging methods

The H1 and ZEUS Collaborations have presented measurements in which the events containing beauty are identified in the following manners: using high p_T leptons (mainly muons) from semileptonic b-decays, or using the impact parameters of all tracks coming from secondary decay vertices (inclusive lifetime tag analysis), or finally using double tagged events ($D^* + \mu$, $\mu\mu$).

In the first method, the transverse momentum p_T^{rel} of the muon with respect to the axis of the associated jets exhibits a much harder spectrum for muons from b-decays than for the other sources. Sometime, in order to enhance the signal to noise ratio also the signed impact parameter δ of the muon track with respect to the primary event vertex is used, this quantity reflects the lifetime of the particle from which the muon decays. The relative contributions from b, c and light quarks are determined by a fit to the p_T^{rel} distribution or to a combined fit to the p_T^{rel} and δ distributions using the shapes of Monte Carlo b, c and light quarks distributions as templates.

In the second method, the track selection requires full silicon vertex detector information. From the measured impact parameter δ a lifetime significance $S = \delta/\sigma_\delta$ is calculated. Two independent distributions are constructed. S_1 is the significance distribution of tracks in events with exactly one selected tracks. S_2 contains the significances of the tracks with the second highest significance for events with two or more selected tracks. Events in which the tracks with the first and second highest absolute significance have different signs are removed from the S_2 distribution. The subtracted significance distributions are obtained by bin-wise subtraction of the numbers of entries on the negative side from those on the positive side. The subtraction method substantially reduces the systematic uncertainties due to track and vertex resolutions. The relative contributions from b, c and light quarks are determined from a fit to the subtracted S_1 and S_2 distributions and the total number of events, using the shapes of Monte Carlo b, c and light quarks distributions as templates.

In the third method, doubled tagged events, events are selected containing at least one reconstructed D^* and at least one muon, $D^* + \mu$, or two muons in the final state ($\mu\mu$). In order to suppress the various types of backgrounds the charge and angle correlations of the D^* with respect to the muon and of the two muons are exploited. These double tagged measurements extend to significantly lower centre-of mass energies of the $b\bar{b}$ system than measurements based on leptons and/or jets with high transverse momentum. Furthermore, these double tagged events permit to test higher order QCD effects. For instance, in the photon-gluon rest frame the angle between the heavy quarks is 180 ^{o} at leading order, but at NLO it can differ significantly from this value due to hard gluon radiation.

1.7.1 The heavy flavor structure functions

$F_2^{c\bar{c}}$ is calculated from the measured charm cross sections as follows:

- The cross section for $c\bar{c}$ is calculated from the D^* cross section [24] (extrapolated to the full phase space) using:

$$\sigma(ep \to ec\bar{c}X) = \frac{1}{2}\frac{\sigma(ep \to eD^*X)}{P(c \to D^*)} \tag{1.32}$$

  where $P(c \to D^*)$ is the probability that a charm quark will produce a D^* meson (about 25%). As said in the sections 1.6.1 and 1.7, the advent of the micro-vertex detectors has permitted to distinguish events containing heavy quarks from light quark events by the long lifetimes of c and b flavoured hadrons, which lead to displacements of tracks from the primary vertex. Furthermore the results can be obtained in kinematic regions where there is little extrapolation needed to the full phase space and so the model dependent uncertainty due to the extrapolation is small. These measurements were done by the H1 Collaboration [25].

- Finally $F_2^{c\bar{c}}$ is related to $ep \to ec\bar{c}X$ cross-section by:

$$\frac{d^2\sigma(c\bar{c})}{dxdQ^2} = \frac{2\pi\alpha^2}{Q^4x}((1+(1-y)^2)F_2^{c\bar{c}} - y^2F_L^{c\bar{c}}), \tag{1.33}$$

  where the small contribution from $F_L^{c\bar{c}}$ is calculated from QCD, while xF_3 is neglected due to the fact that the measurements are made at small Q^2.

In Fig. 1.18 (plot on the left) all the data about $F_2^{c\bar{c}}$ are shown as function of x at Q^2 values between 2 and 500 GeV^2. The various data sets, obtained with different techniques, are in good agreement between them. The structure function $F_2^{c\bar{c}}$ shows a rise with decreasing x at constant values of Q^2. The rise becomes steeper at higher Q^2. The data are compared to calculations using the recent ZEUS NLO fit [26], in which the parton densities in the proton are parameterized by performing fits to inclusive DIS measurements from ZEUS and fixed-target experiments. The prediction describes the data well for all Q^2 and x except for the lowest Q^2, where some difference is observed. In Fig. 1.18 (plot on the right) the ratio $F_2^{c\bar{c}}/F_2$ is shown as function of x at fixed values of Q^2. The charm contribution

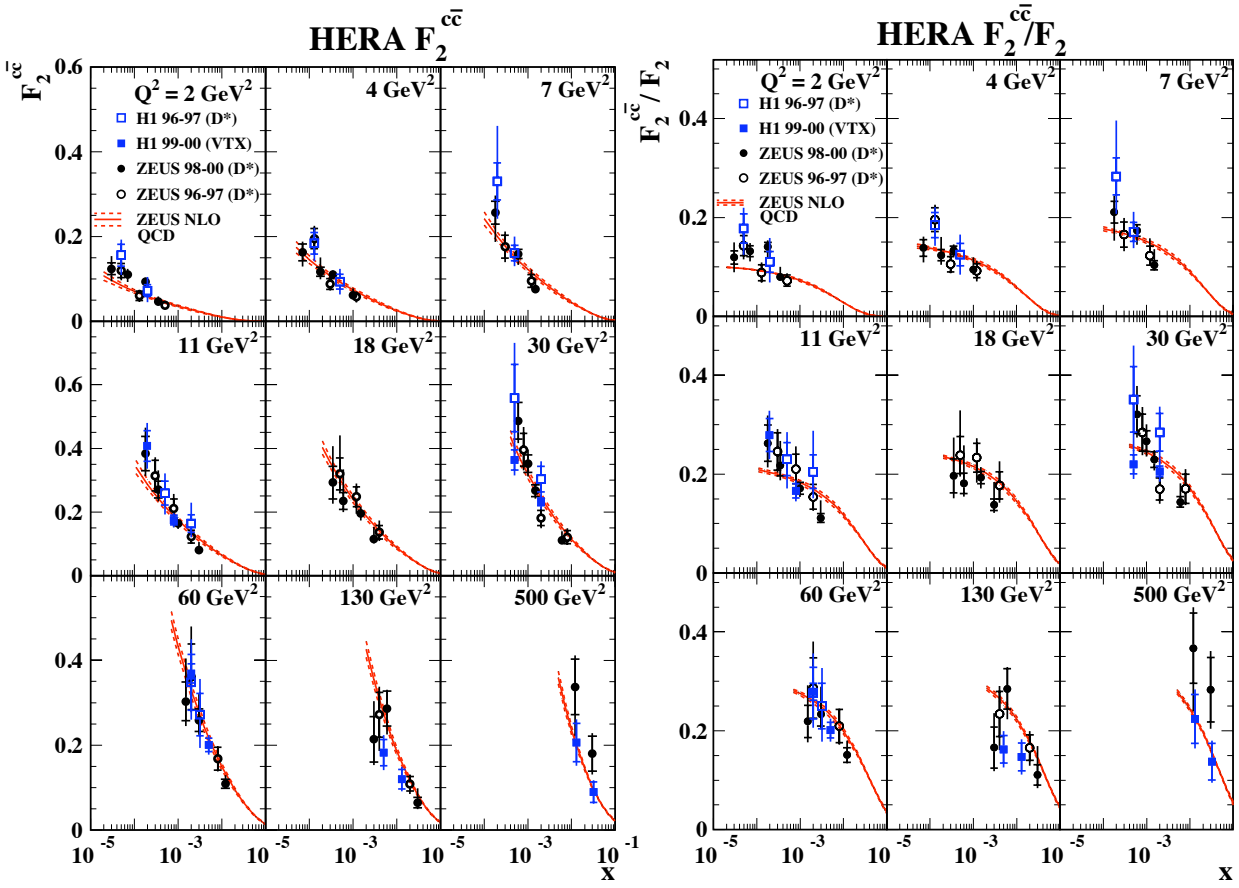

Figure 1.18: *On the left plot, the measured $F_2^{c\bar{c}}$ at Q^2 values between 2 and 500 GeV^2 as a function of x is shown while on the right plot the measured ratio $F_2^{c\bar{c}}/F_2$. Data from the H1 and* ZEUS *experiments using different charm tagging are shown. The data are shown with statistical uncertainties (inner bars) and statistical and systematic uncertainties added in quadrature (outer bars). The curves represent the ZEUS NLO fit.*

to F_2 rises from 10% to 30% as Q^2 increases and x decreases. The strong rise of $F_2^{c\bar{c}}$ at low values of x is similar to that of the gluon density and thus supports the hypothesis that charm production is dominated by the boson-gluon fusion mechanism.

Using the help of the micro-vertex detector it was possible to measure the structure function $F_2^{b\bar{b}}$ [25] in a similar manner to those depicted for the $F_2^{c\bar{c}}$. The measurement of the b cross section (and so of $F_2^{b\bar{b}}$) is particularly challenging since b events comprise only a small fraction (typically $< 5\%$) of the total cross section. In Fig. 1.19 the measured $F_2^{b\bar{b}}$ (by the H1 Collaboration) is shown as function of Q^2. The measurement shows positive scaling violations which increase with decreasing of x. The data are compared with the variable flavour number scheme QCD predictions from MRST [27] and CTEQ [28] at NLO and a recent calculation at NNLO [29]. The predictions are found to describe the data reasonably well. The beauty contribution to F_2, in the present kinematic range, increases rapidly with Q^2 from 0.4% at $Q^2 = 12$ GeV^2 to 1.5% at $Q^2 = 60$ GeV^2.

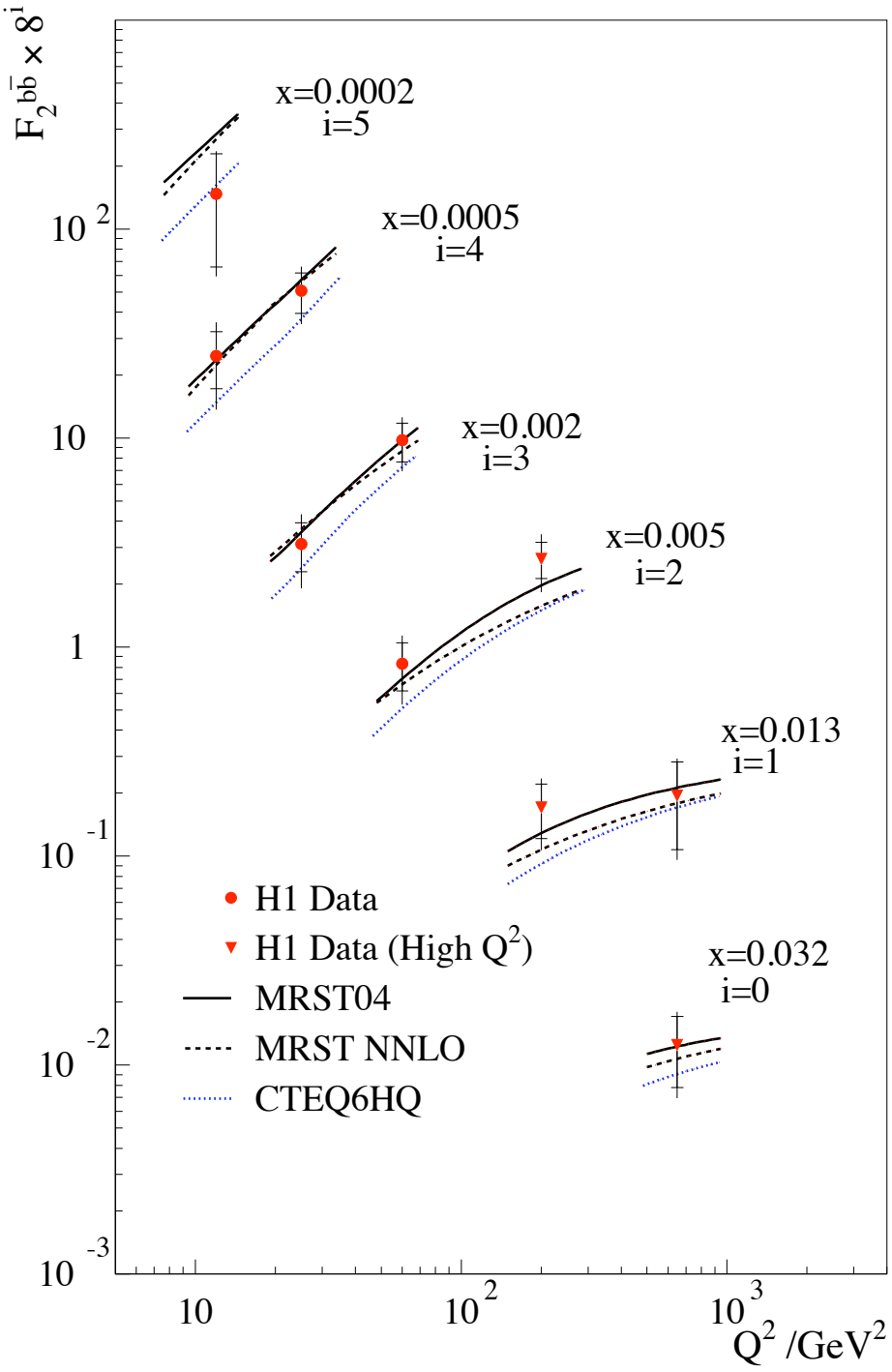

Figure 1.19: *The measured $F_2^{b\bar{b}}$ shown as function of Q^2 for various x values. The inner error bars show the statistical errors, the outer error bars represent the statistical and systematic errors added in quadrature. The prediction of QCD are also shown.*

Chapter 2

HERA and the ZEUS detector

In this chapter the HERA accelerator and the ZEUS detector are described briefly, giving particular emphasis on the parts of the detector used in the analysis described in this thesis. A detailed description of the ZEUS detector can be found in [30].

2.1 The HERA collider

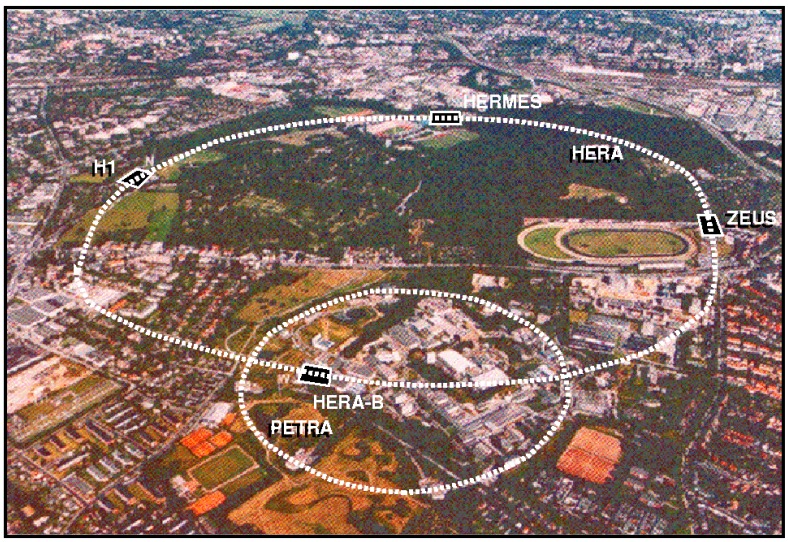

Figure 2.1: *The Hamburg Volkspark showing the* DESY *site. The location of the* HERA *and PETRA rings are shown. Also illustrated are the locations of the two colliding-beam experiments,* ZEUS *and H1, together with the single-beam experiments HERMES and* HERA-*B.*

The HERA (Hadron Elektron Ring Anlage) collider is a unique particle accelerator for the study of high-energy electron-proton (ep) collisions [31]. It is located at the DESY (Deutsches Electronen SYnchrotron) laboratory in Hamburg, Germany, and has been in operation since 1992. The HERA ring is located 15-30 m under ground level and has a circumference of 6.3 km. Fig 2.1 shows an aerial view of the tunnel area in Hamburg and the position of the different experiment halls (the ring has 4 linear sections linked at their extremities by 4 arcs of 779 m radius.)
The HERA machine collides electrons and positrons, accelerated to an energy of 27.5 GeV, with 820 (920) GeV protons (the energy of the proton beam was changed at the beginning of 1998 from 820 to 920 GeV). The resulting centre-of-mass energy is 300 (318) GeV, more than an order of magnitude higher than previous fixed-target lepton-nucleon experiments, allowing a new and wider kinematic region in x and Q^2 to be explored.

Running period	1993-1997		1998-2000		2003-2004	
Luminosity	$1.6 \cdot 10^{31}\ cm^{-2}\ s^{-1}$		$1.6 \cdot 10^{31}\ cm^{-2}\ s^{-1}$		$7.0 \cdot 10^{31}\ cm^{-2}\ s^{-1}$	
Center-of-mass energy	300 GeV		318 GeV		318 GeV	
	lepton	proton	lepton	proton	lepton	proton
Energy (actual)	27.5 GeV	820 GeV	27.5 GeV	920 GeV	27.5 GeV	920 GeV
Max number of bunches	210	210	210	210	180	180
Beam current	58	163	58	163	58	140
Particles per bunch	$3.65 \cdot 10^{10}$	10^{11}	$3.65 \cdot 10^{10}$	10^{11}	$4.18 \cdot 10^{10}$	10^{11}
Beam width (σ_x)	0.286 mm	0.280 mm	0.286 mm	0.280 mm	0.118 mm	0.118 mm
Beam height (σ_y)	0.060 mm	0.058 mm	0.060 mm	0.058 mm	0.032 mm	0.032 mm

Table 2.1: HERA *design parameters*.

Four experiments are located in four experimental halls placed along the HERA ring (Fig. 2.1). The two beams are brought into collision every 96 ns at zero crossing angle at two interaction points, one in the North Hall where the H1 experiment is located, the other in the South Hall where the ZEUS experiment is placed. In the East Hall the Hermes experiment studies the spin structure of the nucleon using the collisions of longitudinally polarized leptons on an internally polarized gas target (H, ^{2}D or ^{3}He). The HERA-B experiment, located in the West Hall was used until 2003 to collide the proton beam halo with a wire target to study B-meson production.

Built between 1984 and 1990, the HERA collider started operation in 1992 in its initial configuration with 820 GeVprotons and 26.7 GeVelectrons. In 1994 it was realized that the electron beam current was limited by positively ionized dust particles in the beam pipe through the pumps, reducing the lifetime of the beam. For this reason HERA switched to positrons in July 1994, achieving a more stable lepton beam and a significant increase in the integrated luminosity of the collected data. During the 1997-98 shutdown period, new pumps were installed in the lepton beam to improve the electron beam lifetime, and during 1998 and part of 1999 HERA was run again with electrons. In 1998 the energy of the proton beam was raised from 820 to 920 GeV. After the switch back to positron-proton collisions in 1999, the total delivered luminosity up to 2000 was $94.95\ pb{-}1$.

Although a lot of interesting measurements have already been performed at HERA, the desire was expressed by the experiments for an increase in the luminosity. The motivations for this increase were studied in a one-year workshop held between 1995 and 1996, when it was concluded that having $\sim 1 fb^{-1}$ of integrated luminosity would open up the possibility of new interesting measurements [32].
During the shutdown 2000/2001, the HERA collider was upgraded to achieve a five times higher specific luminosity at the collision point [33]. In addition spin rotators were included to rotate the spin of the leptons such that the lepton beam is longitudinally polarized at all interaction regions. A further longer shutdown was necessary in the middle of 2003 to solve severe background problems [34]. Since October 2003, HERA provided stable beam operations and delivered a total luminosity of 290 pb^{-1}.
A summary of HERA design parameters during the running periods 1993-1997 and 1998-2000 and 2003-2004 [35, 36] can be found in Table 2.1.

2.1.1 The HERA injection system

HERA provides two different injection systems for the beams, shown in Fig. 2.2.
The proton acceleration chain starts with negative hydrogen ions (H^-) accelerated in a LINAC to 50 MeV. The electrons are then stripped off the H^- ions to obtain protons, which are injected into the proton synchrotron DESY III and accelerated up to 7.5 GeVin 11 bunches with a temporal gap of 96 ns, the same as the main HERA ring; these bunches are then transferred to PETRA, where they are accelerated to 40 GeV. Finally they are injected into the HERA proton storage ring, and the injection stops when the ring contains 210 bunches. Through the radiofrequency generated in resonant cavities, the proton beam is then accelerated up to 920 GeV.
Pre-acceleration of the electrons (positrons) starts in two cascaded linear accelerators, LINAC I and LINAC II, where the leptons are accelerated up to 250 and 450 MeV respectively. The leptons are then injected into DESY II, accelerated to 7.5 GeVand then transferred to PETRA II, where they reach an energy of 14 GeVin bunches separated by 96 ns gaps. They are then injected into HERA where they reach the nominal lepton beam energy of 27.5 GeV, again until the main ring is filled with 210 bunches. Some of these bunches are kept empty (pilot bunches) in order to study the background conditions. When either the lepton or the proton bunch is empty, the beam related background, originating from the interaction of the lepton or the proton beam with the residual gas in the beam pipe, can be studied, whereas when both the bunches are empty the non-beam-related background, such as cosmic ray rates, can be estimated.

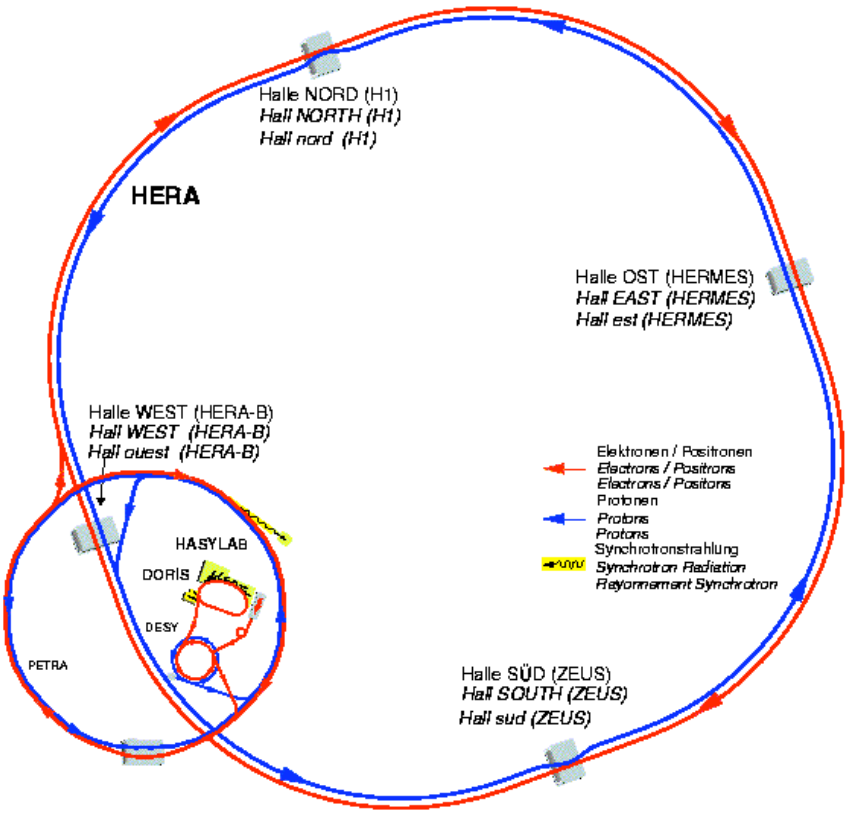

Figure 2.2: HERA *injection system*.

2.2 The HERA luminosity upgrade

HERA started delivering data in June 1992. Since then the luminosity has continously increased, as shown in Fig. 2.3.

The data collected so far were used to explore the proton structure and to test more and more precisely QCD theory; nevertheless the physics studied so far was predominantly low-Q^2 physics relative to the electroweak scale $Q^2 = m_W^2$. HERA was built to also explore this energetic region since phenomena such as the electron polarization and the possibility to have at disposal data with either electron and positron collisions becomes relevant only in the electroweak regime. With the luminosity upgrade new and important tests will be carried out to study the electroweak and strong interactions. Moreover, new phenomena which go beyond the standard model will be investigated; luminosity of the order of an inverse femtobarn will allow the search for particle states in an unexplored kinematic region above 200 GeV. The F_2 structure function will be more precisely measured, allowing the extraction of a gluonic density with a precision of 1%, which will allow more efficient testing of the validity of the QCD evolution equations over a large range in x and Q^2. Moreover the HERA capability to use both electron and positron beams will allow the determination of F_3, and hence the distribution of the valence quarks inside the proton. Studies of diffraction will significantly improve with the larger statistics available. Jet studies will be performed at high E_T allowing α_s measurements at different scales. Also important is the possibility of obtaining more precise measurements of the cross sections which can be calculated through QCD, providing a good test for this theory.
At HERA the luminosity is effectively defined as:

$$L = \frac{I_e \cdot N_p \cdot \gamma_p}{4\pi e \epsilon_N \sqrt{\beta^*_{xp}\beta^*_{yp}}} \tag{2.1}$$

where I_e represents the total leptonic current (only considering the colliding bunches), N_p is the number of protons in each bunch, ϵ_N is the normalized emittance of the proton beam, γ_p is the Lorentz factor for the protons, e is the

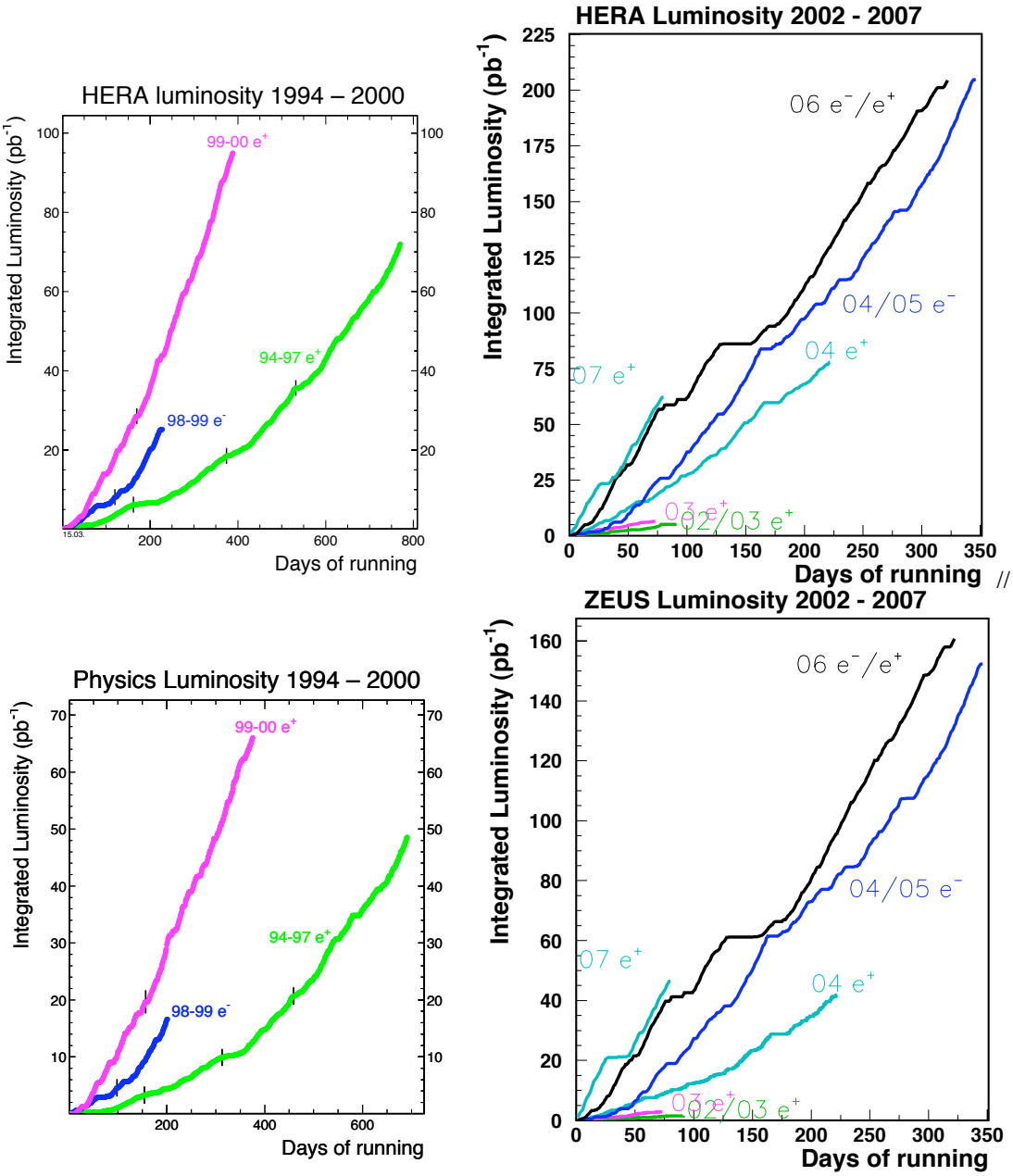

Figure 2.3: *Integrated luminosity provided by* HERA*, upper plots, and collected by* ZEUS*, lower plots, during the*HERA *I phase, 1992 - 2000, left hand side, and* HERA *II, right hand side.*

elementary charge, while β^*_{xp} and β^*_{yp} are the horizontal and vertical beta functions at the interaction point.
Increasing the intensities of the beams to substantially improve the luminosity would have required a huge financial cost (the currents of the leptonic beam could only have been incremented increasing in an almost proportional way the power of the radiofrequency cavity). Rather the luminosity was increased by making the interaction cross-section smaller by reducing the beta functions at the interaction point. These functions are limited by chromatic effects and limitations on the "opening" of the low beta quadrupoles. In order to increase the luminosity up to $\sim 7.4 \cdot 10^{-31} cm^{-2} sec^{-1}$ new superconducting magnets [37] close to the interaction point (inside the calorimeter volume), absorption system for the synchrotron radiation and for the vacuum were installed in the interaction region.
During the break, planned in order to upgrade the accelerator, the Micro Vertex Detector (MVD) was positioned inside the cavity between the beam pipe and the inner wall of the Central Tracking Detector (CTD).

2.3 The ZEUS detector

ZEUS is a multi-purpose, magnetic detector designed to study electron/positron-proton collisions.
It measures $12 \times 10 \times 19\, m^3$, weighs 3600 tonnes and it is quasi-hermetic covering most of the 4π solid angle, with the exception of the small region around the beam pipe.
As a result of the asymmetric beam energies, most of the final state particles are boosted in the proton beam direction. Consequently, the sub-detectors of ZEUS are coaxial but asymmetric with respect to the interaction point. The detector can measure energies from a few tens of MeV to hundreds of GeVin the forward region. For low momentum particles the tracking in the magnetic field is very precise, (resolution: $\sigma(P_T)/P_T \sim P_T$), while high energy particles are well measured by the calorimetric system (resolution: $\sigma(E)/E \sim \sqrt{E}/E$).
Particle identification is needed in a wide momentum range to achieve the physics goals. In Neutral Current (NC) DIS events the scattered lepton has to be identified and measured with high precision and the identification of electrons, positrons and muons is also needed in order to study the semi-leptonic decay of heavy quarks and exotic processes involving leptons.
In Charged Current (CC) DIS processes a hermetic detector is needed in order to reconstruct the missing transverse momentum carried by the outgoing neutrino. In these kinds of events, and also in untagged photoproduction events, the precise reconstruction of the final state is important in order to determine the event kinematics.
The ZEUS coordinate system is a right-handed, cartesian system with the origin defined as the nominal Interaction Point (IP) [1]. The positive z-axis points in the direction of the proton beam and is often referred to as the "forward" region. The x-axis points from the IP towards the centre of HERA ring and the y-axis lies at $90\,^\circ$ to the other two axes and points approximately vertically upwards. Since the proton-beam axis has a slight tilt, the y-axis does not precisely coincide with the vertical. The actual IP varies from event to event, and the run average and proton tilt varies on a fill-by-fill basis. However, the nominal IP is close to the geometric centre of the detector.

Polar angles are defined with respect to the proton-beam direction in the forward region ($\theta = 0$) and the leptonic-beam is therefore at $\theta = \pi$. The azimuthal angles ϕ are measured with respect to the x-axis.

The pseudorapidity variable is often used in event analysis; this quantity is an approximation at high energies of the particle rapidity given by $y = \log \frac{E+P_z}{E-P_z}$, and is defined by $\eta = -\log(\tan \frac{\theta}{2})$, where θ is the polar angle. The ZEUS coordinate system is illustrated in Fig. 2.4.

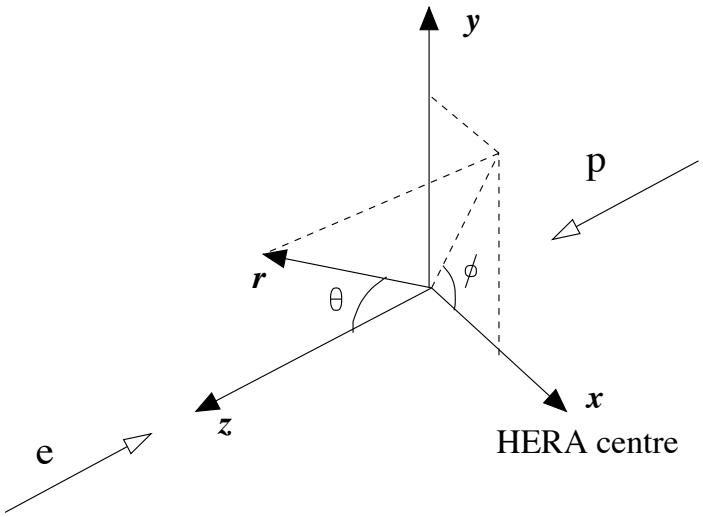

Figure 2.4: ZEUS coordinate system.

A brief outline of the various detector components is given below and a more detailed decription of the sub-detectors relevant to the present analysis will be given later in this chapter. A complete description of ZEUS and its components

[1] $x = y = 0$, defined in ZEUS by the geometrical centre of the central tracking detector, and $z = 0$ defines the nominal interaction point [38]

can be found in [30]. The two projection views of the detector in the $x - y$ and $z - y$ planes (Figs. 2.5 and 2.6) help to understand how the different components are placed in the different angular regions. At the centre of ZEUS, surrounding the beam pipe, lie the inner charged particle tracking detectors. The main tracking device is the CTD (Central Tracking Detector) placed in a solenoidal magnetic field (B=1.43 T) generated by a thin superconducting solenoid. In 2001, a silicon-strip Micro Vertex Detector (MVD) replaced the Vertex Detector (VXD) which was part of the initial configuration and removed during the 1995-1996 shutdown.
The CTD is supplemented in the forward direction by three sets of planar drift chambers (FTD) with interleaved Transition Radiation Detectors (TRD) (labelled FDET in Fig. 2.7).

In 2001 the TRD system was replaced by a Straw Tube Tracker (STT) consisting of two modules built of straw tube layers filling the gaps between the three FTD chambers. The rear direction is supplemented by one planar drift chamber consisting of three layers (RTD). Although technically part of the calorimeter, the Small Rear Tracking Detector (SRTD) provides improved position resolution for particles and is particularly useful for the identification of the scattered lepton in the rear direction not intercepted by the rear part of the calorimeter. Together, the tracking detectors offer an angular acceptance of $10^\circ < \theta < 160^\circ$ for charged particles.

The tracking system is surrounded by a compensating high resolution uranium-scintillator sampling calorimeter which is used as the main device for energy measurements; it is divided into three sections: the Forward (FCAL), Barrel (BCAL) and Rear (RCAL) CALorimeters. The iron yoke, which provides the return path for the solenoidal magnetic field flux, is equipped with a set of proportional tubes and serves as a calorimeter (BAC) for the detection of shower tails not completetly "contained" by UCAL; this device acts also as a tracking device for muon detection.
Dedicated muon identification detectors are located inside (FMUI, BMUI and RMUI) and outside the iron yoke (FMUO, BMUO and RMUO); for the inner muon chambers the iron of the yoke is magnetized with a toroidal field (with strength B $\simeq$ 1.7 T) in order to analyse the muon momentum.

Other detectors are located several metres away from the main detector along the beam pipe. The VETO wall is located in the rear direction at about z=-7.5 m from the interaction point. It consists of an iron wall supporting scintillator hodoscopes and is used to reject background from beam gas interactions. The LUMI detector is made of two small lead-scintillators calorimeters at z=-35 m and z=-(104-107) m and detects electrons and photons from bremsstrahlung events for the luminosity measurement.

2.4 The Central Tracking Detector (CTD)

The Central Tracking Detector (CTD) [39] is a cylindrical wire drift chamber used to measure the direction and momentum of the charged particles and to estimate the energy loss dE/dx which provides information for particle identification. The inner radius of the chamber is 18.2 cm, the outer is 79.4 cm, and its active region covers the longitudinal interval from z=-100 cm and z=104 cm, resulting in a polar angle coverage of $15^\circ < \theta < 164^\circ$. The chamber is flushed with a gas mixture of argon (Ar), carbon dioxide (CO_2) and ethane (C_2H_6) in the proportion 90:8:2. An alcohol/H_2O mixture (77 /23 %) is injected into the gas mixture, maintained close to the atmospheric pressure.
The CTD consists of 72 radial layers of sense wires, divided in groups of eight groups of nine *superlayers* (SL). A group of eight radial sense wires with associated field wires in one superlayer makes up a *cell*. The sense wires are 30 μm thick while the field wires have differing diameters. A total of 4608 sense wires and 19584 field wires are contained in the CTD.
The CTD is designed to operate in a magnetic field to allow the momentum measurement of charged particles. The field wires are tilted at 45° with respect to the radial direction in order to obtain a radial drift under the influence of the electric and magnetic fields. One octant of the CTD is shown in Fig. 2.8.

A charged particle traversing the CTD produces ionisation of the gas in the chamber. Electrons from the ionization drift towards the positive sense wires, whilst the positive ions are repelled and drift towards the negative field wires. The drift velocity of the electrons is approximately constant and equal to 50 $\mu m/ns$. An avalanche effect occurs close to the wire giving an amplification factor on the electrons of $\sim 10^4$ so that a measurable pulse is induced on the sense wires.
The superlayers are numbered 1 to 9 from the innermost to the outermost SL. Odd-numbered (axial) SLs have wires

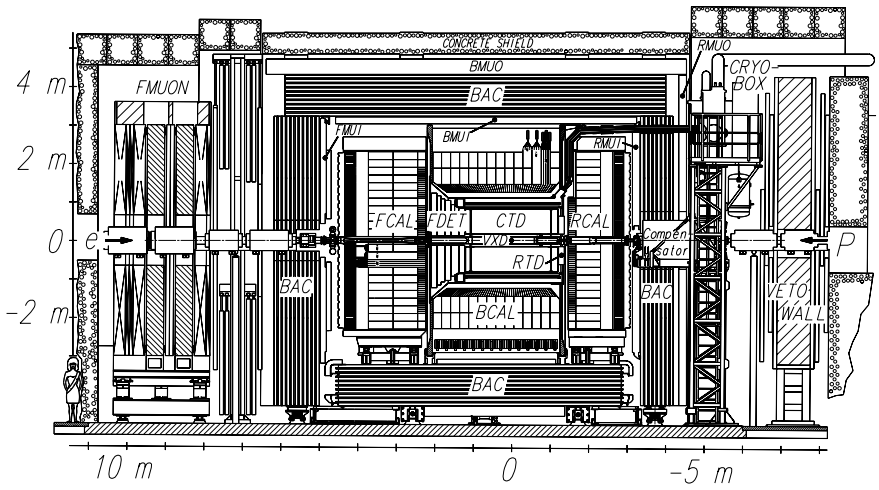

Figure 2.5: ZEUS longitudinal section ($z - y$).

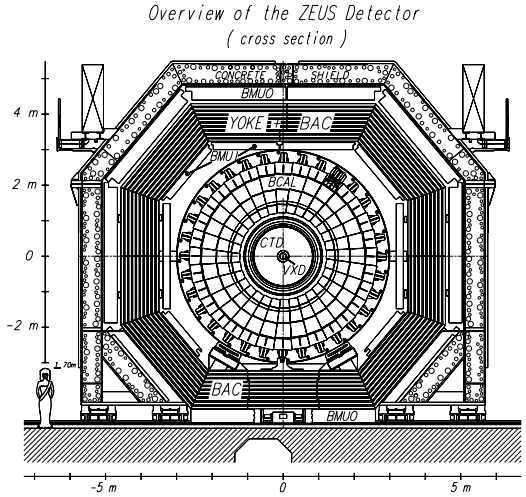

Figure 2.6: ZEUS transversal section ($x - y$).

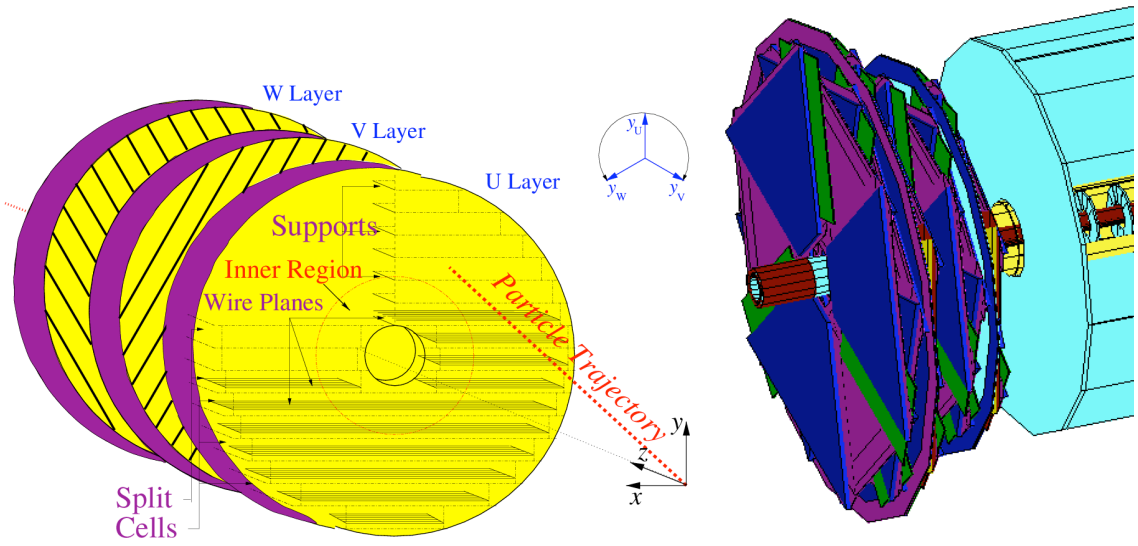

Figure 2.7: *Planar drift chambers (left) and straw tubes (right) constituting the Forward Tracking Detector (FDET).*

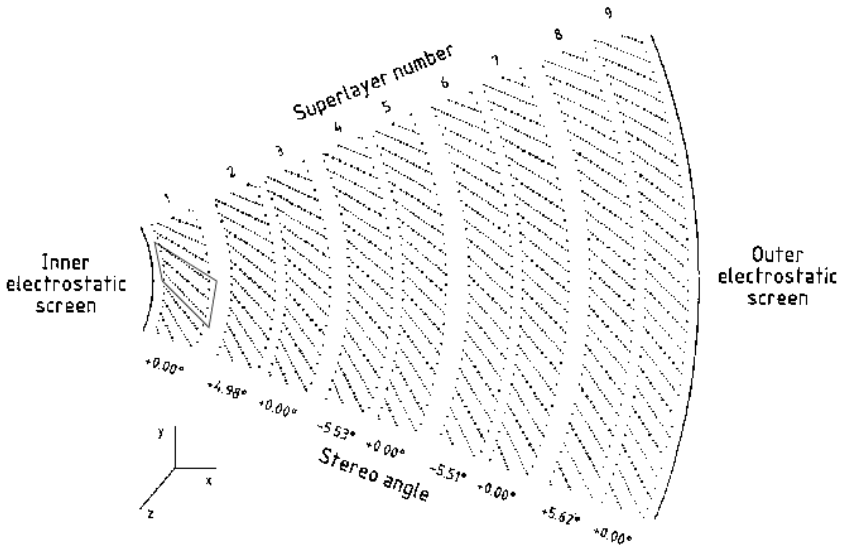

Figure 2.8: *Transverse cross section of one octant of the* CTD. *The sense wires are indicated with dots.*

parallel to the z direction, while wires in even-numbered (stereo) SLs are at a small stereo angle of $\pm 5\,^{\circ}$ to achieve a better resolution in z. The achieved resolution is $\sim 100 - 120 \mu m$ in the $r - \phi$ plane and 1.4 mm in the z coordinate. The three inner axial superlayers (SL1, SL3, SL5) are additionally instrumented with the z-by-timing system. This estimates the z-position of a hit by measuring the difference in arrival time of the pulses on the sense wires at each end of the detector. Although the resolution achieved ($\sim 3\ cm$) is much cruder than that obtained using the full axial and stereo wire information, it is a relatively fast method and used predominantly for trigger and track seed-finding. As already mentioned, the CTD is contained within a superconducting solenoid which provides a magnetic field of 1.43 T. This field causes charged particles to travel in a circular path of radius, R, given by:

$$R = P_T/QB \quad \text{(S.I. units)} \tag{2.2}$$

where Q is the charge of the particle (Coulombs), B is the strength of the magnetic field (Tesla) and P_T is the transverse momentum (kg m s^{-1}). This allows an accurate determination of the P_T of the charged particle. The resolution on

the transverse momentum P_T, for tracks fitted to the interaction vertex and passing at least three CTD superlayers, and with $P_T > 150$ MeV, is given by [40]:

$$\sigma(P_T)/P_T = 0.0058 P_T \oplus 0.0065 \oplus 0.0014/P_T \tag{2.3}$$

where P_T is expressed in GeV. The error includes the hit position resolution (first term) and the multiple scattering before and inside the volume of the chamber (second and third terms), where the symbol $\oplus$ indicates the quadratic sum.
Since the installation of the MVD in 2001, the resolution has changed and the influence of new detector components on the resolution of the tracking system is still under investigation. It is expected that the influence from multiple scattering is larger (more material) but that the hit resolution is better compared to the resolution quoted above due to the inclusion of MVD hits. Latest results including the MVD in the global track reconstruction parametrize the momentum resolution in an a way analogue to the
CTD–only resolution [41]:

$$\sigma(P_T)/P_T = 0.0026 P_T \oplus 0.0104 \oplus 0.0019/P_T \tag{2.4}$$

2.5 The ZEUS Microvertex Detector (MVD)

During the 2000-2001 shutdown, planned for the luminosity upgrade, a silicon microvertex detector (MVD) was installed in ZEUS.
The MVD, placed between the beam pipe and the inner volume of the CTD, provides an improvement in the global precision of the tracking system and allows the identification of events with secondary vertices originating from the decay of particles with long lifetime ($c\tau \gtrsim 100 \mu m$). This device helps the study of hadron decays containing heavy quarks such as charm and beauty, or tau leptons thanks to an improvement in the track resolution with the possibility to resolve secondary vertices.
The main analysis topics which can be substantially improved through the use of the MVD are [51]:

- *Charm and beauty in photoproduction*. Measuring the rate of events containing charm (and beauty) in direct photoproduction, it is possible to study the gluon content of the proton.
- *Charm and beauty in Deep Inelastic Scattering*. The measurement of the proton structure function F_2^{charm} will cover a kinematic range beyond the one accessible so far from ZEUS using D^* meson tagging. This analysis is currently characterized by a low efficiency, around 1%, with 30% purity and hence very limited statistics. The introduction of the MVD will allow charm tagging with an efficiency between 10% and 30% and with a purity greater than 30%. The proton structure function F_2^b will be extracted.
- *New physics*. The possibility to identify tracks originating from secondary vertices and the tracking resolution improvement will allow a better reconstruction of the events containing electrons with very high Q^2 which are scattered in the forward region.

The technical requirements which were taken into account during the design of the MVD are:

- angular coverage around the interaction point between $10^\circ < \theta < 160^\circ$;
- measurement of three points for each track in two independent projections;
- $20\ \mu m$ intrinsic hit resolution;
- separation of two tracks up to $200\ \mu m$;

The main limitations are due to the small amount of space available between the CTD and the beam pipe. The following description summarizes the main characteristics of the MVD, in its two components covering the central (BMVD) and forward (FMVD) region (see Fig. 2.9).

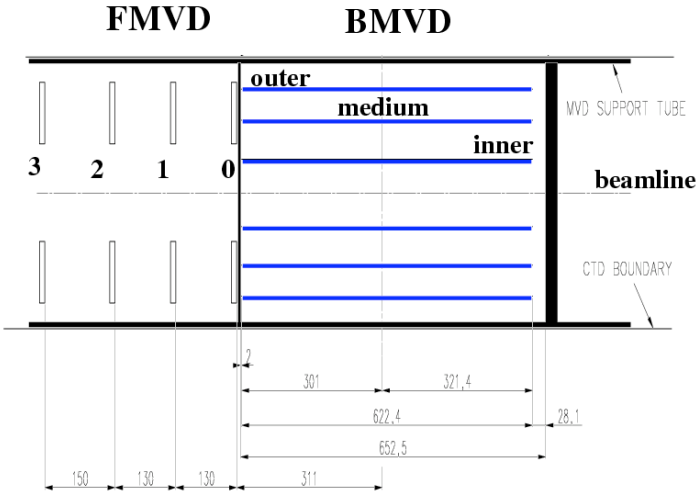

Figure 2.9: *Longitudinal* MVD *section. There are 3 layers in the barrel region and the 4 wheels in the forward section.*

2.5.1 Barrel and forward micro vertex detector

The barrel section of the MVD is 64 cm long (see Fig. 2.9) and is sub-structured in three layers to allow high efficiency in the pattern recognition and to make an estimate of the track momentum in the trigger phase.
The first layer of silicon detectors follows the elliptical path around and along the beam pipe and it is placed at a variable radius between 3 and 5 cm from the CTD axis (see Fig. 2.10).
The beam pipe is not centred with respect to the CTD axis and the nominal interaction point is shifted towards the

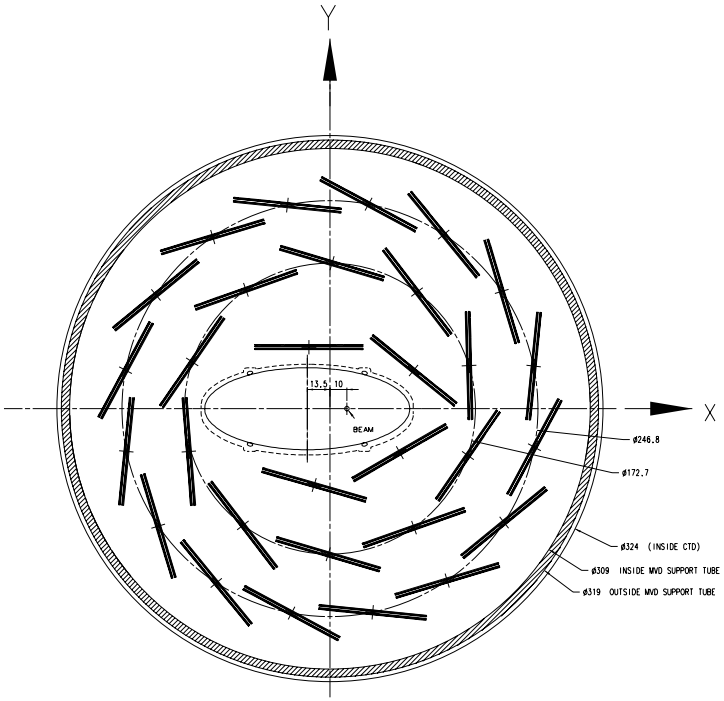

Figure 2.10: *B*MVD *section: 3 superlayers around beam pipe are shown.*

centre of HERA (along the x axis) by about 4 mm in order to accommodate the primary synchrotron radiation spread

inside the beam-pipe volume. The second and third layer are placed along a circular path at $r \sim 8.6$ cm and $r \sim 12.3$ cm. On average a track crosses 2.8 layers. The resolution on the impact parameter, based on Monte Carlo studies, is shown in Fig. 2.11. These resolution studies are for tracks perpendicular to the beam pipe ($\eta = 0$) which cross all

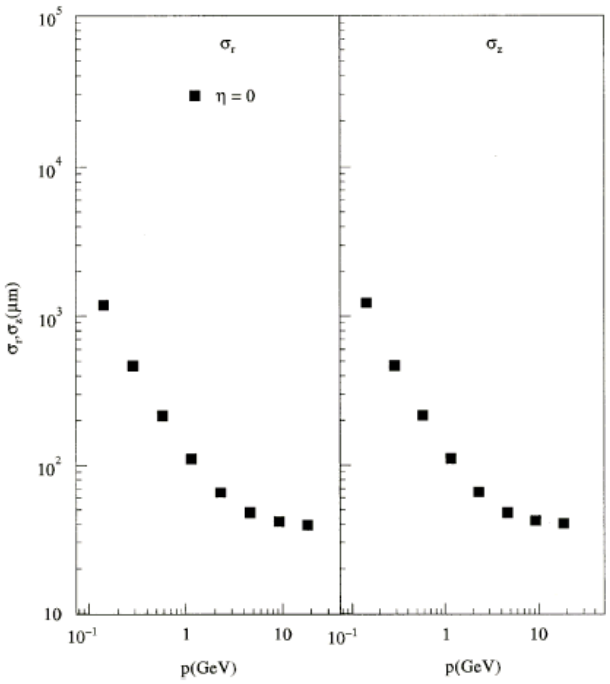

Figure 2.11: *Impact parameter resolution on tracks at $\eta = 0$ as a function of the momentum. The measurements are for tracks crossing 3 layers of half modules [52].*

three layers, as a function of track momentum.

The BMVD is equipped with 600 silicon strips sensors mounted on 30 carbon fibre structures called *ladders* (Fig. 2.12); two layers of sensors are placed parallel and perpendicular to the beam line in order to measure $r - \phi$ and $r - z$ coordinates. Each layer is made of two single-sided silicon strip planes (320 μm thickness) with p^+ strips implanted

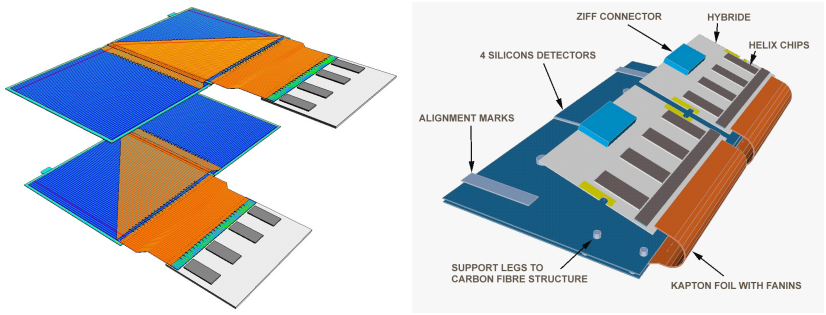

Figure 2.12: *Half modules and ladders mounted on the support.*

in a n-type bulk. The strip pitch is 20 μm; every 6^{th} strip has an AC coupling with a read out line made by an aluminium strip through a dielectric material ($SiO_2 - SiN_4$). Two sensors are glued together, electrically connected with a copper path excavated in a Upilex foil of $50\mu m$ of thickness (see fig. 2.12). From the figure it can be seen that the sensor is connected to the readout device; the resulting surface covered by the two sensors and by the readout system is called a "half-module" and is 6.15 cm $\times$ 6.15 cm.

The FMVD consists of 4 planes called *wheels*, each of them is made of two layers of 14 silicon sensors with the same technical characteristics of the barrel sensors but with a trapezoidal shape (Fig. 2.13). This device allows the

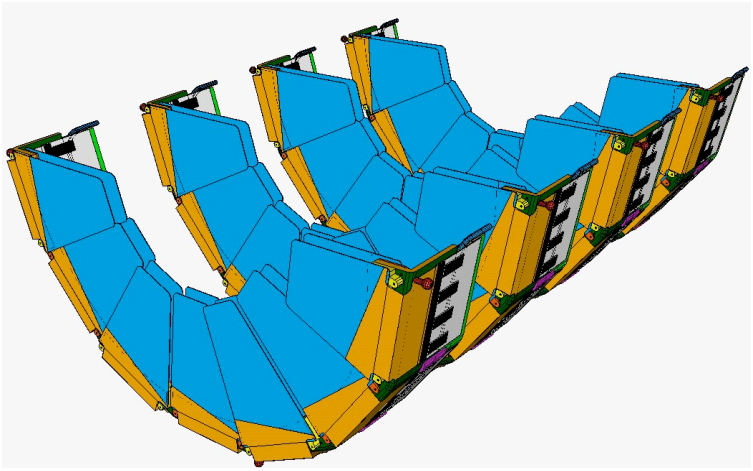

Figure 2.13: *F*MVD *4 wheels*.

acceptance to extend in pseudorapidity up to $\eta = 2.6$, a region where tracking information has yet to be used in ZEUS. Each wheel has inner and outer sensors. They are mounted back to back. An inner and outer wheel sensor form a sector. The crossing angle between the strips in the inner and outer sensor is $\sim 13^\circ$ ($180^\circ/14$). Inside a layer of sensors the adjacent sensors are slightly overlapped in order to minimize the dead regions. The four wheels are positioned at z=32, 45, 47 and 75 cm; the first wheel is linked to the structure supporting the BMVD. A more detailed description can be found in [53].

2.5.2 Readout electronics

The MVD silicon sensors are read by the analog chip HELIX3.0 [54] (see fig. 2.14); the chip integrates 128 channels with a charge-sensitive preamplifier followed by a shaper which produces a Gaussian signal with a time peak of $50-70$ ns. The signals are sampled in an analog pipeline where up to 136 event measurements can be stored while the GFLT is producing a trigger decision. The HELIX outgoing signal is transferred with an analog connection to the ADC boards, which perform a first cluster reconstruction. The signal is then transferred to the MVD second level trigger processor and to the ZEUS event builder.

2.5.3 Preliminary test results

The MVD design was exposed to a detailed test-beam programme; half-modules were exposed to a 2-6 GeVelectron test beam at the DESY II accelerator (see fig. 2.15). The charge produced by a particle crossing the device was collected by three reference sensor pairs which gave the coordinates in the $x-y$ plane perpendicular to the beam which defines the z axis direction. The reference sensors were strip sensors with a readout pitch of 50 μm and an intermediate strip. The system could be moved sideways and rotated in order to select tracks with a specific incidence angle.
Strips collecting the highest charge above a certain threshold were selected in order to find cluster candidates. The threshold was set to 5σ, where σ is the squared average noise of each strip. The impact position reconstruction was calculated using three different algorithms:

- *Eta Algorithm*: it is based on the assumption that most of the charge is collected by the two strips closest to the impact position. If Q_{left} (Q_{right}) is the charge collected on the left (right) side of the impact position, P is the readout pitch and x_{left} (x_{right}) is the position on the left (right) strip, the x_{eta} can be defined as:

$$x_{eta} = P \cdot f(\eta) + x_{left} \tag{2.5}$$

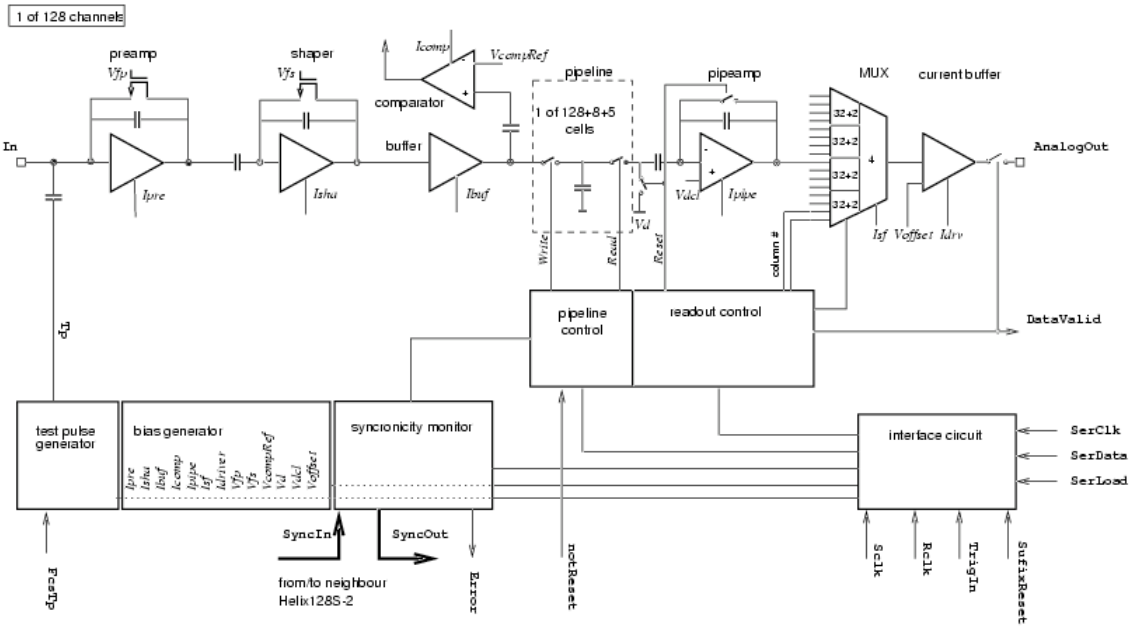

Figure 2.14: *Schematic view of the analog HELIX chip*.

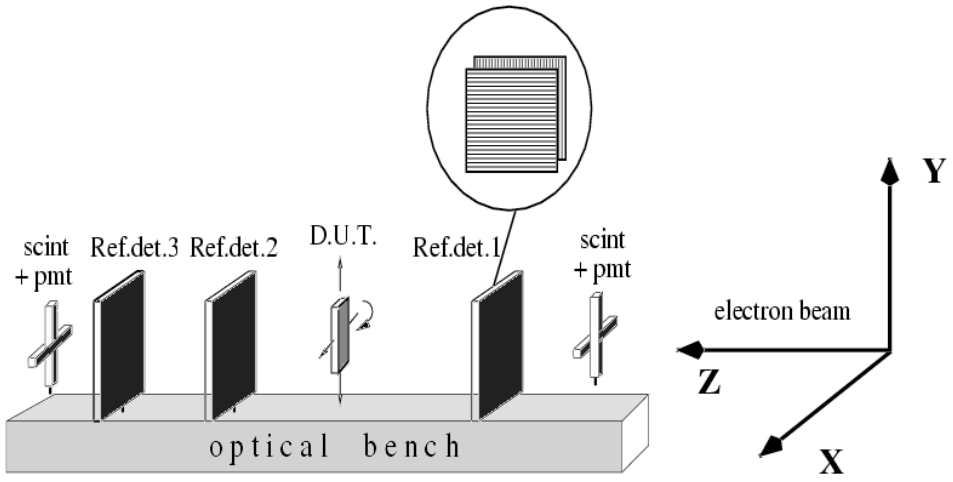

Figure 2.15: *Schematic view of the device used with the test beam*.

with:

$$\eta = \frac{Q_{right}}{Q_{right} + Q_{left}}, \quad f(\eta) = \frac{1}{N}\int_0^{\eta} \frac{dN}{d\eta'} d\eta'. \tag{2.6}$$

- *Double Centroid Algorithm*: it reconstructs the impact position using the strip collecting the highest charge and the two nearest strips. Once the gravity centre C_{left} (C_{right}) between the central and the left (right) strip is calculated, the hit position will be:

$$x_{DC} = \frac{C_{left}/dr + C_{right}/dl}{dr + dl}, \quad \text{where} \quad dl = \frac{C_{left}}{C_{right}} = 1/dr. \tag{2.7}$$

- *Head-Tail Algorithm*: for large incidence angles, the charge generated by a particle is spread over many strips. In this case, the charge collected by the central strip of the cluster does not contain precise information about the position. The head-tail algorithm uses the information from the external strips on both sides to solve this problem. The *head* (*tail*) strip is that with the lowest (highest) identification number (integer number defining the strip position inside a sensor) which collects a charge three times higher than the noise level.
  The hit position will be given by:

$$x_{HT} = \frac{x_h + x_t}{2} + \frac{Q_t + Q_h}{2Q_{AV}} \cdot P \tag{2.8}$$

  where $x_h(x_t)$ is the head (tail) strip position and Q the charge. Q_{AV} is the average pulse height for each strip inside the cluster.

Figure 2.16 shows the instrinsic resolution as a function of the incident angle, measured with the three different algorithms. The intrinsic spatial resolution reaches $13\mu m$ for tracks perpendicular to the sensor surface.

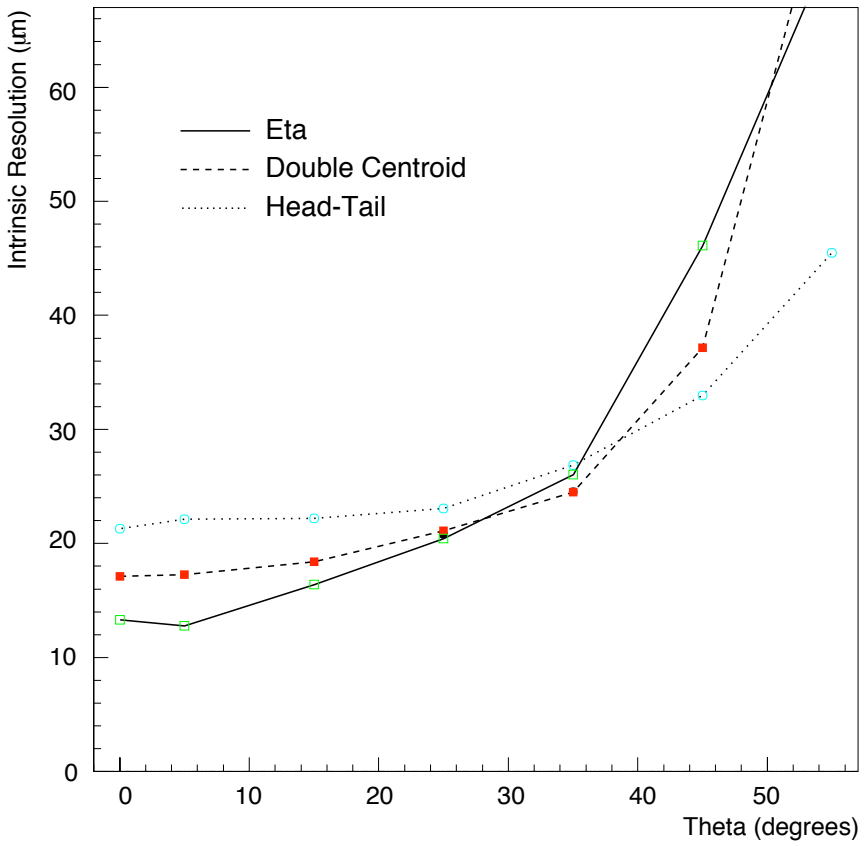

Figure 2.16: *Intrinsic resolution as a function of the incident angle, measured with the three different algorithms [57].*

2.5.4 Radiation monitor

The main radiation sources in the MVD area are the synchrotron radiation and the radiation caused by beam losses. The MVD is expected to be operative for at least 5 years. During this period, the foreseen integrated radiation dose is ~ 0.5 kGy. The MVD detector and all the readout electronics were designed to work without a change in the signal-noise ratio, up to an integrated dose of 3 kGy. In order to keep the radiation dose under control, a radiation monitoring system (RadMon) generates warning signals when there is high radiation and generates a dump signal to the electron kicker. This RadMon is also used to calculate the time integrated total dose.

2.6 The Uranium-scintillator Calorimeter (UCAL)

The ZEUS calorimeter (UCAL) [44] is a high-resolution compensating calorimeter. It completely surrounds the tracking devices and the solenoid, and covers 99.7% of the 4π solid angle. It consists of 3.3 mm thick depleted uranium plates (98.1% U^{238}, 1.7 $\%$ Nb, 0.2 $\%$ U^{235}) as absorbers alternated with 2.6 mm thick organic scintillators (SCSN-38 polystyrene) as active material.
The hadronic showers contain both hadronic and electromagnetic components whose proportions can fluctuate enormously (see Fig. 2.17). In order to take into account this phenomenon and therefore optimize the energy detection of

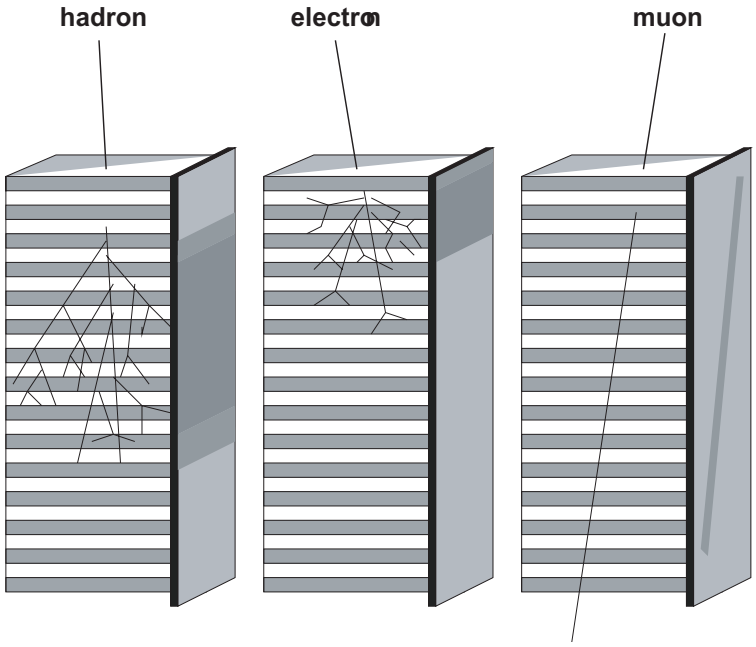

Figure 2.17: *Production of showers inside* ZEUS *calorimeter.*

both shower components, the uranium calorimeter was designed to be *compensating*, so as to obtain the same mean detector response from hadronic and electromagnetic showers of the same energy (e/h=1). Therefore the UCAL has different layers of depleted uranium and scintillator with thickness of 3.3 mm and 2.6 mm (Fig. 2.18).
Under test beam conditions [45], the electromagnetic resolution achieved is:

$$\frac{\sigma_E}{E} = \frac{18\%}{\sqrt{E}} \oplus 2\% \tag{2.9}$$

whilst the hadronic resolution is:

$$\frac{\sigma_E}{E} = \frac{35\%}{\sqrt{E}} \oplus 1\% \tag{2.10}$$

where E is the particle energy measured in GeV.

The UCAL is divided into three regions: the forward (FCAL), barrel (BCAL) and rear (RCAL) calorimeter. Since most of the final state particles in a lepton-proton interaction at HERA are boosted to the forward (proton) direction, the three parts are of different thickness, the thickest being the FCAL ($\sim 7\lambda$), then the BCAL ($\sim 5\lambda$) and finally the RCAL ($\sim 4\lambda$), where λ is the interaction length.
Each part of the calorimeter is divided into *modules*. The 23 FCAL modules and the 23 RCAL modules are rectangular, whereas the 32 BCAL modules which surround the cylindrical CTD are wedge-shaped covering $11.25\,^{\circ}$ in azimuth. An FCAL module is shown in Fig 2.18. Each module consists of so called *towers* of $20 \times 20 cm^2$ which are subdivided longitudinally into one electromagnetic (EMC) and two (one in RCAL) hadronic (HAC) sections. The EMC sections are further transversely divided into four cells (only two in RCAL).
The FCAL EMC section per tower consists of the first 25 uranium-scintillator layers and has a depth of 25 X_0, where

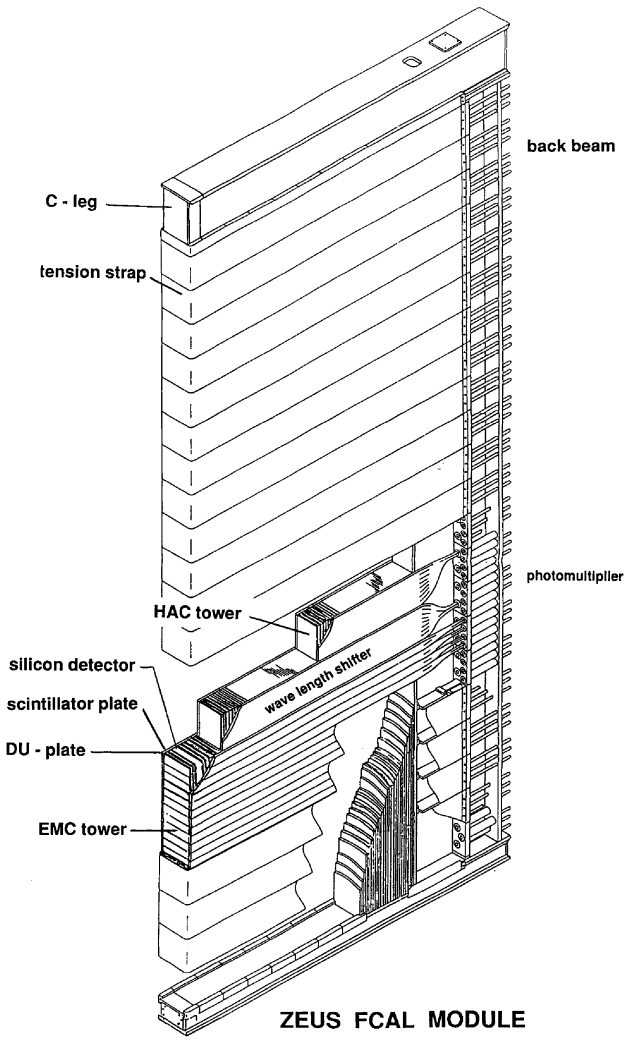

Figure 2.18: Section of an FCAL module.

X_0 is the radiation length. Each of the two HAC sections per FCAL tower is 3.1 λ deep and consists of 160 uranium-scintillator layers.
The BCAL EMC section is made of the first 21 uranium-scintillator layers, the two HAC sections of 98 layers. The resulting depth is 21 X_0 for the electromagnetic section and 2.0 λ for each hadronic section.
The RCAL towers consist of one EMC and only one HAC section. Therefore its depth is 26 X_0 for the EMC part and 3.1 λ for the HAC part.
Light produced in the scintillators is read out by 2 mm thick wavelength shifter (WLS) bars at both sides of the module, and brought to one of the 11386 photomultiplier tubes (PMT) where it is converted into an electrical signal. The summed information per cell is used for energy and time measurements. The UCAL provides accurate timing information, with a resolution of the order of 1 ns for particles with an energy deposit greater than 1 GeV. This information can be used to determine the timing of the particle with respect to the bunch-crossing time, and it is very useful for trigger purposes in order to reject background events, as will be illustrated later in the trigger section.
Calibration of the PMTs and the electronics is mainly performed using the natural radioactivity of the depleted uranium which produces a constant signal in the PMTs. The signal can be used to intercalibrate geometrically identical regions and to transport the absolute calibration scale determined in test beam measurement. In addition, laser, LED and test pulses are also used for the calibration. The achieved accuracy is better than 1%.

2.7 The luminosity measurement

The luminosity measurement at ZEUS is done by studying the production rate of photons through the Bethe-Heitler process [47]:

$$e + p \rightarrow e' + p + \gamma, \tag{2.11}$$

where the photon is emitted from the electron at very small angles with respect to the ingoing lepton direction (negative z). The cross section for this process at the leading order (LO) is expressed as:

$$\frac{d\sigma}{dk} = 4\alpha_e r_e^2 \frac{E'}{kE}\left(\frac{E}{E'} + \frac{E'}{E} - \frac{2}{3}\right)\left(ln\frac{4E_pEE'}{Mmk} - \frac{1}{2}\right) \tag{2.12}$$

where E and E_p are the energies of the lepton and proton beams respectively, E' is the outgoing electron energy, k is the photon energy, M and m are the proton and electron masses while r_e^2 represents the classical electron radius. Higher-order corrections in the above cross section calculation are less that 0.5%.

The luminosity monitor consists of a photon and a lepton calorimeter [48], located along the beam pipe at z= -(104 - 107) m and z= -35 m, respectively (Fig. 2.19)

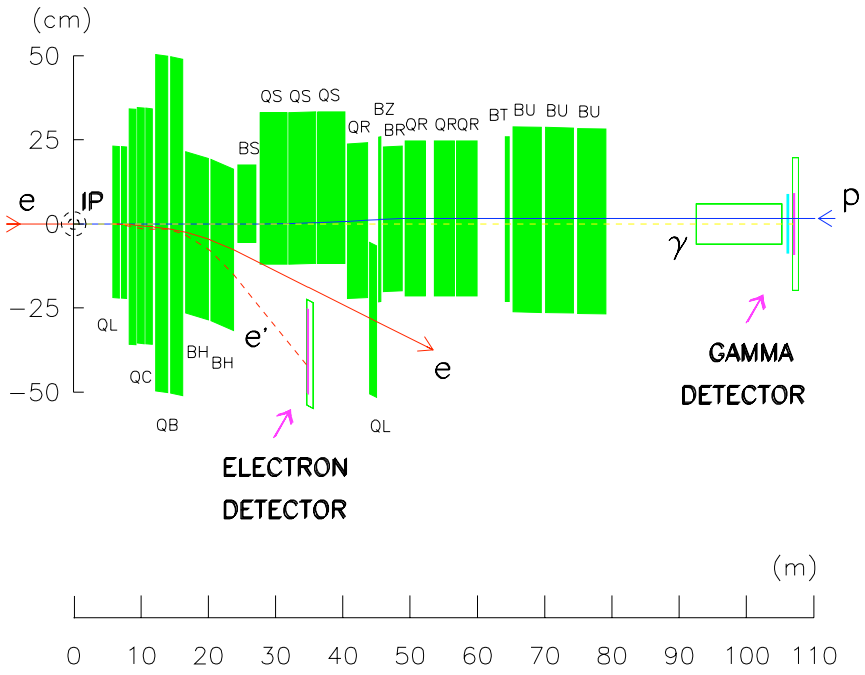

Figure 2.19: *The layout of the* ZEUS *Luminosity Monitor. The nominal interaction point is located at (0,0).*

To protect the photon calorimeter against synchrotron radiation, it has been shielded by a carbon-lead filter. The resulting calorimeter resolution, (with E in GeV), is:

$$\frac{\sigma_E}{E} = \frac{0.25}{\sqrt{E}}. \tag{2.13}$$

The bremsstrahlung event rate is determined by counting the number of photons above a fixed energy threshold, and not by the simultaneous identification of the lepton and the photon, because of the dependence of the lepton calorimeter acceptance on the beam position and angle. The luminosity is then extracted using:

$$L = \frac{R_{ep}\left(E_\gamma > E_\gamma^{th}\right)}{\sigma_{ep}^{acc}\left(E_\gamma > E_\gamma^{th}\right)}, \tag{2.14}$$

where $\sigma_{ep}^{acc}\left(E_\gamma > E_\gamma^{th}\right)$ is the cross section corrected for the detector acceptance, $R_{ep}\left(E_\gamma > E_\gamma^{th}\right)$ is the photon rate and E_γ^{th} is the photon threshold.

2.8 Background

The background event rate at ZEUS can be much higher than the ep interaction rate, especially in the machine startup phases, depending on the beam-pipe vacuum conditions. The main background sources which have to be removed are:

- gas interactions inside the beam pipe: when the beam particles interact with the residual gas inside the beam pipe. If this interaction happens near the detector, the interaction products can be detected by ZEUS.
- halo muons: the hadronic interactions of the beam protons can subsequently produce muons through pion or kaon decays; these muons go into the halo beam and are therefore called *halo muons*.
- cosmic muons: these are muons coming from the cosmic showers generated in the atmosphere which can be detected by ZEUS.

The background is dramatically reduced by the trigger, which is tuned to reduce it. The background coming from the interaction of the particles with the beam gas is limited through the VETOWALL device, an iron wall 87 cm thick and $800 \times 907 cm^2$ placed at z=-7.5m from the interaction point. It is instrumented with two scintillator hodoscopes, one for each side of the wall, which can identify the beam-gas-interaction events. A $95 \times 95\ cm^2$ gap window is left uncovered around the beam-pipe.
The trigger system, described in the next chapter, takes into account the information coming from the calorimeter, SRTD (a hodoscopic scintillator placed around the beam pipe in front of the RCAL) and C5 (a HERA collimator equipped with scintillator counters placed behind the RCAL at 1.2 m from the nominal interaction point in the electron beam direction).
The temporal information from the ZEUS calorimeter is calibrated in order to have no temporal gap for the particle in the interaction region. The timing difference between the FCAL and RCAL measurements can be used to reject the beam gas events, since the products from the beam gas interactions hit the RCAL $\sim$ 10 ns before hitting the FCAL. The calorimeter temporal resolution, for energy E greater than few GeV, is better then 1 ns. The same method is used to tag the cosmic muons, studying the temporal difference between the upper and lower side of BCAL.

2.9 The ZEUS trigger system

The bunch crossing frequency at ZEUS is $\sim 10\ MHz$, corresponding to a time gap of $96ns$ between two consecutive collisions. The rate is dominated by the interaction of the proton beam with the residual gas which contributes about $10 - 100\ kHz$, depending upon the vacuum levels in the beam-pipe up to 100 m upstream of ZEUS. This frequency has to be reduced at a level compatible with the offline data storage without losing interesting physics events (few Hz).
The approach adopted for the ZEUS data acquisition is a three level trigger system with increasing complexity of the decision making algorithm and decreasing throughput rate (Fig. 2.20).

- *first level trigger (FLT)*; is a hardware based trigger which uses programmable logic to make a quick rejection of background events. The FLT reduces the input rate of $100kHz$ to an output rate of $1kHz$. As it is not possible to take a decision within the bunch crossing time, the data are pipelined until the trigger decision is taken.
  Individual component decisions use a subset of the total data, and are made within 1.0-2.5 μs. The global first level trigger (GFLT) calculations take up to 20 bunch crossings and the FLT delivers the abort/accept decision after 4.4 μs.
  Typical criteria used by the FLT in taking the trigger decision are the approximate "crude" event vertex position, the transverse energy of the event, and energy sums in sections of the calorimeter. The FLT has a good efficiency for ep physics ($\sim 100\%$), but still has a very low purity ($\sim 1\%$).
- *second level trigger (SLT)*; the SLT is a parallel processor utilising a network of transputers. It reduces the FLT output rate of $\sim 1\ kHz$ to an output rate of $\sim 100\ Hz$. As in the FLT, the outputs of the component SLT decisions are passed to the global SLT (GSLT) where the event decision is made. The GSLT makes its decision after 5.2-6.8 ms. The decision is based upon limited charged particle tracking, vertex determination, calorimeter

timing and $E - P_z$ and scattered electron tagging.
Data from an event accepted by the SLT trigger is sent directly from the component to the event builder (EVB). The EVB stores the data from the components until the third level trigger (TLT) is ready to process it, and combines the data from different components into one consistent record: the event. One event is stored in a single record of the ADAMO [49] database tables.

- *third level trigger (TLT)*; is a software trigger which is sent asynchronously with the bunch crossing on a dedicated PC farm. At this stage an approximate version of the event reconstruction software is run, including tracks and interaction vertex reconstruction. The TLT has been designed to cope with an input rate of $100Hz$ from the SLT at design luminosity. The output rate is reduced to about $5Hz$.
  After the decision to accept the event, the TLT sends the data via optical link to the DESY computer centre, where the events are written onto disk to be available for further offline reconstruction and data analysis.

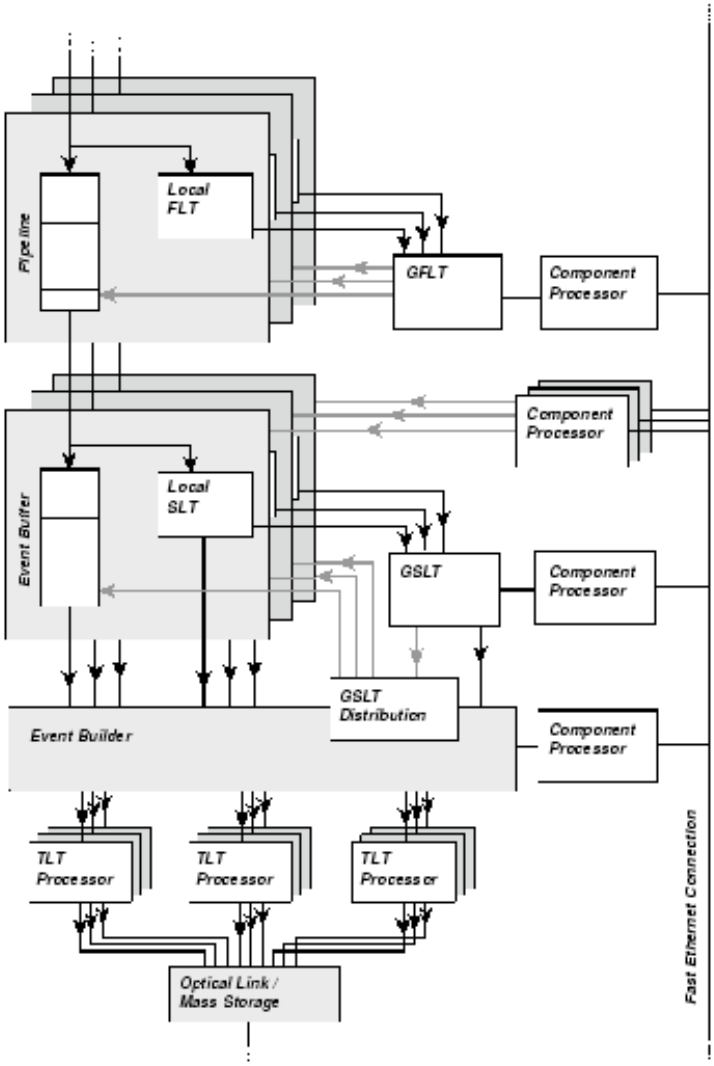

Figure 2.20: ZEUS trigger chain

2.10 Physics simulation

The use of simulation programs is important in physics analysis. A better understanding of the data and the detector behaviour can be achieved by simulating the detector response to physics events. Moreover, the theoretical models implemented in the simulations can be tested by comparisons to real data.
The simulation of physics events at HERA is done in two main steps. First, the ep scattering process is simulated using an *event generator*. This programme, following the prescriptions of the theoretical models implemented in it, provides a complete list of the four-momenta of the final state particles. In the second step, all the detector and the trigger systems are simulated, in order to determine their response to the particles produced in the physical process. These simulations are based on Monte Carlo (MC) techniques, which are an essential tool in understanding the complexity of high energy physics processes and of particle detectors.

2.10.1 General structure of an event generator

The factorization theorem for hard processes [58] is the main theoretical justification for the approach adopted by QCD Monte Carlo event generators. Following the prescriptions of the theorem, an ep scattering process, characterized by a hard scale, can be factorized into the following separate stages (Fig. 2.21):

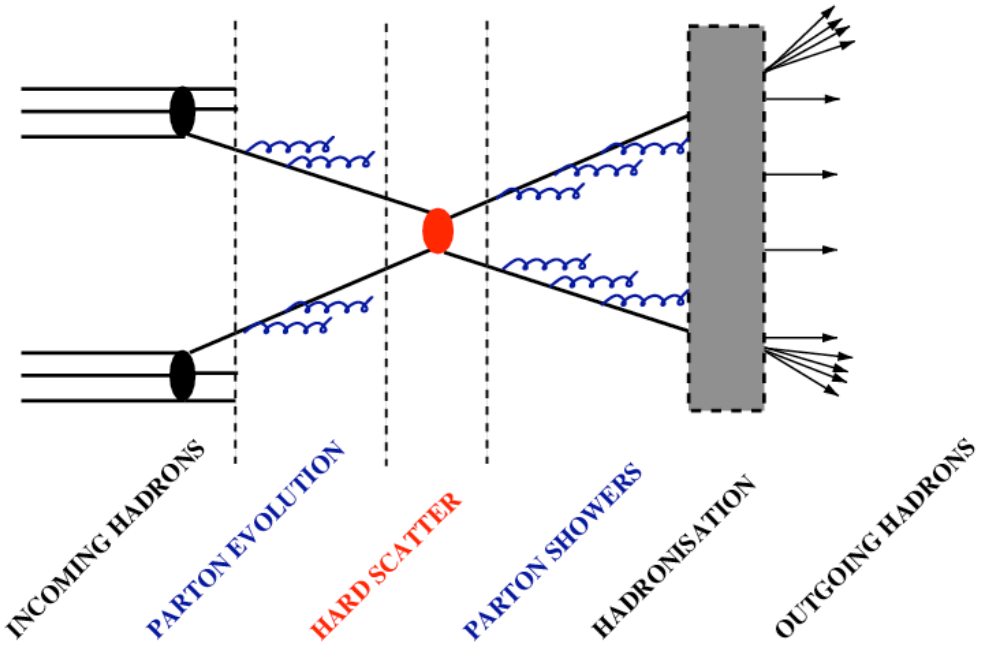

Figure 2.21: *General structure of the leading-order plus parton-shower PYTHIA MC generator.*

- *hard sub-process*: it is the interaction between a parton, extracted from the proton, and the photon, or a photon constituent in resolved photon events. This process can be calculated in a fixed order perturbative expansion if it involves a hard scale μ ($\mu \gg \Lambda_{QCD}$);
- *initial* and *final state radiation*: in processes involving charged and coloured objects, the topology of an event can be strongly influenced by the emission of gluons and photons in the initial or final state. These perturbative corrections are usually modelled by the so called *parton shower method*: the radiation is simulated by an arbitrary number of branchings of one parton into two, like $e \to e\gamma$, $q \to qg$, $q \to q\gamma$, $g \to q\bar{q}$. The kernel $P_{a\to bc}(z)$ of a branching gives the probability distribution of the energy sharing, with daughter b taking a fraction z and daughter c the remainder (1-z) of the initial energy E_a. The two daughters may branch in turn, producing other partons, and so on. Via *initial state radiation* a parton, having low space-like virtuality, radiates

time-like partons, increasing its space-like virtual mass. On the other hand, in *final state radiation* an outgoing virtual parton with large time-like mass generates a shower of partons of lower virtuality. The shower evolution is stopped at some fixed scale μ_0, typically of the order of 1 GeV;

- *hadronization*: the process in which colourless hadrons are formed starting from coloured partons, involving the phenomenological inputs described in 1.5.2.

- *beam remnant*: the interacting partons carry only a fraction of the initial beam energy, the rest is taken by the beam remnant. If the shower initiator is coloured, so is the beam remnant, which is therefore connected to the rest of the event and has to be fragmented and reconstructed coherently.

2.10.2 The detector simulation

All the event generators supported in ZEUS, like RAPGAP and DJANGOH (see Sect. 4.2.1) are gathered in a software programme called AMADEUS , see Fig. 2.22. The user can choose the event generator, which gives as output all the four-momenta of the particles produced in the hard scattering process and all the relevant kinematic variables.
The data produced by an event generator are the input to the ZEUS detector and the trigger simulation programme, MOZART [62]. MOZART is based on the GEANT [63] package, whose kernel contains a description of all the detector components, including the material they are made of, their shapes and positions. The programme traces the particles through the whole detector, simulating its response and taking into account physics processes such as energy loss, multiple scattering and particle decays in flight.
The events then pass through the CZAR [49] package, that simulates the trigger logic as implemented in the data taking.
As a final step, the generated sample is processed by the ZEUS reconstruction programme, ZEPHYR. This programme reconstructs the event variables, like particle momenta and energies, treating the data and the Monte Carlo in the same way. All the information coming from the different detectors making up ZEUS are taken as inputs by ZEPHYR.
ZEUS data are organized using the ADAMO [49] management system and used for the data storage in memory or on external media and for their documentation. Access to the data by users is done with the EAZE programme. The ZEVIS event display generates bi-dimensional graphical representations of the real or simulated events.

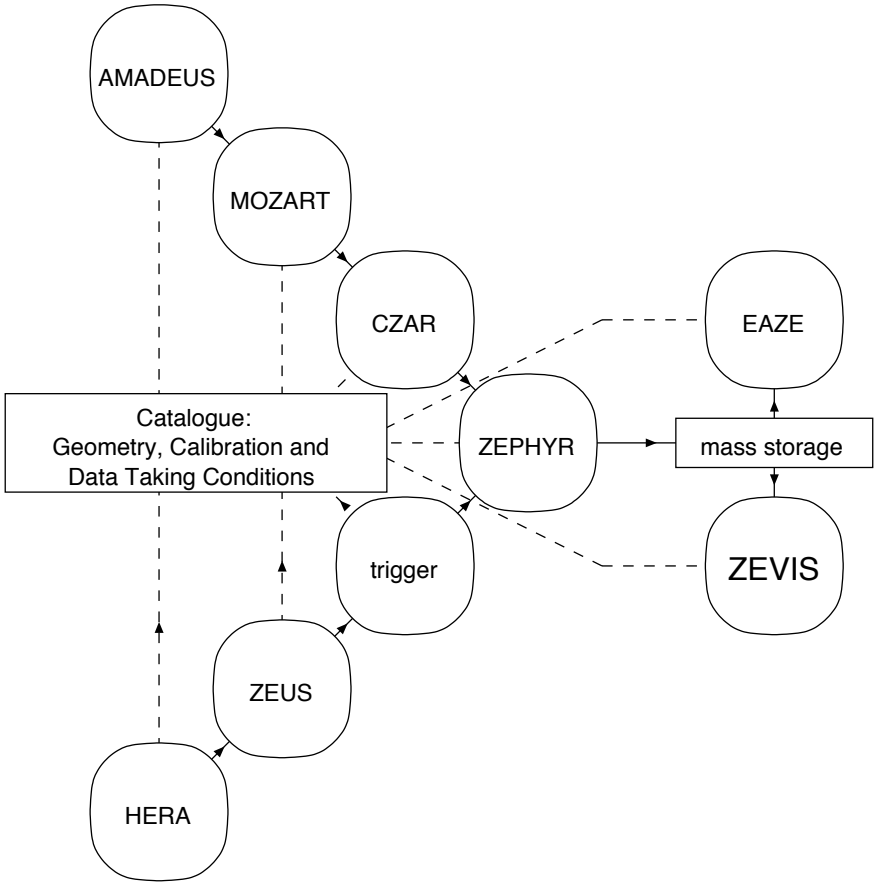

Figure 2.22: *A schematic diagram of* ZEUS *data and Monte Carlo reconstruction chain*.

Chapter 3

Analysis overview

3.1 Physics goal

The present analysis is devoted to measure the heavy quarks contribution to the structure function F_2, that is to extract the quantities $F_2^{b\bar{b}}$, $F_2^{c\bar{c}}$, in $e^- p$ deep inelastic scattering events at HERA.
In order to select events with an high contents of heavy quarks, the presence of at least *two* jets in each event has been required.
The probed kinematic range is $22 < Q^2 < 1000$ GeV^2, $0.02 < y < 0.7$; the reasons for such a choice will be illustrated in the following.

In order to get more accurate measurements, one prefers to extract the ratio between the heavy quarks contribution over the inclusive structure function F_2, that is the ratios $F_2^{b\bar{b}}/F_2$, $F_2^{c\bar{c}}/F_2$; in such a way most part of the systematic errors cancels in the ratio.
The estraction of the differential b and c cross section as a function of x and Q^2 has also been performed. But in this case the relevance of the missing estimation of the systematic errors could be sizable.

In this thesis, the so-called Impact Parameter (IP) method will be used. Method and measurement are alternative to those already exploited, e.g. D mesons reconstruction and jet plus p_t^{rel} for the charm and beauty estimation respectively.

3.2 Measurement strategy

In order to measure the structure functions $F_2^{b\bar{b}}$, $F_2^{c\bar{c}}$, one should count the events in which an heavy quarks has been produced in the hard scattering. The key point is hence to discriminate tracks coming form a beauty or a charmed hadrons from tracks coming from light hadrons, only by means of topological features of the events.
The advantages of this approach are obvious: one can avoid complicate kinematical reconstructions of decaying hadrons, access a large phase space region and avoid hard selection cuts.
On the other hand, high performances of the tracking devices and good knowledge of the tracking tools become aspects more important with respect to the standard analysis; furthermore, having to deal with high precisions measurements of the track (the order of $\simeq 100\mu m$), this techninque acquires a stronger dependence on the event reconstruction and on the reliability of the detector simulation.

3.2.1 Definition of Impact Parameter

The Impact Parameter (IP) is a geometrical quantity that could be defined for each well reconstructed track and is the main tool of the present measurement. So first of all, let us illustrate what the impact parameter is, with the help of the Fig. 3.1. The "distance of closest approach" (DCA) is defined as the point of the reconstructed track helix closest to the interaction point. For each track, the impact parmeter is basically the distance of closest approach (DCA) projected into the transverse plane, that is the plane orthogonal to the beams direction.

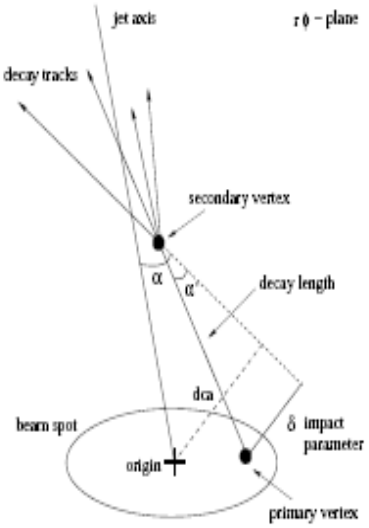

Figure 3.1: *Schematic representation of the quantities outlined in the text: the distance of closest approach, the beam spot and the impact parameter.*

3.2.2 Lifetime signature: the impact parameter method

The main quantity to distinguish heavy quarks from background is the relative long lifetime of heavy flavoured hadrons. The lifetime can be translated to a measurable quantity using the decay length of the boosted hadron:

$$l = c\tau\beta\gamma, \tag{3.1}$$

where τ is the lifetime in the particle rest frame and $\beta\gamma = |\vec{p}|/m$ denotes the boost of the particle relative to the laboratory frame. The probability that a hadron with characteristic decay length l traverses at least a laboratory distance L between its production and decay is:

$$P(L) \propto \exp(-L/l). \tag{3.2}$$

For experimental reasons the measurement of the impact parameter could reach the precision needed only in a plane perpendicular to the beam axis. The longitudinal size of the crossing particle buches is much much larger than the transverse sections, so along the beam directions the interaction point is reconstructed with a precision of the order of several centimeters. Therefore, only the $r\phi-$ projection

$$L_t = L\,\sin\theta, \tag{3.3}$$

where θ denotes the polar angle of the decaying hadron, is relevant here.
The $impact\ parameter$ of a particle coming from the hadron decay is the closest distance in the $r\phi$ plane, between the decay particle's trajectory and the production point of the decaying hadron and is given by

$$\delta = L_t\,\sin\alpha. \tag{3.4}$$

Here α is the angle in the $r\phi$-plane between the hadron direction and the direction of the decay particle.
The difference in lifetime for charm and beauty-flavoured hadrons leads to significantly different δ spectra, the large δ region beeing dominated by the heavy quarks. This is shown in Fig. 3.2, that compares the normalized IP distributions for beauty, charm and light quarks as predicted by the MC.

In principle is hence possible to distinguish the heavy hadrons from background profiting of the correlation between their lifetime and the IP of the track of their decay products: the longer the heavy hadron's lifetime, the larger is the track's IP.
One has, of course, to isolate the real signal from long lived particles not containing heavy quarks, as e.g. the Kaons. This can be achieved selecting tracks whit IPs in a suitable range. This important requirement, as well as other requirements, will be discussed in the section 4.4.2. In contrast to an explicit decay length analysis, no knowledge of the hadron decay vertex is required and, therefore, a reconstruction of secondary event vertices is not necessary.

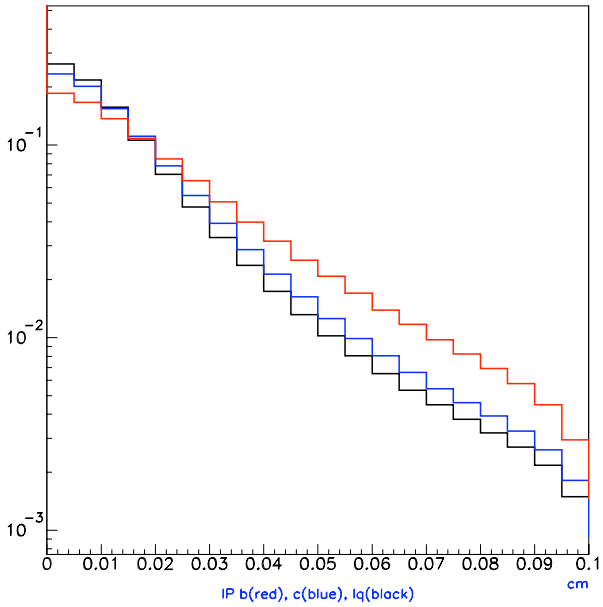

Figure 3.2: *Normalized distributions of the impact parameter for tracks originating from charm decays (blue line), beauty decays (red line) and light quarks (dark line), as predicted by* DJANGOH *MC*.

3.2.3 The signed IP: the jet-track association

It is possible to further improve the discriminating power of the IP defining a signed impact parameter (sIP). This can be done using the jet to which the charged particle belongs. In each event, the jets are searched and reconstructed by dedicated software algorithms that will be illustrated in the following (Sec. 3.4.3). If jets are present in the event, one can set a procedure in order to state if a track could be associated to a jet. Then the IP sign is set as positive if the intercept of the track with the jet in the $r\phi$-projection is downstream of the primary vertex, negative otherwise (see Fig. 3.3). A positive sign means that the particle crosses the jet, while a negative sign means the track crosses the interaction point with a direction opposite to the jet one.

Experimentally, the procedure is as follows :

1. first of all one computes for each track the the distance between the track and the reference jet in the $r\phi$ plane:

$$\Delta R_{track-Jet} := \sqrt{(\Delta\eta)^2 + (\Delta\phi)^2}$$

   where $\Delta\eta = \eta_{jet} - \eta_{track}$, $\Delta\phi = \phi_{jet} - \phi_{track}$;

2. all the tracks with $\Delta R < 1$ are associated to the reference jet;

3. then one computes the scalar product $\hat{U}_{track-Jet}$ between the versor of the track's DCA, $\hat{n}_{track}$, and the direction defined by the jet axis $\hat{n}_{Jet}$, both projected in the transverse plan:

$$\hat{U}_{track-jet} := \hat{n}_{track} \cdot \hat{n}_{jet}$$

4. finally the sign of the IP is defined as the sign of the scalar product just computed:

$$sIP = sign(\hat{U}_{trk-Jet}) \cdot |IP|$$

In this analyisis it has been chosen to perform the association procedure *only with the most energetic jet* in the event. This because the jet coming from the hadronisation of the heavy quarks is expected to be more energetic and more collimated with respect to the jets coming from radiated gluons or light quarks.

Tracks originating from long living hadrons are expected to produce impact parameter distribution tending towards positive values: the hadron boost set the decay products to have their direction similar to the jet direction. On the other hand, track from light quarks are expected to deliver signed impact parameters distributed symmetrically around zero. The width of the distribution is related to the detector sensitivity and reflects the finite resolutions for tracks and vertex reconstruction.

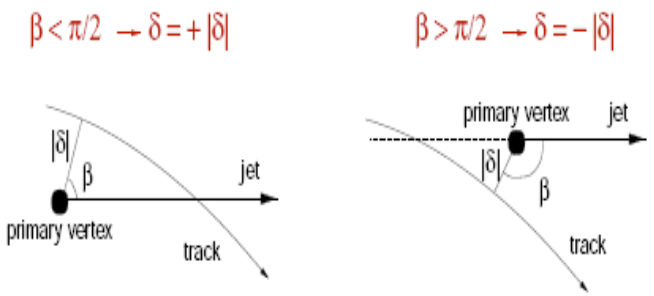

Figure 3.3: *Sketch of the impact parameter, δ for a generic track. If the track intercepts the jet axis downstream the reference point, the impact parameter has positive sign, negative otherwise.*

3.3 Smearing the Impact parameters

The extraction of the b and c fractions using the impact parameter technique relies on the Monte Carlo description of the track parameters. Unfortunately the available MC does not provide a good description of these variables. This disagreement has clearly come out in different analyses carried out by various ZEUS Collaboration members. Fig. 3.4 shows the poor description of the signed IP distribution obtained when using a PYTHIA photoproduction Monte Carlo sample compared with the 2004 data in a previous analysis of ZEUS Collaboration concerning beauty exctraction in di–jet events with the IP plus p_t^{rel} technique [112]. On the left side of Fig. 3.6 similar disagreement is evident for the IP distribution predicted by the ARIADNE MC compared with the 2005 DIS events subject of this analysis.
In general the data impact parameter distribution is significantly wider than that in the MC. There are several reasons for this disagreement:

- the dead material is not simulated accurately enough in the Monte Carlo;
- the intrinsic hit and track resolutions implemented in the Monte Carlo simulation do not correctly reflect the real tracking detector resolution;
- the current implemented alignment of the Micro Vertex Detector has still to be improved.

In order to improve this status, background studies have been performed [112]: a refined reweighting has been tuned on an inclusive sample of light flavour MC to be compared with the 2004 data.

3.3.1 Double convolution fit

The resolution of the tracking system can be expressed as:

$$\sigma(p_T)/p_T = ap_T \oplus b \oplus c/p_T \tag{3.5}$$

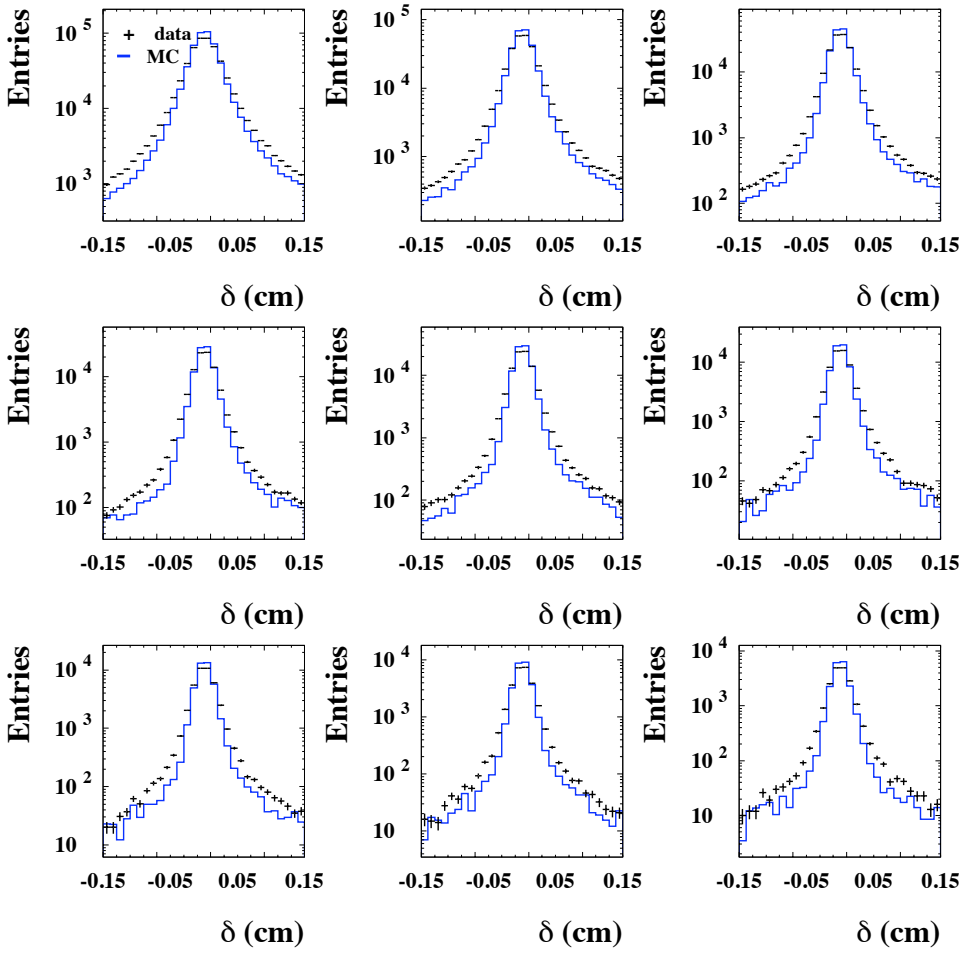

Figure 3.4: *The MC impact parameter distributions (histograms) compared with 2004 data (black crosses), in different P_T bins (the P_T range considered is $0.5 < P_T < 5$ GeV, the P_T bin size is 0.5 GeV).*

where the first term is related to the intrinsic track and hit resolution, whilst the second and third terms are related to the multiple scattering. It is therefore useful to analyze the impact parameter spectrum in different p_T bins. The multiple scattering is particularly expected to be the phenomenon less under control or worse simulated. In order to determine the correct smearing to apply to the MC, different functional forms (e.g. Gaussian, double Gaussian, Breit-Wigner, convolution of Gaussian with exponential) were tested to fit the negative side of the signed IP distribution in the data (the total distribution is slightly asymmetric towards positive values due to physics processes like K decays). The best fit to the data is found to be a double convolution of MC with a Gaussian and a Breit-Wigner: if F in the original IP distribution in the fitted range, the functional form of the new distribution is obtained as:

$$F_{fit}(x) = \int dy \int dz F(z)\mathbf{B}(y-z)\mathbf{G}(x-y) \tag{3.6}$$

where B indicates the Breit-Wigner function and G is the Gaussian function. In order to determine the precise values for the widths of the two distributions, different combinations of the σ of the Gaussian and the Γ of the Breit-Wigner distributions were tested in order to find the minima. The χ^2 of the fit for each p_T bin is found to be approximately constant as a function of the Gaussian σ, whilst it shows a strong dependence on the Breit-Wigner Γ. The minima were determined considering two-dimensional distributions; the χ^2 of the fit was plotted as a function of the Gaussian σ keeping the Γ of the Breit-Wigner at its minimum; the Gaussian width was determined by fitting the local minimum area with a parabolic fit. The same procedure was adopted to extract the minimum of the χ^2 as a function of the Γ of

the Breit-Wigner.

The distributions of the above minima as a function of p_T, have been fitted using a combination of an exponential and constant function in the case of the Breit-Wigner and with an exponential term for the Gaussian; the result can be written as:

$$\Gamma_{BW}(P_T) = \exp(a + b \cdot P_T) + c \tag{3.7}$$

$$\sigma_{Gauss}(P_T) = \exp(d + f \cdot P_T) \tag{3.8}$$

where the Breit-Wigner parameters are $a = 1.9791, b = -0.83335$ and $c = 0.001$ cm, whilst the Gaussian fit parameters are $d = 0.0037817$ cm, 0.00039859 cm. These values are used to correct the impact parameter measurements as follows:

$$IP_{smeared} = IP_{original} + sme_{BW} + sme_{Gauss} \tag{3.9}$$

where:

$$sme_{BW} = N^{BW}_{RAN}(N^{UNI}_{RAN}) \times (\exp(a + b \cdot p_T) + c) \times const. \tag{3.10}$$

and

$$sme_{Gauss} = \exp(d + f \cdot p_T) \times N^{GAUSS}_{RAN} \tag{3.11}$$

In Eq. 3.10 N^{BW}_{RAN} is a random number generated with Γ_{BW} equals to 1, whilst N^{UNI}_{RAN} is a uniformly generated random number from 0 to 1. In Eq. 3.11, N^{GAUSS}_{RAN} is a random number generated according to a Gaussian distribution with σ_{Gauss} equals 1.

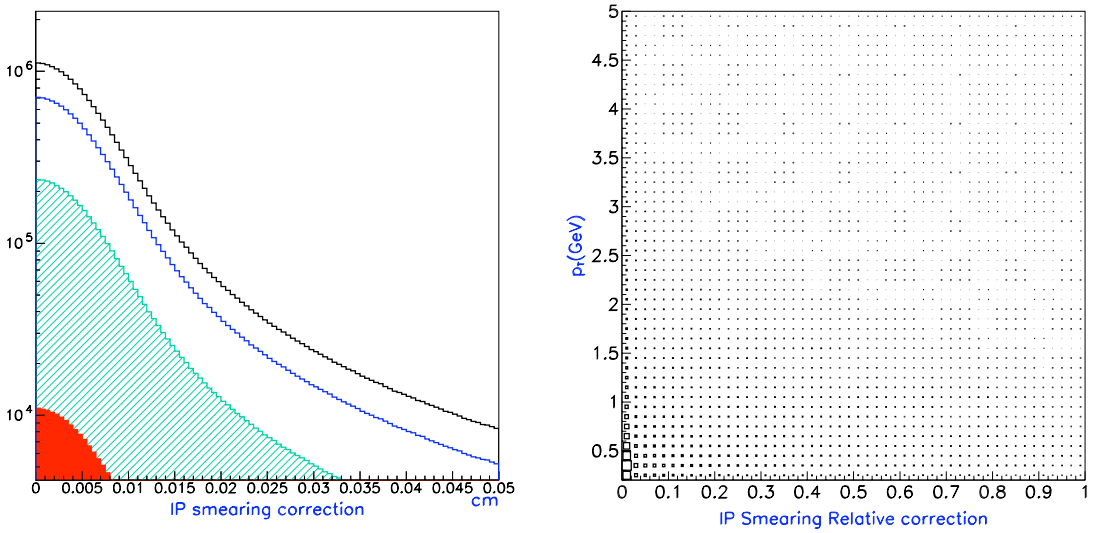

Figure 3.5: *Absolute value of the corrections applied to the impact parameters by the smearing procedure (left) and scatter–plot of the entity of the smearing correction to the IP in percentage versus the transverse momentum of the relative track.*

For about half of the selected tracks, the absolute value of the corrections applied to the impact parameters by the smearing correction is below $100\mu m$ as can be seen in Fig. 3.5. The same figure also shows the transverse momentum of the track as a function of the percentages of the smearing correction with respect to the IP of the relative track. The randomization of the smearing parameters ensures an indipendent sampling of the applied corrections.

Although the IP smearing applied on the trial sample is effective, as can be seen on the right side of Fig 3.6, in the present contest the improvement is not so stunning. Even if the agreement is largely improved after the smearing, the χ^2 per degrees of freedom between the data and MC remains large (> 5). Probably a new tuning on an inclusive DIS sample would provide better results.

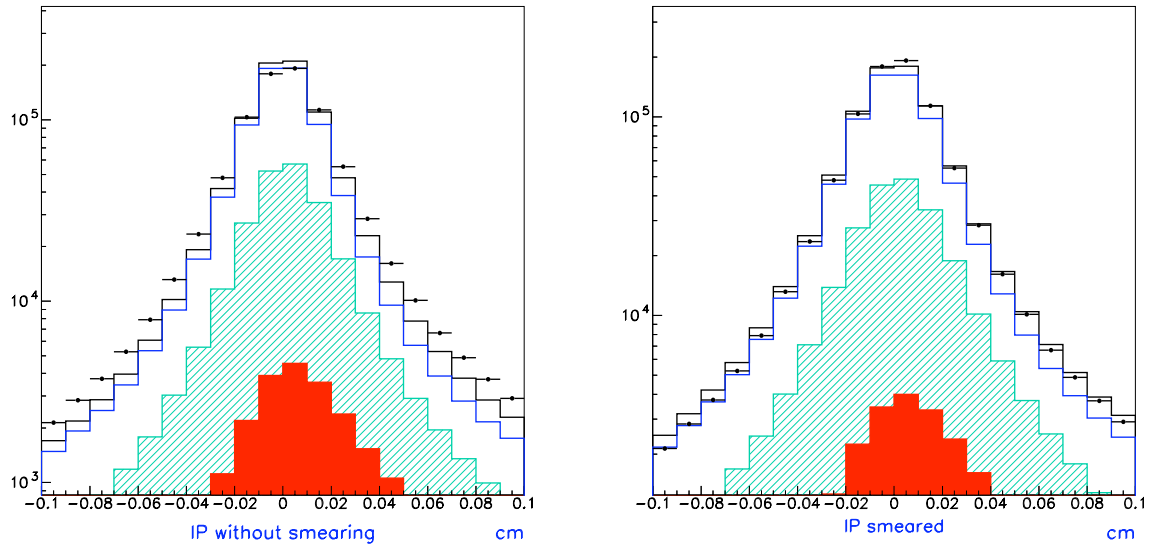

Figure 3.6: *Inclusive MC impact parameter distributions (hatched histograms) compared with 2005 data (black dots) analysed in the present work, without smearing on the left side, and after the smearing, on the right side. The smearing procedure illustrated in the text The inclusive MC is built with the method explained in 4.2 and plotted after the whole selection of 4.3; beauty (red), charm (hatched green) and light quark (blue) components are shown separately.*

3.4 Physical observables

The computation of the signed impact parameter requires three ingredients: a well reconstructed track, the knowledge of the spatial point in which the interaction occurred and a jet.
All of them play a fundamental role in this analysis, so in the following sections the software and hardware devices related to their measurements will be reviewed.

3.4.1 Tracks

The development of the package used in ZEUS for the reconstruction of tracks and vertices inside the detector begun in 1990 and is still undergoing developments because of the different configurations of the ZEUS tracking system. All reconstructed tracks use mostly hits from the CTD although information coming from other tracking devices (MVD, SRTD, RTD and FTD1) are taken into account.
The reconstruction of the tracks and vertices can be summarised in three basic steps:

- pattern recognition
- track fit
- vertex finding

which will be discussed in some detail in this chapter.

3.4.1.1 Pattern recognition

Due to the axial magnetic field around the interaction region, the particle trajectory is to first approximation a cylindrical helix with axis along Z. In the pattern recognition phase in order to describe the helix in 3 dimensions the following parameters are used (see Fig. 3.7):

- two parameters in the XY plane: (a_1, a_2)
- two parameters in the sZ plane: (p_1, p_2), where s is the path length. For a 2D s path along the circumference, $Z = p_1 + sp_2$, where $p_1 = z$ at (x_0, y_0) and $p_2 = \cot\theta$; (x_0, y_0) is reference point for the trajectory in the XY plan, corresponding to the outer hit.

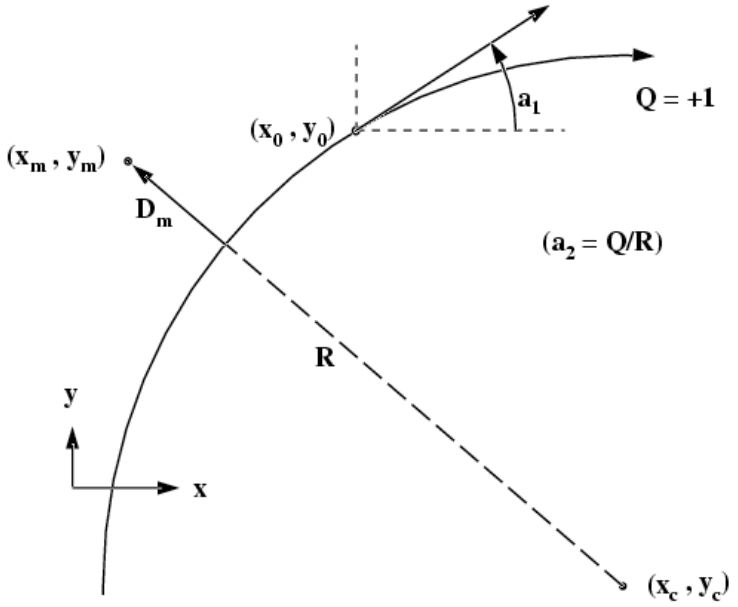

Figure 3.7: *Parametrization used in Pattern Recognition in VCTRAK. The reference point for the trajectory is* (x_0, y_0)*;* (a_1, a_2) *are the two fit parameters in the* XY *plane.*

This method of track parametrization is faster than the 5-parameter fit used in the final track reconstruction; the speed of the execution is important in this phase because this algorithm is also implemented at the third level trigger where it is necessary to process a huge quantity of information (all possible hit combinations) in a limited amount of time. Pattern recognition begins at the outer point of the tracking detectors and goes inward, i.e. it starts in the outer SuperLayer (SL9) of the CTD and follows inward through the MVD module layers. Of all track segments found, only track segments with at least 4 hits are kept.

3.4.1.2 Track fit

In the region around the interaction point the magnetic field generated by the solenoid is almost parallel to the CTD axis leading to a parametrization like the one sketched in Fig. 3.8;

at this stage the helix is described by 5 parameters calculated with respect to a reference point (X_{ref}, Y_{ref}):

1. ϕ_H, azimuthal angle of the helix tangent at the distance of closest approach to the straight line $x = y = 0$;
2. Q/R, where Q indicates the track charge (sign) and R the local curvature radius;
3. QD_H, distance of closest approach to the straight line $x = y = 0$;
4. Z_H, z coordinate of the track at the distance of closest approach to the straight line $x = y = 0$;
5. $\cot\theta_H$, where θ_H is the polar angle of the track.

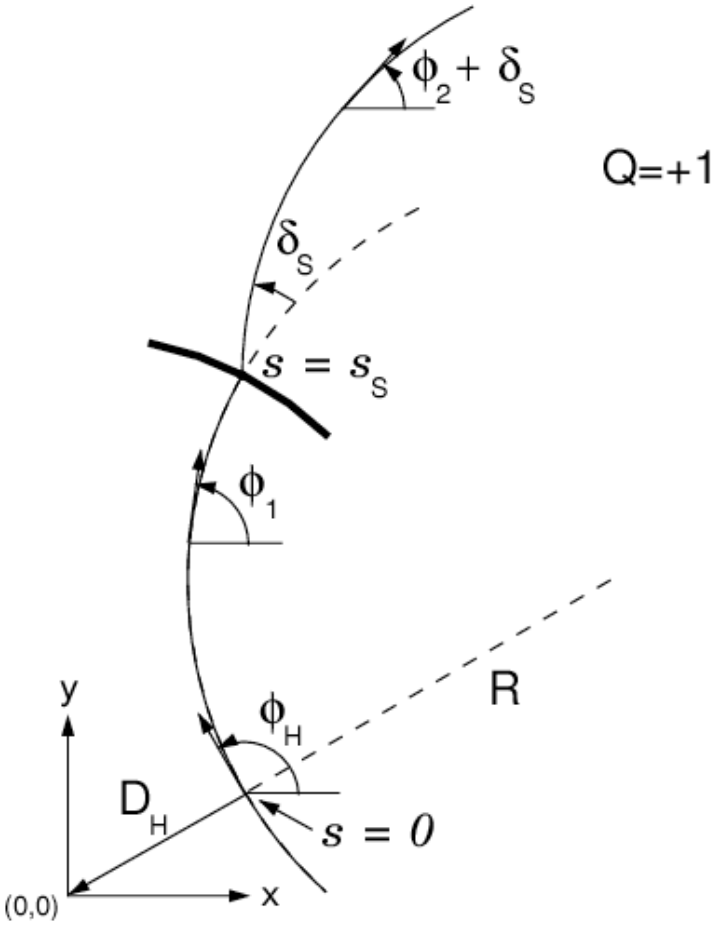

Figure 3.8: *VCTRAK parametrization used in the track fit*.

The coordinates of the point of closest approach to the reference point can be written as:

$$\begin{cases} X_H = X_{ref} + QD_H \sin\phi_H \\ Y_H = Y_{ref} - QD_H \cos\phi_H \\ Z_H \end{cases} \tag{3.12}$$

The path length of a generic trajectory in the XY plane is given by:

$$s(\phi) = -QR(\phi - \phi_H) \ . \tag{3.13}$$

The coordinates at a generic point of the helix can be parameterized as:

$$\begin{cases} X = X_H + QR(-\sin\phi + \sin\phi_H) \\ Y = Y_H + QR(+\cos\phi - \cos\phi_H) \\ Z = Z_H + s(\phi)\cot\phi \ . \end{cases} \tag{3.14}$$

The three-momentum components are given by:

$$(p_x, p_y, p_z) = (p\cos\phi\sin\theta, p\sin\theta\sin\phi, p\cos\theta) \ . \tag{3.15}$$

3.4.1.3 Vertex finding

The track parameters obtained in the fit phase are the starting point for the vertex finding. The goal of the pattern recognition phase for the vertices is to find the primary vertex. Each vertex is defined by the trajectories of the tracks

"forced" to its position. A detailed description of this process can be found in [91]. The tracking package can be run in two modes:

A) "primary vertex only" mode which does not reconstruct secondary vertices.

B) "multi-vertex" mode which finds a primary vertex compatible with the existence of secondary vertices. The execution time is obviously longer but there are some advantages:

- many events in which the primary vertex is not revealed in the A) mode now can be reconstructed (usually they are events with a low multiplicity of primary tracks and many secondary tracks);
- the primary vertex is identified in a "cleaner" way because tracks contaminating the primary vertex reconstruction now are associated to secondary vertices.

3.4.1.4 MVD information

At the end of 2002 a new version of the tracking software including the MVD hits became available; the improvements with respect to the old version which used only CTD information are the following:

- track finding efficiency: using the MVD already in the pattern recognition stage, an efficiency improvement of $\sim 3\%$ can be obtained, from 93.5 % using CTD only information to $\sim 97\%$ including also the MVD information;
- trajectory precision: MC studies have shown that the precision in the trajectory determination is significantly improved;
- vertex finding: the primary vertex resolution is improved as well as the efficiency in the identification of secondary vertices.

3.4.2 The reference point

The impact parameter is defined with respect to the interaction point. But there are two choices in locating the interaction point experimentally: one can naively consider the primary vertex (PV) as the point where the interaction occurred, as determined by the reconstruction packages of the global tracking, on an event-by-event basis. In such a way there is strong dependence on the analysed event, and the error on its determination could vary a lot. But if the primary vertex spread in the transverse plane (XY) is smaller than its reconstruction resolution, the accuracy on its position determination can be improved by replacing its value on an event-by-event basis with its average over many events, technically named *beam spot* (BS). In order to achieve the best resolution for the x and y coordinates, an average vertex position is then determined run-by-run, and a beam spot is calculated averaging the primary vertex positions for all the events in a run. Some quality cuts are applied to the tracks participating in the fit as well as adequate background reduction cuts:

- existance of the primary vertex
- RCAL time - FCAL time $>$ -8 ns. This cut reduces proton beam-gas events and proton beam halo muons;
- CAL $E_T > 5$ GeV and CAL $P_T < 5$ GeV. This cut reduces proton beam-gas events. Here E_T is the transverse energy in the calorimeter, whilst P_T is the sum of the momentum vectors of all CAL deposits projected onto the xy plane;
- $E - p_Z > 10\,\text{GeV}$
- At least four tracks fitted to the primary vertex;

The advantage in using an averaged position of the PV as interaction point is obvious, being the precision with which it is known much higher. Considering the BS as the interaction point, the total error could be greatly limited, and its dependence on the reconstruction tools or on peculiar features of the event becomes smaller.

The beam position in x and y, determined from an average of 2000 reconstructed event, provides quite a precise and unbiased estimation of the event vertex in the transverse plane: the transverse width of the HERA beams at the interaction point has been estimated to be about $\sigma_x \simeq 110\ \mu m$ and $\sigma_y \simeq 30\ \mu m$. These are the dimensions of the beam spot width taken into account.
The statistical contribution coming form its determination over the sample in which it is computed is about one order of magnitude lower.

All runs within the same HERA fill are treated as a single run. The last few events at the end of a fill are added to the previous interval and the distributions are re-fitted.

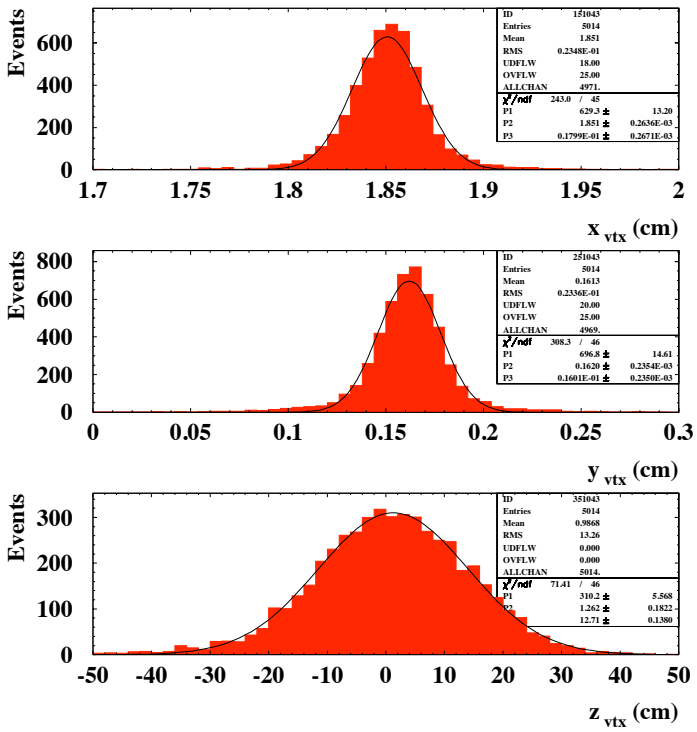

Figure 3.9: *Distribution of the primary vertex coordinates in an example run (∼5000 events taken during the 2004 were selected after applying the background rejection and quality cuts). A Gaussian fit was used to extract the mean beam spot values, restricting the fit range to* $\pm 2\sigma$.

For each run the beam spot position is determined applying a Gaussian fit to the primary vertex coordinate distributions (see Fig. 3.9). Different fitting ranges have been tested ($\pm 2\sigma$, ± 4 bins from the mean, free fit range), obtaining differences in the mean positions of the order of few μm, meaning that the systematic effects from the chosen fit procedure are of the same order of the statistical uncertainties.

3.4.2.1 Time and z dependence of the BS

The beam spot is not always in the same position, as shown in Fig. 3.10 where the HERA and H1 measurements are reported. The vertical and horizontal positions of the beams vary significantly. The beam orbits can change between the fills due to the fact that the focussing superconducting magnets before the interaction point [37] move, being subject to magnetic forces. Also temperature effects can occur in the magnetic bridges leading to a shift up to 1 mm. The orbits can drift inside each fill as well; the reasons are again temperature effects induced by the magnet bridges and also luminosity, background and polarization tuning.

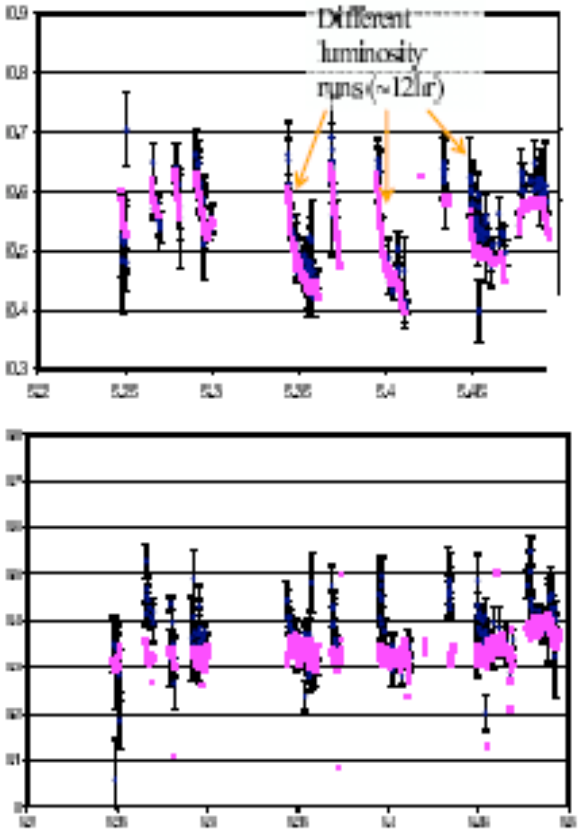

Figure 3.10: *HERA (grey) and H1 (black) vertical (top) and horizontal (bottom) beam position measurements (in mm) as a function of time (months). The periodic structure of the plot reflects the different machine fills.*

3.4.2.2 Time dependence

The average position of the primary vertex described in section 3.4.2 can drift during a fill (see Fig. 3.10). In order to quantify this effect, a study [112] has been performed on the 2004 data, limiting the study to large statistics consecutive runs inside the same fill. In Fig. 3.11 the primary vertex coordinates are plotted as a function of the $Run\ Number$ (time-dependent); the observed variation inside each run was of the order of $\sim \pm 20\ \mu m$ for both the x and y coordinates. These variations have been found to be small compared to the sigmas of the beam spot coordinates distributions (see Fig. 3.9), so no corrections are applied for this effect.

3.4.2.3 Z dependence

The beam and detector axes are not parallel along the longitudinal direction, producing a dependence of the primary vertex X,Y positions on the Z coordinate.
In Fig. 3.12 this effect is shown for a particular run taken during the year 2004: the variations can reach $\sim \pm 200\ \mu m$. Therefore this effect is not negligible and a correction is needed on the beam spot coordinates. A fit is then performed on the x vs z and y vs z distributions with a straight line. Then the obtained tilt-parameters $m_{x,y}$, Figs. 3.13 and 3.14, are used to correct for the primary vertex position The new coordinate positions are written as:

$$X_{BS}^{corr} = X_{BS} + m_{x,y} \cdot (Z_{PV} - Z_{BS}) \tag{3.16}$$
$$Y_{BS}^{corr} = Y_{BS} + m_{x,y} \cdot (Z_{PV} - Z_{BS}) \tag{3.17}$$

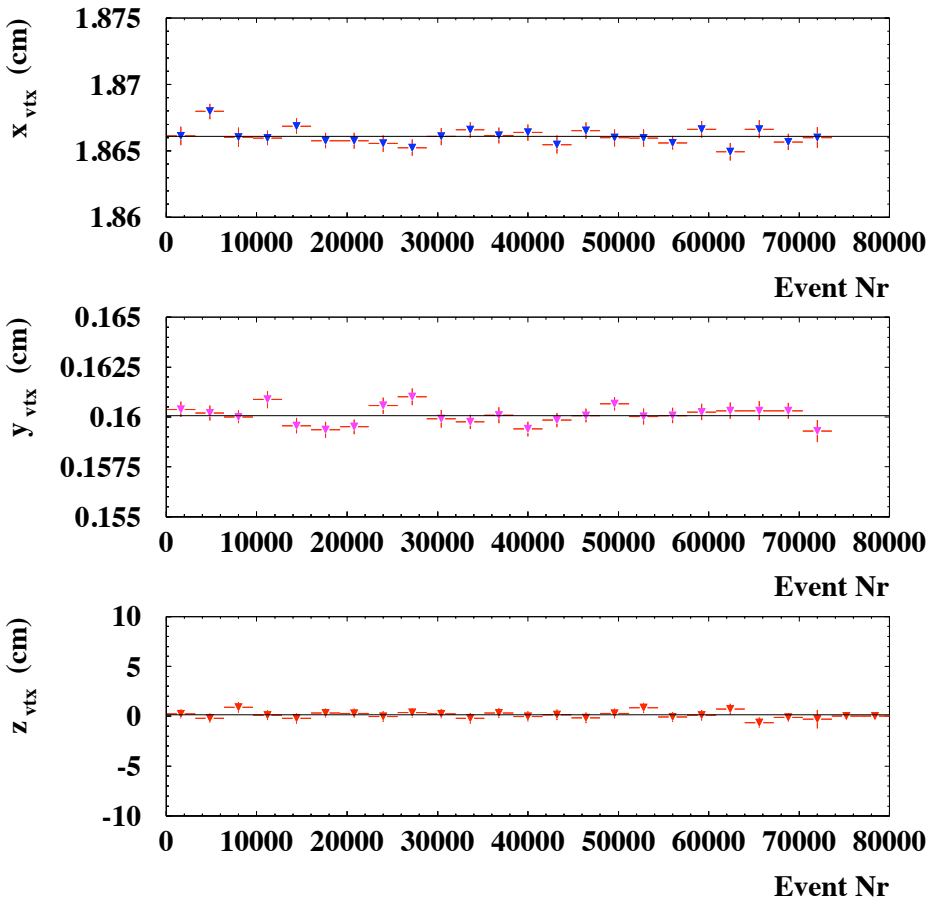

Figure 3.11: *Distribution on the vertex position in x (top, left), y (top, right) and z (bottom) in bins of approximately 500 events for one single 2004 run. Each of the measurements (triangles) corresponds to 200 events. The variation observed in x and y is of the order of* $\sim \pm 20\ \mu m$.

3.4.2.4 DAF Vertexing

A further refinement of the vertex position measurement is possible implementing the Deterministic Annealing Filter (DAF) procedure [68]. The main issue is to replace hard χ^2 cuts of the track fit by a smooth weight function, which is sharpened by iteratively tuning its parametrisation.
The potential benefit is a more robust determination of primary vertex. This technique is already adopted by other experiments experiments. In the present analysis the DAF vertexing has been adopted, setting it in the beam spot constrained mode.

The impact parameter used in this analysis will be always referred to the beam spot, corrected for the beam tilt. In order to refer the tracks to this reference point, all the tracks undergone the procedure to re–computing the coordinates of their helix.

3.4.3 Jet algorithm

The features of the jets in a hadronic final state are related to those of the partons from which they originate. However, jets are complex objects, and they are not uniquely defined in QCD: their definition relies on the algorithms used to reconstruct them. In the Snowmass workshop in 1990 [95] some criteria were fixed to be satisfied by every jet

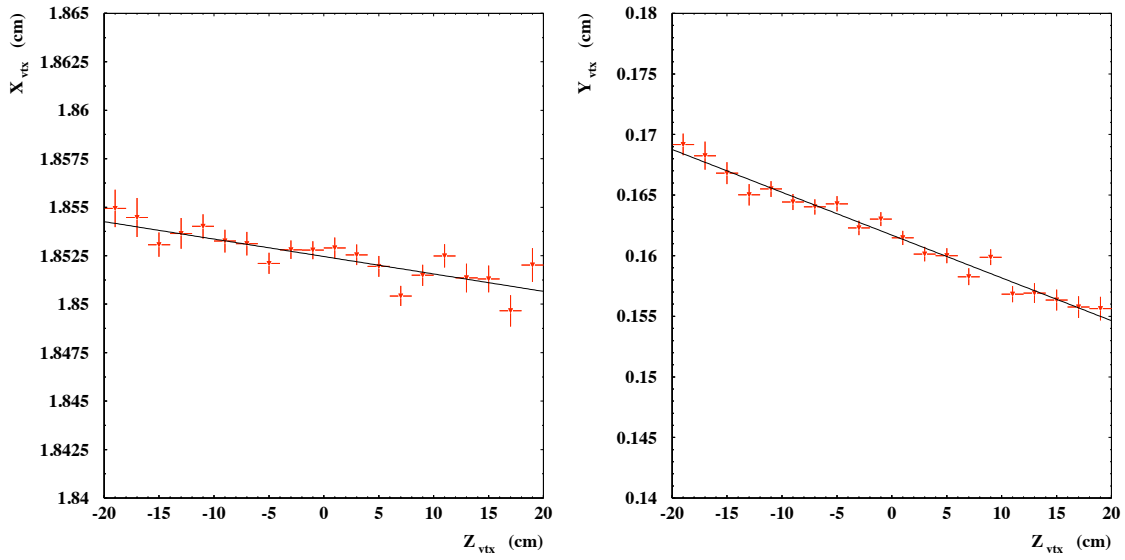

Figure 3.12: *Straight line fit for the x vs z (left) and y vs z (right) distributions. Only the central region around the mean value of the Z coordinate ($|Z| < 20$ cm) is shown.*

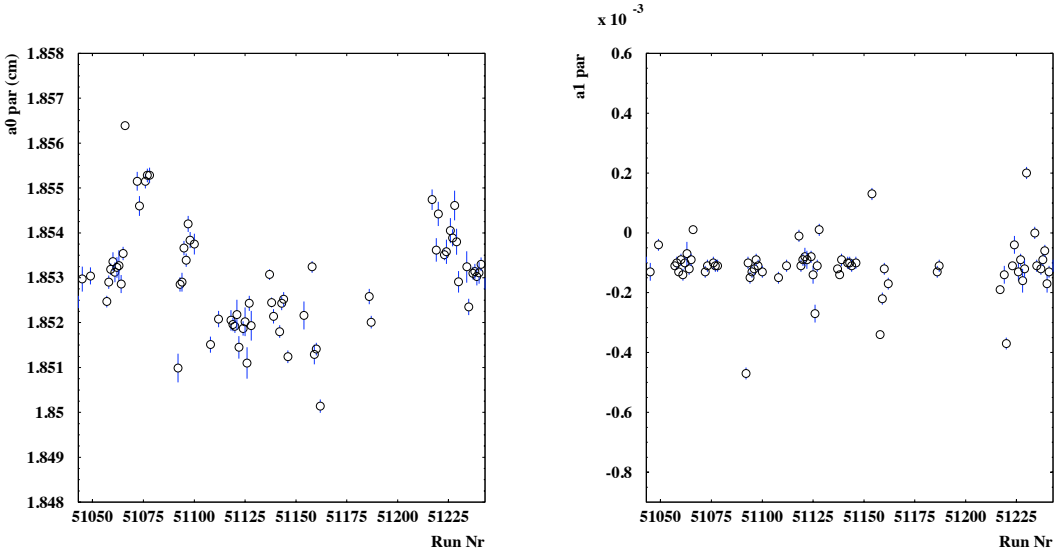

Figure 3.13: *Fit parameters for the x coordinate. On the left the off-set, on the right the slope coming from a linear fit.*

reconstruction algorithm. In particular, two requirements have to be fulfilled, in order to define an *infrared* and *collinear-safe* algorithm, reconstructing jets in the proper way:

- the results must be independent of the fact that one parton can split into two partons moving collinearly, or, from the experimental point of view, that a particle can release energy in two adjacent calorimeter cells. This dependence in fact causes collinear divergences in the theoretical calculations, which disappear if no distinction is made between two particles having energy $E_1 + E_2 = E$ and one single particle of energy E, moving in the same direction. From the experimental point of view, this means that the results are independent from the detector *granularity*;
- the results must be independent of the emission of very low energy particles; this fact causes infrared divergences in the theoretical calculations, removed by integration. In experiments these small energy deposits are related to the noise of the detector, removed by using appropriate thresholds or corrected by suitable algorithms.

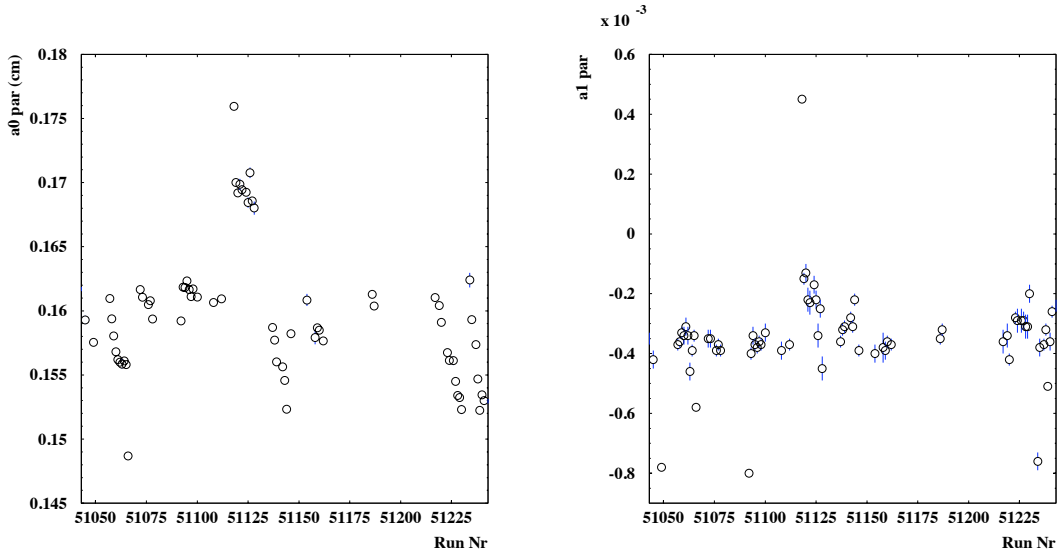

Figure 3.14: *Fit parameters for the y coordinate. On the left the off-set, on the right the slope coming from a linear fit.*

Jet algorithms for the analysis of photoproduction processes have to fulfill two further requirements: they have to treat the proton and, if present, the photon remnant in a proper way, that means, the remnants have to be separated from the jets and not influence their search. Moreover, in photoproduction processes in general the laboratory frame is different from the frame of physical interest (i.e. the γp centre-of-mass frame). Nevertheless, in DIS as well as in photoptoduction processes, the frame are Lorentz boosted along the beam direction with respect to the laboratory frame. Therefore the jet algorithm has to be independent of this kind of transformation: this can be done by reconstructing jets using their transverse energy in a pseudorapidity-azimuth plane ($\eta - \phi$).

In ZEUS jet reconstruction is performed through *cone* and *clustering* algorithms. The clustering approach has the advantages of unambiguously assigning objects, i.e. the treatment of overlapping jets is clear, and the assignment of hadrons to jets can be done using the same procedure both in theoretical calculations and in experiments. This is the reason why here a clustering algorithm has been used to reconstruct jets, namely the k_T algorithm [96].
The resolution variable used by the k_T algorithm to identify the jets is the relative transverse momentum, k_T, between particles. The use of this variable follows from the fact that, with the present understanding of perturbative QCD, the jets are not sprays of hadrons confined in cones of fixed angle. Soft hadrons produced coherently by the fragmentation of hard partons should be assigned to the jet of the hard parton nearest in angle, independently of the actual value of its angular distance [97, 98]. This means that the jets have an effective radius depending on the hardness of the jet itself and on the colour flow of the hard subprocess.
The clustering procedure of the k_T algorithm is performed using the following iterative procedure:

1. the final state is described through a set of four-momentum objects p_i. The initial p_i can be the single particle four-momenta or the energy deposits inside the calorimeter (which can be improved using the information reconstructed by the tracking devices). The masses of these objects $m_i = \sqrt{p_i^2} << |\vec{p_{Ti}}|$, where $\vec{p_{Ti}}$ is the transverse momentum of the i^{th}-object. The algorithm recursively groups pairs of objects to form new objects, merging objects with almost parallel momenta. A parameter R characterises the measurement of the "distance" between two candidate objects to be merged. Every i^{th}-object is characterised by its pseudorapidity $\eta_i = -\log(\tan\frac{\theta_i}{2})$, its azimuthal position ϕ_i and transverse energy E_T^i.

2. For each object it is possible to define:
$$d_i = E_{T,i}^2 \ , \tag{3.18}$$
which measures the distance from the beam-axis and for each pair:
$$d_{ij} = \frac{min\left(E_{Ti}^2, E_{Tj}^2\right)\left[(\eta_i - \eta_j)^2 + (\phi_i - \phi_j)^2\right]}{R^2} \tag{3.19}$$
where $R = 1$ is assumed in this thesis.

3. The quantity:
$$d_{min} = min(d_i, d_{ij}) \tag{3.20}$$
is determined.

4. If $d_{min} = d_{ij}$, the i and j objects are recombined into a new object. The recombination scheme used in this thesis, known as "E-scheme", combines the 4-momenta of i and j like:
$$P_k = P_i + P_j \tag{3.21}$$
and produces massive jets taking into account the masses of the tracks, assuming them to be pions.

5. If $d_{min} = d_i$, the i^{th}-object is removed from the list and is added to the final jet list.

6. Re-start from step 2.

This procedure is re-iterated until all the starting objects are processed.

3.4.3.1 Reconstruction of the hadronic system

The measurement of particles energy is fundamental for the reconstruction of the event properties. The energy resolution of the CAL (see Eqs. 2.9, 2.10) goes like $\sigma(E)/E \sim a/\sqrt{E} \oplus b$ improving as the particle energy increases, whilst the resolution of the tracking system behaves like $\sigma(P_T)/P_T \sim a \cdot P_T \oplus b \oplus c/P_T$ leading to better energy estimation for lower energy particles (see Fig. 3.15).

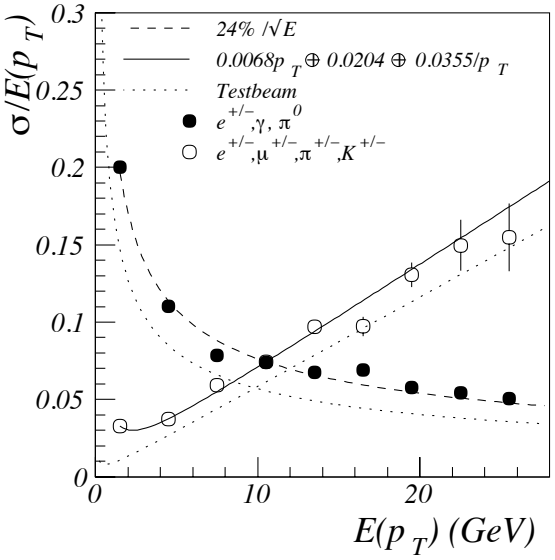

Figure 3.15: *Resolution from single particle MC simulation. The track transverse momentum resolution in the CTD (open markers) and the CAL energy resolution (full markers) are shown [94].*

The relationship between the CTD and BCAL resolution for electrons and charged hadrons as implemented in the MC is shown in Fig. 3.16 a) and 3.16 b), respectively, as a function of the polar angle. The angular range chosen lies within the BCAL and away from its edges. The BCAL energy resolution for electrons, in the energy range shown, is $\sigma(E_e) \approx 0.193E_e^{1/2}$ [99], where E_e is the electron's energy in GeV and the relationship assumes 1 X_0 of dead material. The equivalent formula for the hadronic energy resolution is $\sigma(E_h) \approx 0.35E_h^{1/2}$, where E_h is the hadron's energy in GeV. The CTD energy resolution for both electrons and charged hadrons is given by $\sigma(E) \approx 0.0058E^2 \sin\theta \oplus 0.0065 \oplus 0.0014/\sin\theta$, where E is the charged particle's energy in GeV and θ, its polar angle. The poorest CTD resolution corresponds to $\theta \approx \pi/2$, where the energy of electrons O(10 GeV) and hadrons O(15 GeV), or higher, begins to be better resolved by the BCAL.

To benefit from the most accurate energy determination in both energy ranges, the track reconstruction and the CAL energy measurement are combined into *energy flow objects* (EFOs) [94]. The tracking information is mainly used below 10-15 GeV and the calorimetry energy measurement above to form four-vectors representing the oriented energy deposit of particles traversing the detector.

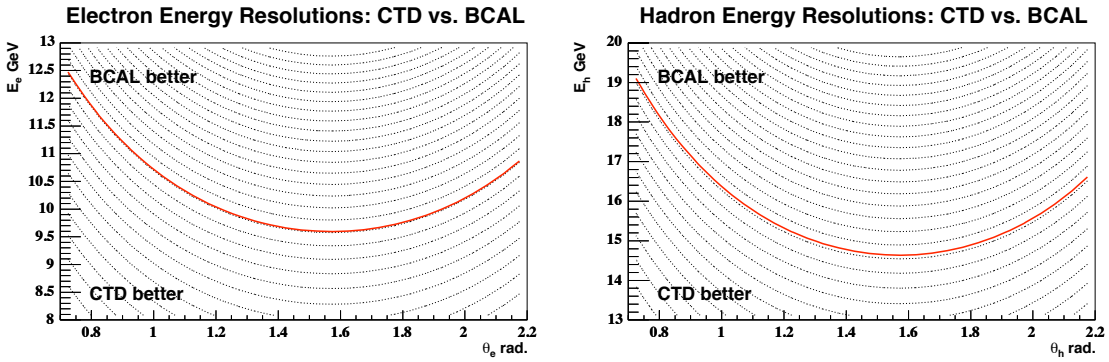

Figure 3.16: *The relative resolution of the* CTD *and BCAL for reconstructing the energy of (a) an electron, E_e and (b) a charged hadron, E_h, as a function of E_e and E_h and polar angle, θ_e and θ_h, for electrons and hadrons, respectively. The contours show the rate at which one reconstruction improves the other [99].*

3.4.3.2 Reconstruction of Energy Flow Objects (EFOs)

The use of EFOs is justified by the fact that the hadronic energy has both a charged particle and a neutral particle component. Both are measured by the calorimeter, but a large fraction of the charged particles are also measured by the tracking detectors. The use of the EFOs rather than the usual energy deposits in the calorimeter is also driven by the design of the ZEUS calorimeter (see Chapter, which is divided in three parts, the forward (FCAL), barrel (BCAL) and rear (RCAL) calorimeter. This spatial separation is a serious complication for a local clustering algorithm in handling the energy deposits of a single particle which is not confined within a single part of UCAL, since the energy will be split in two or more clusters.
Because of these complications, the EFO clustering algorithm is done in two steps [94]:

- the first stage of the clustering procedure is performed in each calorimeter layer separately. Each cell with sufficient energy is considered a candidate to be connected with one of its neighbours. The connection is made with the nearest neighbour with the highest energy or with the highest energy cell next to the neighbour. This procedure is repeated for each cell and produces a unique assignment of a cell to a so-called *cell island* (see Fig. 3.17).
- The second stage of the clustering procedure collects the cell islands belonging to a shower of a single particle or a jet of particles into a so-called *cone island*. The matching of cell islands starts from the outermost hadronic layer of the calorimeter and proceeds inwards. The angular separation between cell islands of different layers is calculated in $\theta - \phi$ space and translated to a probability according to a distribution determined by a single pion MC. Links with high probability are accepted provided that the probability is larger than a threshold. Once the linking procedure has been completed, the cone islands are generated by combining all calorimeter cells which point to the same cone island in the electromagnetic layer.
  The cone island centre is calculated as the energy weighted mean of the cell centres which have been corrected for the imbalance of the two photomultiplier measurements per cell. The energy weight is determined logarithmically rather than linearly to cope with the observed systematic bias due to the varying cell projectivity resulting from the CAL geometry.

For the track reconstruction (see Sec. 3.4.1), vertex fitted tracks with hits in at least 4 superlayers are selected in the transverse momentum range $0.1 < P_T^{track} < 20$ GeV. If the track has hits in more than 7 superlayers, the upper

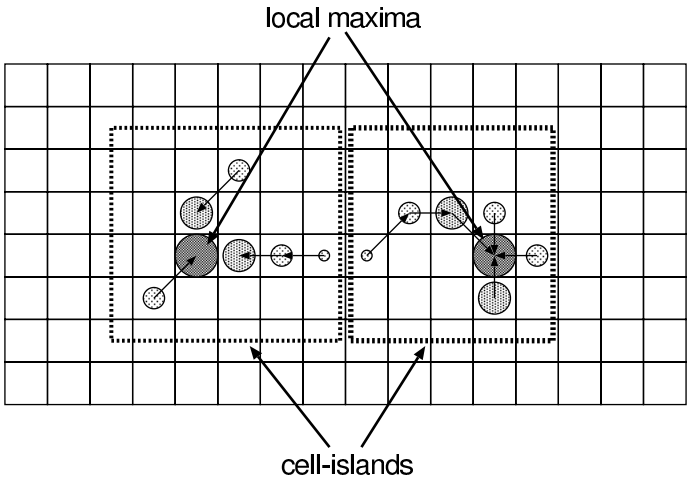

Figure 3.17: *A schematic diagram showing how cell-islands are formed.*

transverse momentum cut is raised to $P_T^{track} < 25$ GeV. The tracks are extrapolated to the inner CAL surface taking into account the magnetic field geometry and further into the CAL by a linear approximation using the track momentum vector at the CAL surface.

The matching of a track to a cone island uses the distance-of-closest-approach (DCA) method. A match is assigned

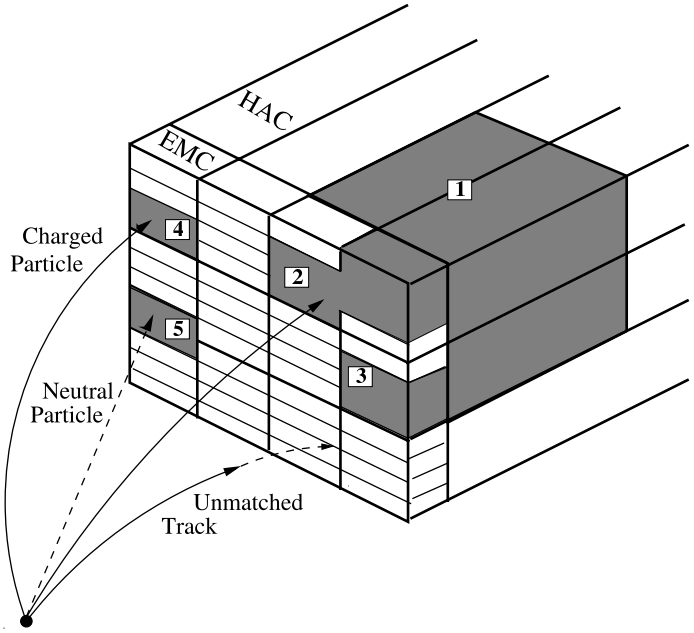

Figure 3.18: *Reconstruction of EFOs by a match between CAL cells clustered into cone islands (HAC cell 1 and EMC cell 2 and 3 are joined to form a cone island) and tracks. The different match categories of a charged particle (track is matched to cone island 4), neutral particle (no track is matched to cone island 5) and unmatched track are shown.*

between the extrapolated track and the cone island centre (see. Fig. 3.18) if the distance is closer than the cone island radius or a minimal radius of $r_{min} = 20$ cm optimized using MC simulations to maximize the track-island matching efficiency for single particle CAL clusters:

$$DCA \leq max(r_{min}, r_{island}) \ . \tag{3.22}$$

The set of associated track-islands, the EFOs, are then processed according to the following criteria:

- good tracks not associated to any calorimetric object are counted as charged particles, and the CTD information is used. The particle is assumed to be a pion;
- calorimeter objects not associated with any track are counted as neutral particles and the calorimeter information is chosen;
- for calorimeter objects associated with more than three tracks the calorimetric information is chosen.

In the case of one-to-one track-island matching, the track information is used instead of that from the UCAL if these two requirements are fulfilled: the energy deposit in the calorimeter has to be due to the associated track alone, and the momentum resolution of the track has to be better than the energy resolution of the corresponding calorimetric object (see Fig. 3.15), i.e. if both the following requests are satisfied:

- the track momentum exceeds the energy measurement in the CAL within the resolution on the measured ratio E_{cal}/p:
$$E_{cal}/p < 1.0 + 1.2 \cdot \sigma(E_{cal}/p) \ , \tag{3.23}$$
where $\sigma(E_{cal}/p) = \sigma(E_{cal}/p^2)\sigma(p) \oplus (1/p)\sigma(E_{cal})$.
- That:
$$\sigma(p)/p < \sigma(E_{cal})/E_{cal} \ , \tag{3.24}$$
where $\sigma(p)$ and $\sigma(E_{cal})$ are the resolutions of the momentum from the tracking and the energy in the CAL respectively.

Since muons are minimum ionising particles (MIPs) and lose their energy predominantly by ionisation, the measured energy in the CAL is not proportional to the momentum. Therefore, EFOs having the properties of a muon are treaated differently and the tracking information is favoured over the energy measurement if

- $E_{cal} < 5$ GeV;
- $E_{cal}/p < 0.25$;
- $P_T < 30$ GeV.

The more complicated 1-to-2, 1-to-3, 2-to-1 and 2-to-2 track-island matches are treated similarly to the 1-to-1 match, substituting the UCAL energy and the CTD momentum with the sum of the energies of the islands and the sum of the momenta of the tracks respectively.
Finally, in the case where a single track is matched to two or more islands, and the energy of the UCAL is favoured, the more precise angular information of the track is used.

Comparisons between data and MC simulations have shown discrepancies in the reconstruction of EFOs using calorimeteric islands [114, 115]. The main reasons are:

Energy loss in inactive material: Energy losses due to dead material are generally difficult to fully implement into the MC simulation. A detailed dead material map is available and has been used to write correction algorithms. The material constituting the beam pipe, the tracking devices and the solenoid correspond to a number of radiation lengths varying from 1 to 3 in the central part of the detector and the energy loss of the particles, especially of those having low momenta, can be significant in such a thickness. Since energy losses due to the presence of dead material are difficult to include with sufficient precision in the detector simulation, the correction is done offline, and it is parametrized as a function of the energy and of the polar angle of the particles.

Calorimeter geometry: The zones of the cracks between the calorimeter sectors are not well simulated and corrections are introduced offline.

Energy overestimation of low momentum hadrons: Protons and pions with momenta below ~ 1 GeV lose energy mainly through ionisation without hadronic interactions. In this case, the CAL is no longer compensating ($e/h \sim 0.6$). This effect causes an overestimation of the energy of low-momentum hadrons which has to be corrected.

Chapter 4

Data and MC sample

4.1 Data sample

The impact parameter for heavy hadrons is in the order of tens to hundreds of micrometers. To resolve these distances, high precision track measurements are required. Only in the HERA II period this resolution can be achieved, provided by the MVD.

The data sample here analysed covers data taken in the 2005, during the HERA II period. It corresponds to an integrated luminosity taken by ZEUS of about $126\,\mathrm{pb}^{-1}$.

4.2 Monte Carlo

In this section, the Monte Carlo samples generated and used for the simulation of the data analysed in this study are presented.

4.2.1 DJANGOH and RAPGAP

The Monte Carlo program used in this analysis to generate the heavy quarks content of the ep-scattering events in the DIS regime is the RAPGAP [82] event generator. It is used to generate either beauty and charm events.
The background, constituted by events from light flavors, is simulated using DJANGOH [73], an interface between HERACLES [74, 75] and ARIADNE [86].

The HERACLES program, used by RAPGAP and DJANGOH, simulates ep-scattering in DIS regime, including first order radiative corrections. The hard scattering between the parton and the photon is simulated according to the Standard Model cross sections and the proton PDFs. The parameterization of the PDF is chosen according to the CTEQ5 [66] set of proton PDFs

RAPGAP is used for QCD corrections in order to simulate the complete ep-scattering process. The first order QCD processes are simulated using exact matrix elements. These processes are the BGF and processes with a radiated gluon (see Ch. 1, Fig. 1.9). For higher order corrections, QCD parton showers, based on the *leading log* DGLAP [15] splitting functions are used. They can occur before and after the hard subprocess.

For the fragmentation, RAPGAP uses the Lund-string model, as it is implemented in JETSET/ Pythia [85] (see Fig. 4.1).

ARIADNE uses the color dipole model (CDM). In this model, gluon emissions from a $q\bar{q}$ pair is treated as radiation from the color dipole between the quark and the anti-quark. This model incorporates BGF as an extra process, while QCDC is included in the color dipole radiation.
Like RAPGAP, also ARIADNE uses the Lund-string model for hadronization.

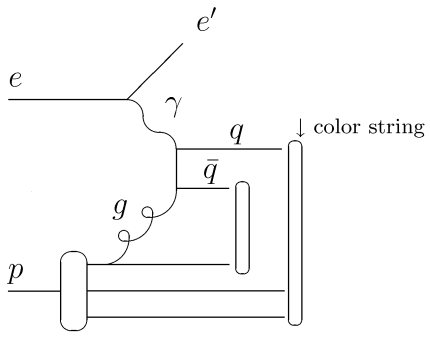

Figure 4.1: RAPGAP implementation of BGF. Shown are the color strings and the proton remnant in Boson-gluon-fusion of $O(a^{em}a_s)$. The proton remnant is the valence quark and valence diquark [82].

The DJANGOH MC generator provides the simulation of the whole inclusive DIS event; that means with beauty and charm components also therein. But, due to a more accurate treatment of the matrix elements in the cross–sections calculations, RAPGAP is expected to be more reliable DJANGOH in reproducing the heavy quarks behaviours. So, to build a proper inclusive sample of DIS events, the heavy quarks component supplied by the DJANGOH MC has been replaced by the events simulated with RAPGAP.
The differences are not relevant for light quarks, that are hence simulated with DJANGOH.

The evaluation of the right amount of heavy quarks from RAPGAP to be added to the light quarks from DJANGOH has been computed according to the values of the cross–sections for the corresponding processes, and then summed to obtain the inclusive MC. The relative percentages are kept so that the total amount of the MC events should correspond to a luminosity proportional to one of the analysed data. It's worth to stress that if the MC cross–sections where correct, the total cross–section of the inclusive MC sample built in such a way would reproduce exactly the real DIS cross–section, without any normalization.
However, the inclusive MC sample arranged in the way just explained is not expected to reproduce the correct number of events measured in the data, since it is well known that the MC cross–sections of the heavy quark production [1] are wrong by some factor[2]. The MC sample is expected to reproduce the shapes of the differential distributions for the main kinematical and topological variables of the data, whereas to reproduce properly the amount of the events too, the normalization is usually taken from the comparison to the data. So in order to check that the main distributions are well reproduced by the inclusive MC, all the distributions are normalized to the data.

An overview of MC used in this analysis is given in Table 4.1; it can be seen that the amount of light quarks has been chosen to be roughly 4.2 times the luminosity of the data. The charm part alone is about the same, whereas the beauty sample is well above.
The different trigger configurations set during the data taking periods are assigned to four configurations of the MC detector simulation. The luminosity of the different MC configurations is generated accordingly to the corresponding data luminosity, and the proportion are kept for each MC.

Process	cross–section	MC generator	Luminosity	Cuts
$ep \to b\bar{b}X$	0.908 nb	RAPGAP	2077.0 pb^{-1}	$Q^2 > 1\,\text{GeV}^2$
$ep \to c\bar{c}X$	21.36 nb	RAPGAP	303.3 pb^{-1}	$Q^2 > 8\,\text{GeV}^2$
$ep \to c\bar{c}X$	11.55 nb	RAPGAP	280.4 pb^{-1}	$Q^2 > 16\,\text{GeV}^2$
inclusive DIS	83.3 nb	ARIADNE	531.8 pb^{-1}	$Q^2 > 20\,\text{GeV}^2$

Table 4.1: *MC samples used in this analysis.*

[1] The inclusive MC cross section are expected to be more accurate, as the HERA I analyses showed.
[2] The beauty cross–section for example is expected to be wrong by a factor about two. At the end of this analysis an evaluation of the errors of the MC cross–sections, both for charm and beauty, will be obtained. directly from the fit output.

4.3 Data selection

4.3.1 Online requirements

The trigger chain used to select DIS events is described in detail in this section. The detector simulation takes into account the simulation of the trigger system, therefore the same trigger preselection is also applied to data and MC samples. The online pre–selection applied to the examined data is represented by the events flagged by the third level slot SPP02, that requires:

- CAL: $30 < E - p_z < 100\,\text{GeV}$.
- Electron energy $E_{el} > 4\,\text{GeV}$
- Box Cut $12 \times 12\ \ cm$
- SLT SPP01

The SLT slot SPP01 requires in turn basically absence of veto signals, correct timing of the event and a minimum energy deposit in the CAL.

The efficiency of this trigger channel has been check with beauty and charm MC. For the latter, in the selected Q^2 range (see 4.4.1), the efficiency is costantly around 90%, and 93% for the former. After the whole kinematic selection, the overall efficiency for this trigger branch is above 99% on both the heavy flavour MC samples. In Fig. 4.2 the ratio between the accepted events over the total after the whole kinematic seletion is shown for beauty and charm as a function of Q^2.

4.3.2 Electron finder

In DIS events the electron is scattered at a sizeable angle in contrast to photoproduction events where the scattered electron escapes undetected inside the beam pipe. Therefore, to select DIS events, events with a reconstructed electron in the final state are kept. An appropriate software package for the electron finding called SINISTRA [103] is used in this thesis to analyse energy deposits in the electromagnetic and hadronic parts of the CAL; it also distinguishes between electromagnetic and hadronic clusters. The algorithm proceeds in two steps: first, it takes as input the energies of the calorimeter cells, and, using a neural network, gives as output the probability for each cluster to be electromagnetic or hadronic. Then, the second part of the algorithm selects the scattered electron from the list of the candidates.
SINISTRA gives as output the lepton candidate having the highest probability to be the scattered electron. For this candidate the probability, $Prob_{el}$, the energy deposited in the calorimeter, E_{el}, and the inelasticity, y_{el}, are given as output by the algorithm.

Filtering the data to be analysed, the following pre-seection has been applied on the electron candidate:

- $Prob_{el} > 0.97$
- $E_{el} > 9\,\text{GeV}$
- $x_{el} > 0.00007$
- $y_{el}^{JB} > 0.01$
- $y_{el}^{EL} < 0.9$

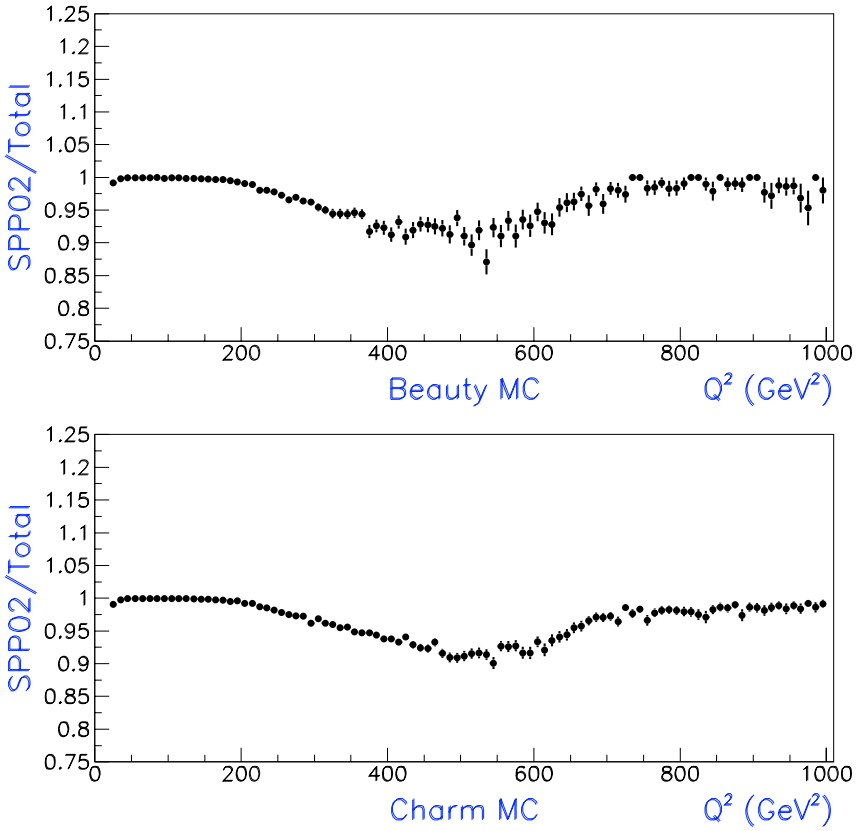

Figure 4.2: *Ratio of the accepted event from SPP02 over the total after the whole kinematic selection for beauty (up) and charm (down) MC.*

4.4 Reconstruction method

In order to obtain the main kinematic variables y and Q^2, different reconstruction methods are possible. Since the detector performs measurements of several observable quantities, that is energies, angles or momenta. Such a redundancy traslates in different ways to derive the kinetic variables. Without too many details, one can essentially make use of the leptonic variables "Electron" method, of the hadronic variables, "Jacquet–Blondet" method, or combinations of them, as for "Σ" and "Double Angle"(DA)" methods (see e.g. [87]). In Figs. 4.3, 4.4 the correlation between the generated and the corresponding reconstructed quantities is shown for the y and Q^2 variables for the Double Angle, with and without CAL energy correction, the Electron and the "eΣ" methods, together with the so–called *bias* for the same variables, that is the difference between the generated and the reconstructed values over the generated ones.

Beside the effective resolution achievable using MC events with the different methods, our choice was driven by the knowedge that the energy scale of the calorimeter is not perfectly set: to get rid of this issue, the Double Angle method has been chosen to reconstruct the y and Q^2 variables in the present analysis. Their definitions are as follows:

$$Q^2_{DA} = \frac{4\, E^2_{el}\, cos^2\frac{\theta_{el}}{2}}{sin^2\frac{\theta_{el}}{2} + sin\frac{\theta_{el}}{2} cos\frac{\theta_{el}}{2} tan\frac{\theta_{el}}{2}} \tag{4.1}$$

$$y_{DA} = 1 - \frac{sin\frac{\theta_{el}}{2}}{sin\frac{\theta_{el}}{2} + cos\frac{\theta_{el}}{2} tan\frac{\theta_{el}}{2}} \tag{4.2}$$

where θ_{el} is the azimuthal angle of the scattered electron and E_{el} its initial energy.

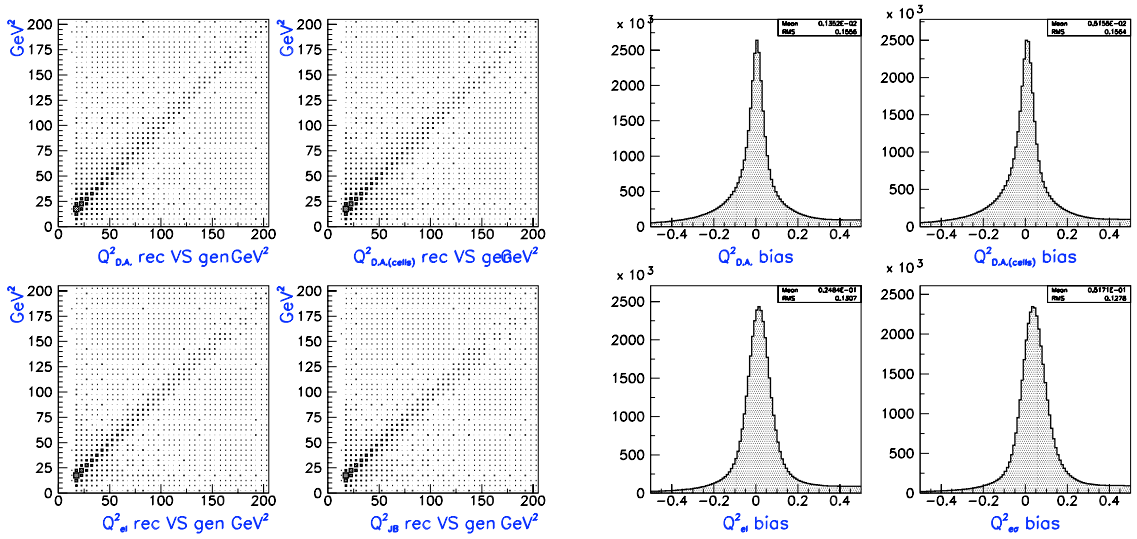

Figure 4.3: *LEFT: correlation between the generated and the reconstructed Q^2 for the methods Double Angle, with and without* CAL *energy correction (up) the electron (down left) and the "eΣ" (down right); RIGHT: bias of the corresponding reconstruction methods.*

4.4.1 DIS selection

Let's now illustrate the offline requirements applied to select DIS events. Most of them are standar cuts, well tested within the Colaboration. Each data and MC event is required to fulfill the following features:

- At least one electron candidate with the aformentioned characteristics;

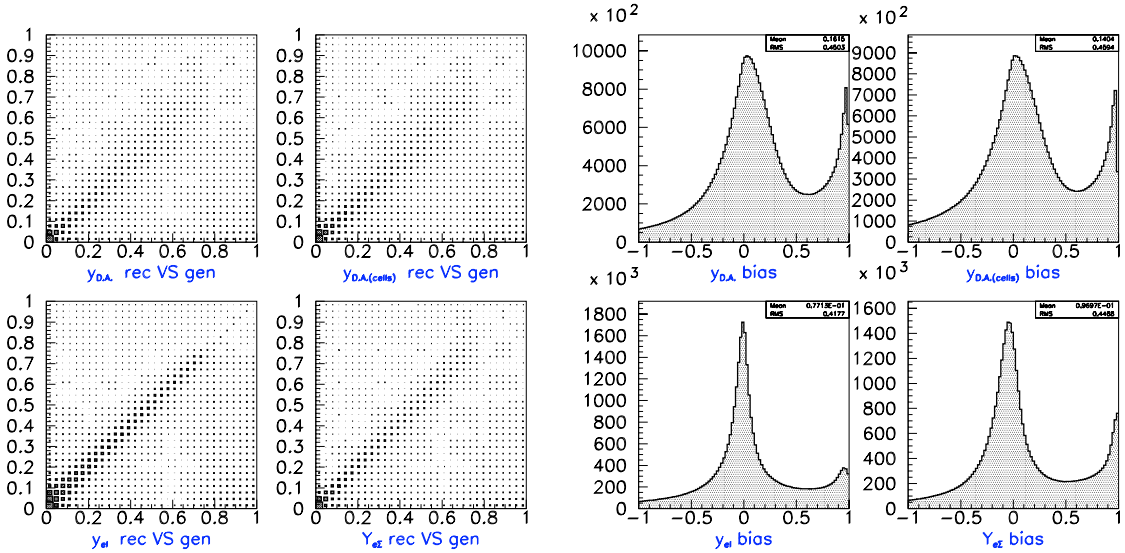

Figure 4.4: *LEFT: correlation between the generated and the reconstructed y for the methods Double Angle, with and without* CAL *energy correction (up) the electron (down left) and the "eΣ" (down right); RIGHT: bias of the corresponding reconstruction methods.*

- $x_{e^-} > 10^{-4}$;
- $22 < Q^2 < 1000$ GeV^2
  the lower cut was dictated by the availability of a suitable inclusive DIS MC sample, the higher one to constrain the background contamination;
- Electron energy in the CAL greater than 10 GeV, to ensure the electron being well identified;
- $y_{JB} > 0.02$ and $y_{el} < 0.7$ [3]
  these limits are set to avoid phase space regions with high systematic errors: due to the hadronix flux and to mis–identified electrons, in the low y region, and photoproduction background not under control, at high y values;
- coordinated of the reconstructed primary vertex within $\pm 30\ cm$ from the nominal interaction point position, to suppress cosmic and background events as collisions with the beam gas;
- Electron x and y position far enough from the beam pipe, to ensure it was well reconstructed:
  $|X_{el}| > 12\ cm$ and $|Y_{el}| > 7\ cm$;
- net longitudinal energy of the event correctly balanced, to suppress photoproduction background:
  $40 < [E - p_z(e^-)]_{Zufo} < 60$ GeV;
- Events accepted by the SPP02 TLT slot.

Beside that, two further requirements are asked for each event:

- at least *two* tracks of "good quality", see below;
- at least *two* jets with transverse energy greater than 4 GeV, one of them with energy greater than 5 GeV.

The former requirement is imposed by the choice of the observables quantities fitted to extract the signal (see Ch. 5), the latter being devoted to limit the contamination of events without heavy flavour production.

The electron is sistematically removed from the sample of tracks clustered in the jets and processed in the analysis.

4.4.2 Track quality requirements

In order to achieve a good resolution on the measured impact parameters, only tracks with the following characteristics are retained:

- at least **three** crossed CTD superlayers: $n_{SL} \geq 3$;
- reference point of helix not out of place: $|Z_H| < 30$ cm;
- at least **four** MVD hits: $n_{MVD\ hits} \geq 4$;
- minimum transverse momentum: $p_T > 500$ MeV;
- small error on the impact parameter[4]: σIP $< 1mm$;

In addiction to the aformentioned cuts, each track is required to fulfill another important request, that is:

- IP smaller than one millimiter: IP$< 1mm$.

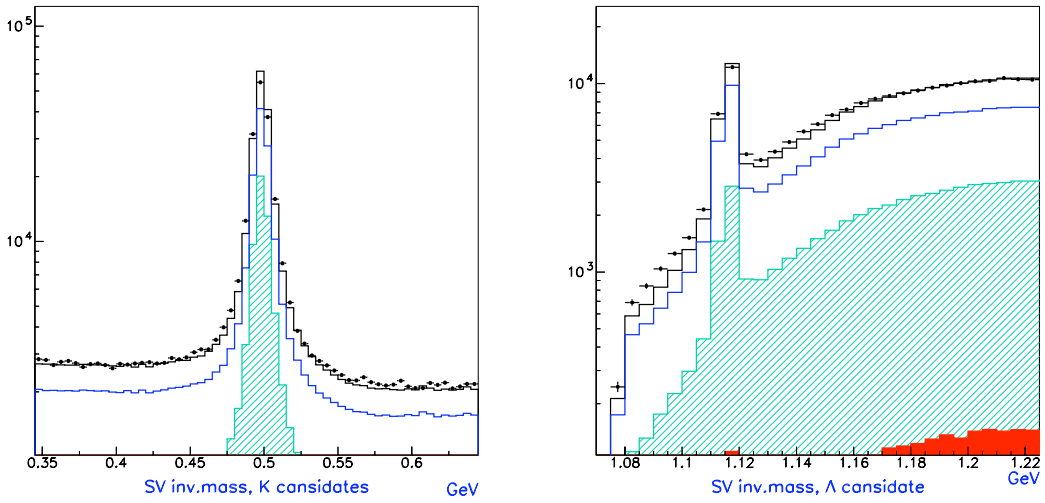

Figure 4.5: *Invariant mass peacks for K^0(left) and Λ (right) candidates. The different flavours components as predicted by the MC are also shown: beauty in full red, charm in hatched green and light quark in blue. The procedure to select the tracks used to compute the invariant mass is explained in the text.*

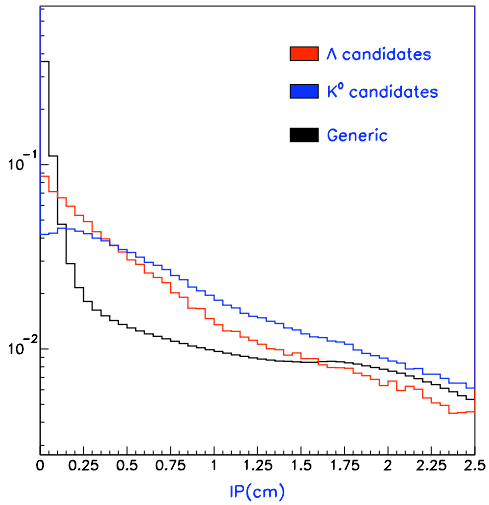

Figure 4.6: *IP absolute values for tracks coming form K^0 and Λ candidates (blue and red histograms respectively) decay compared to the IP of the generic track (black histogram) selected in the same sample.*

Without this cut, the signed impact parameter distributions would be greatly dominated by long lived particles not containing heavy flavours, but giving large positive IP values anyway, such as Kaons or Lambdas; this requirement is hence devote to reject them.

In order to verify that the impact parameters of the tracks coming from the light long living particle decay such as Kaons and Lambdas are effetively large, a cross check has been performed.

[3] In these cases, the JB method has been used to get rid of those background events at low y having large deposit of energy in the FCAL, contaminated by the proton remnant and/or escaping though the beam pipe, whereas the cut at high y_{el} permits to reject fake electron events, peaking at $y \simeq 0$. As metioned before, to scan the y value in various bins, the DA method has been adopted.

[4] the error of the impact parameter receives contributions form the position of the track's DCA and from the beam spot width.

Particles as Kaons or Lambdas are expected to have large lifetime[5], so the secondary vertex of their decay are usually well reconstructed. Furthermore, they are expected to decay meanly through decay modes producing two tracks with opposite charge. Therefore, the invariant mass of the track pairs fitted to a secondary vertex has been computed for those secondary verticies having only two tracks with opposite sign fitted to them. For the Λ candidates the masses of the tracks was assigned setting the proton mass to the one with highest momentum and the pion mass to the other one; for the K^0 candidates, the pion mass was assumed for both the tracks.
The invariant mass distributions built with this criteria show evident peaks in the mass regions of K^0 and Λ, as can be seen in Fig. 4.5.
Then the normalized distribution of the impact parameters of those tracks having an invariant mass within one sigma from the nominal values of the K^0 and Λ masses has been compared with the impact parameters of the generic tracks coming from the secondary verticies selected in the same way. Fig. 4.6 shows clearly that the impact parameters of tracks coming from K^0 and Λ candidates, the blue and red histogram respectively, are much larger than the other ones, represented by the dark histogram.

A small fraction of heavy hadrons could be thrown away with this cut: the B_s mesons for example are expected to live enough to deliver tracks with IP larger than one millimiter indeed. But their production rate is so small in our kinematical regime that their contribution is completly negligible.

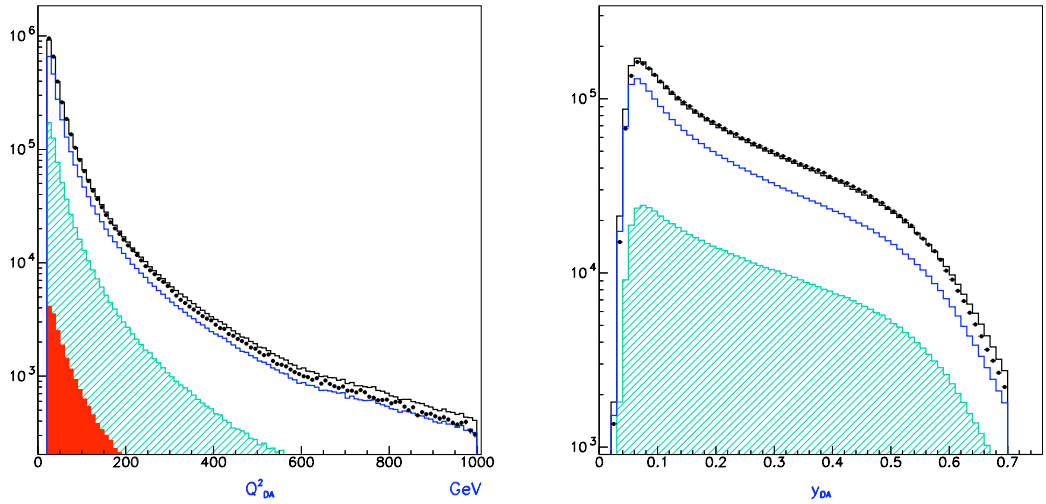

Figure 4.7: *Data and MC distributions for the main kinematic variables: Q^2, on the left, and y, on the right, both reconstructed with the Double Angle method. The different flavours components as predicted by the MC are also shown: beauty in full red, charm in hatched green and light quark in blue.*

4.5 Control distributions

In this section the control distributions concerning the main variables related to this analysis are shown. The inclusive DIS MC, built taking the beauty and charm events from RAPGAP and the light quark contribution from DJANGOH is normalized to the corresponding data distribution and compared with it. The different flavour components are explicitly shown in each histogram: the red filled histograms represent the beauty fraction, the green hatched area is the charm component, the blue histogram is the light quark fraction, black line in the sum of the three, that is the inclusive MC, where the data are represented by black dots.

Fig 4.7 shows the main kinematic variables Q^2 and y, reconstructed with the Double Angle method.
The overall multiplicities of the jets and of the tracks after the quality selection are shown in Fig. 4.8
Other quantity related to the jets are shown in the histograms of Figs. 4.9 and 4.10: transverse momentum and energy,

[5] $c\tau(K^0) \simeq 2.7\ cm,\ \ c\tau(\Lambda^0) \simeq 7.9\ cm.$

polar and azimuthal angle for all the reconstructed jets with transverse energy greater than $4\,\mathrm{GeV}$, and for the most energetic jet respectively.
The quantities involved in the track–jets association procedure are shown in Fig. 4.11: the difference in polar and azimuthal angle between the most energetic jet and the track direction, and the quadratic sum of the two quantities before the association, that is their distance in the $r-\phi$ plane.

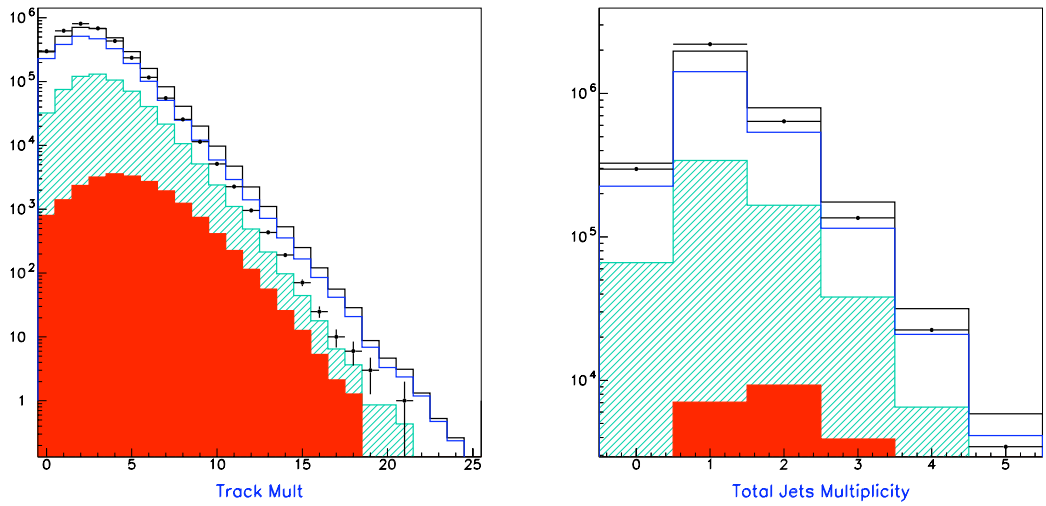

Figure 4.8: *Tracks and jets multiplicity in the examined data and MC samples. The tracks multiplicity reported here is obtained after the quality selection. In full red the beauty component, in hatched green the charm, the blue histograms are light quarks and the black is the total. The data are represented by black dots.*

Turning on quantities more related to the tracking, histograms of Fig. 4.12 represents an overview of the multiplicity of the MVD hits for tracks fulfilling the good quality requirements; the total number of the hits is shown together with the number of the polar and azimuthal hits separately.
In Fig. 4.13 the distributions for the polar and azimuthal angles of the selected tracks are shown, whereas Fig. 4.14 shows their transverse momentum.

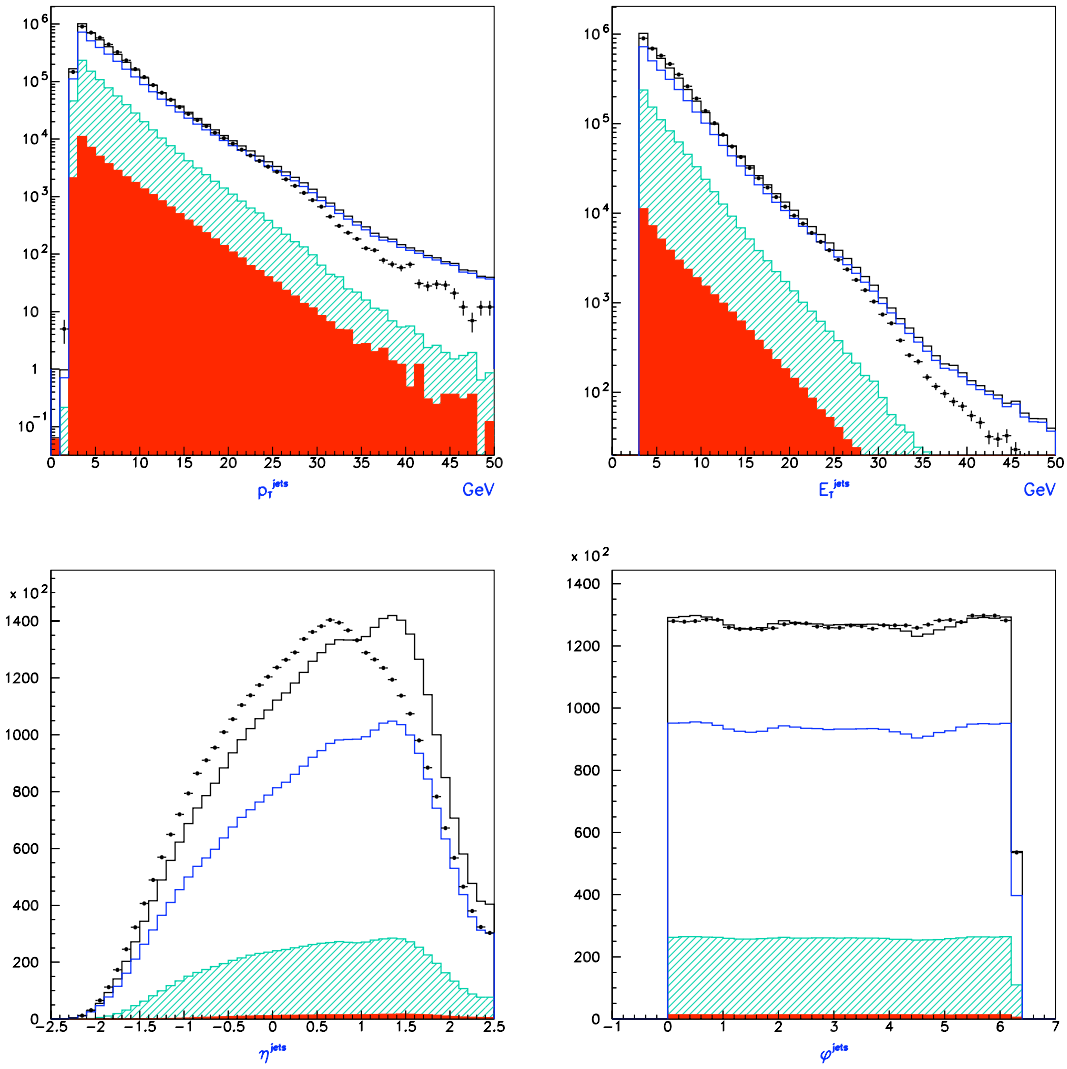

Figure 4.9: *Energetic and angular distributions for the jet with the highest transverse energy: transverse momentum (upper left), transverse energy (upper right), azimuthal (lower left) and polar (lower right) angles. In full red the beauty component, in hatched green the charm, the blue histograms are light quarks and the black is the total. The data are represented by black dots.*

The overall agreement between data and MC is satisfactory. However, sizable discrepancies are present in some ditributions; in particular the Monte Carlo is not precise in predict the shape of the pseudorapidity, either for tracks and for jets; it predicts more events with large track multiplicity and the ϕ distribution of the real tracks is more irregular with respect to the MC predictions.
But above all, the discrepancy more relevant in the present analysis is about the impact parameter distributions, present even despite of the smearing, as it has already been shown in Section 3.3.
The discrepancy observed in the jet distributions are related to the energy scale not perfectly set, whereas the not satisfactoty agreement between data and MC predictions in the tracking related quantities is rooted in a limited comprehension of the MVD performances. They come basically from misalignements of the detector, bad description of the dead material and misunderstanding of multiple scattering effects. This behaviour will limit the quality of our fit and further refinemets are definitely needed on this side.
It is worth to mention that the 2005 data is the subsample of the HERA II data in the worst situation from the point of view of the overall reconstruction quality [111], so there is place for better agreement in analysing the remaining part of the HERA II data.

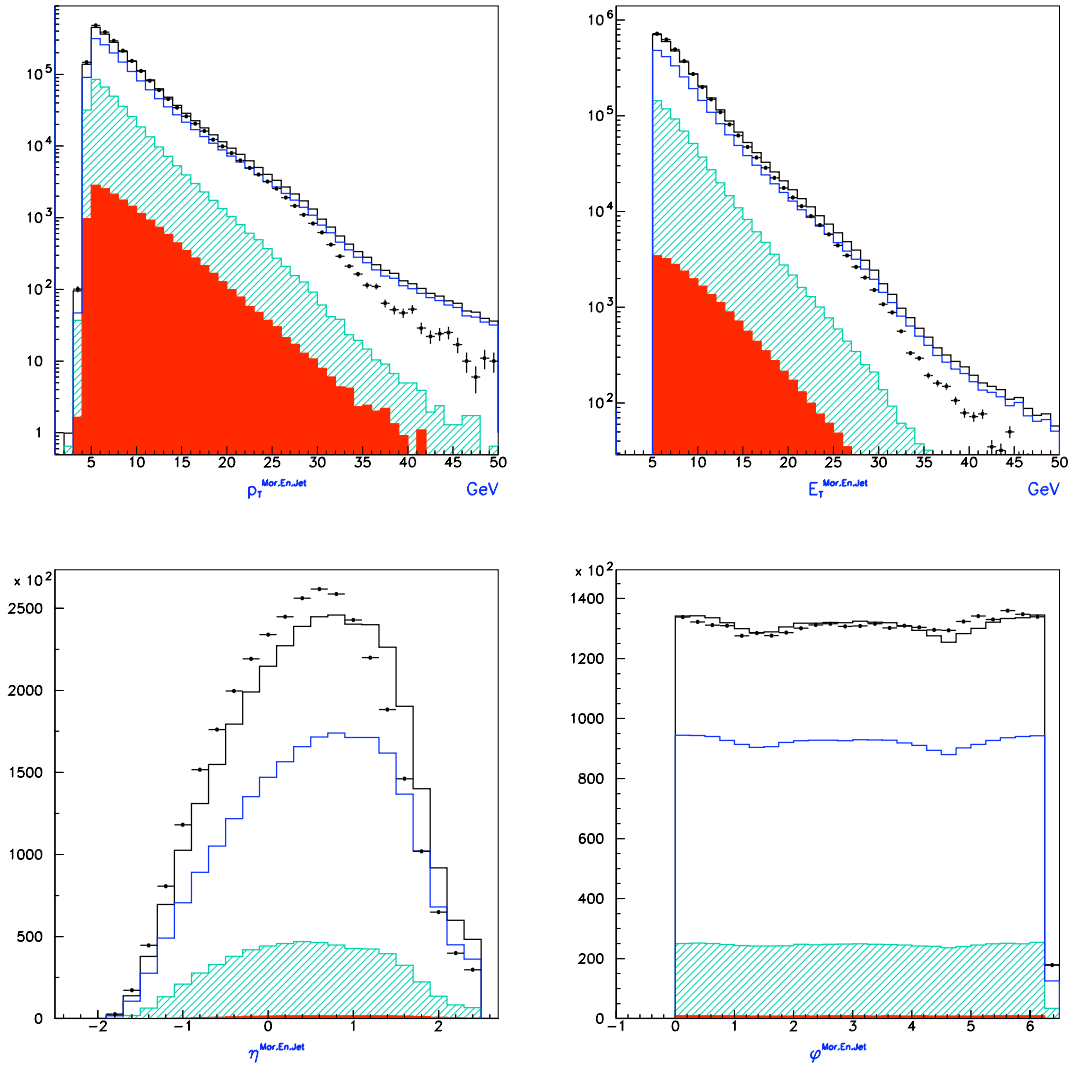

Figure 4.10: *Overall energetic and angular distributions for the jets in the selected data and MC samples: transverse momentum (upper left), transverse energy (upper right), azimuthal (lower left) and polar (lower right) angles. In full red the beauty component, in hatched green the charm, the blue histograms are light quarks and the black is the total. The data are represented by black dots.*

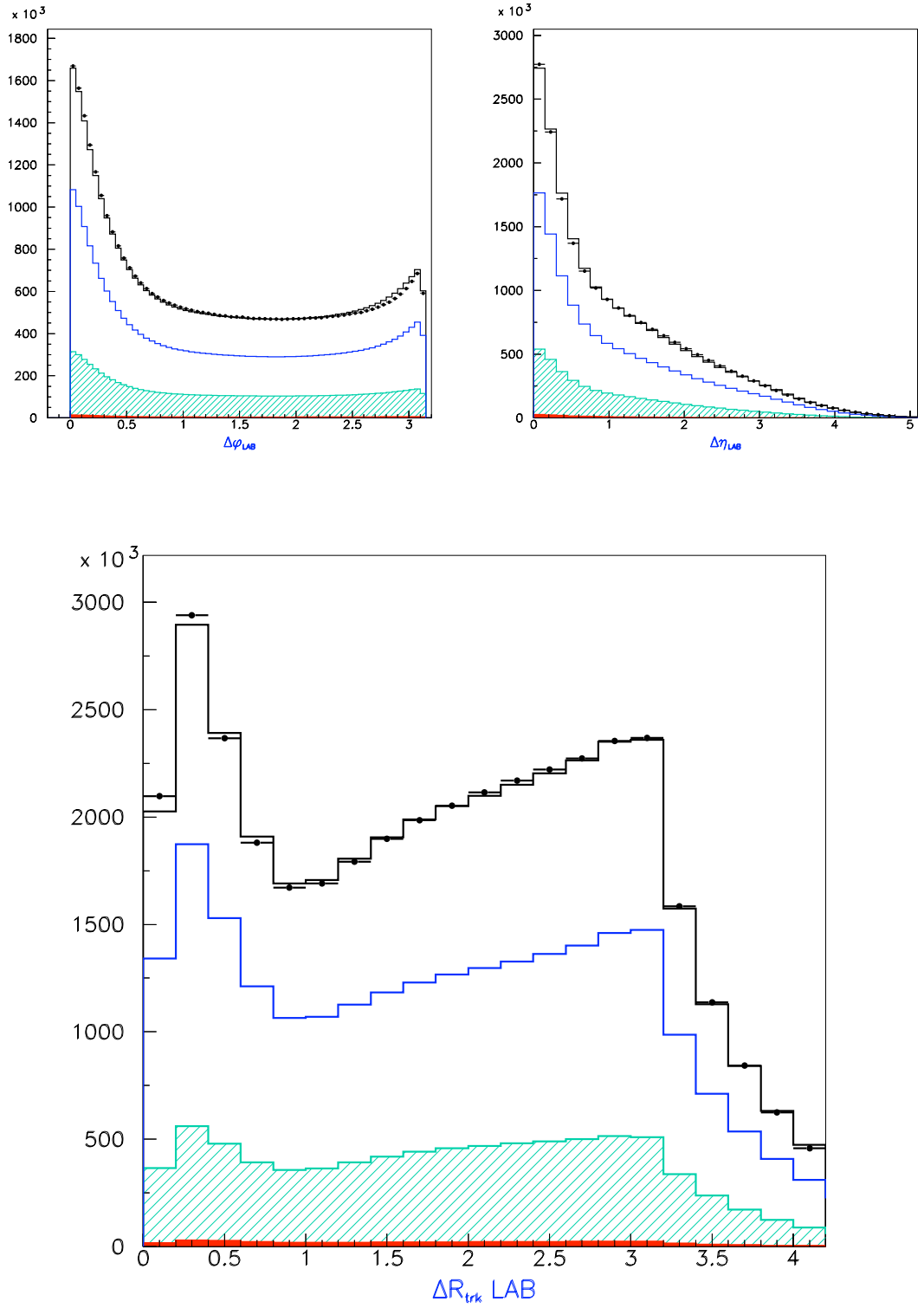

Figure 4.11: *Distributions of the quantities involved in the jet–track association procedure. UPPER PLOTS: Difference in the polar angle, on the left, and azimuthal angles, on the right, between the track and direction of the most energetic; LOWER PLOT: Distance in the $\eta - \phi$ plane between each the track and the direction of the most energetic jet in the event. In full red the beauty component, in hatched green the charm, the blue histograms are light quarks and the black is the total. The data are represented by black dots.*

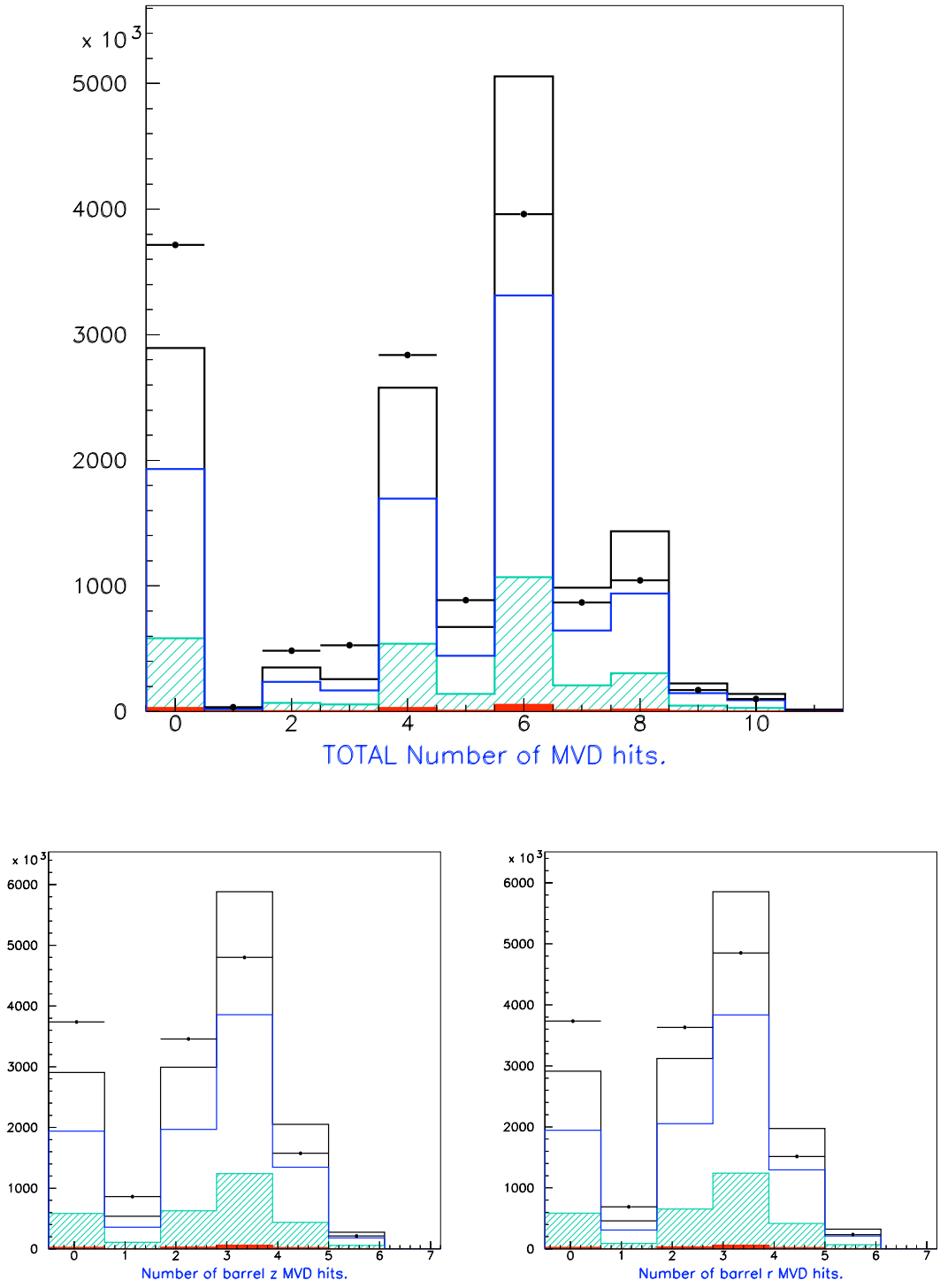

Figure 4.12: *Multiplicity of* MVD *hits for the selected tracks: the total number, upper plot, polar, lower left and azimuthal hits, lower right plot. In full red the beauty component, in hatched green the charm, the blue histograms are light quarks and the black is the total. The data are represented by black dots.*

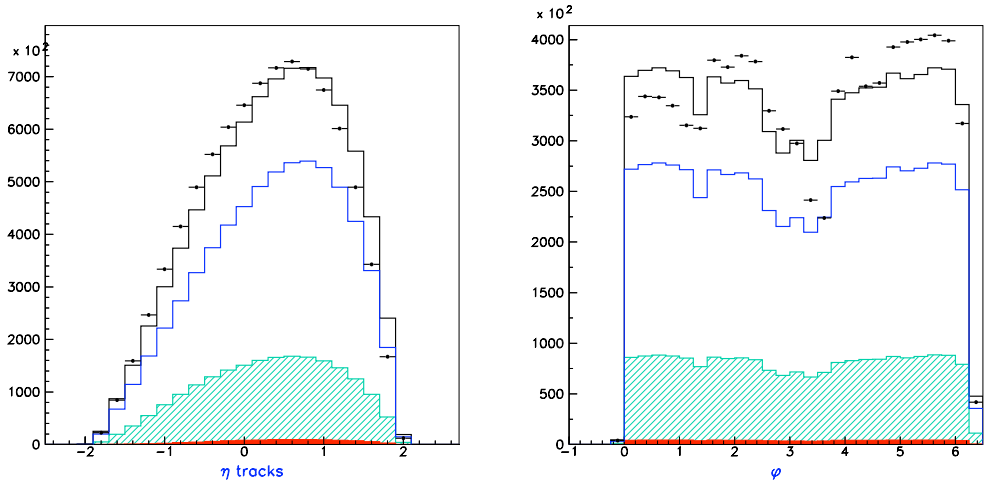

Figure 4.13: *Distributions of the azimuthal (left) and polar angles (right) of the tracks after the good quality selection. In full red the beauty component, in hatched green the charm, the blue histograms are light quarks and the black is the total. The data are trepresented by black dots.*

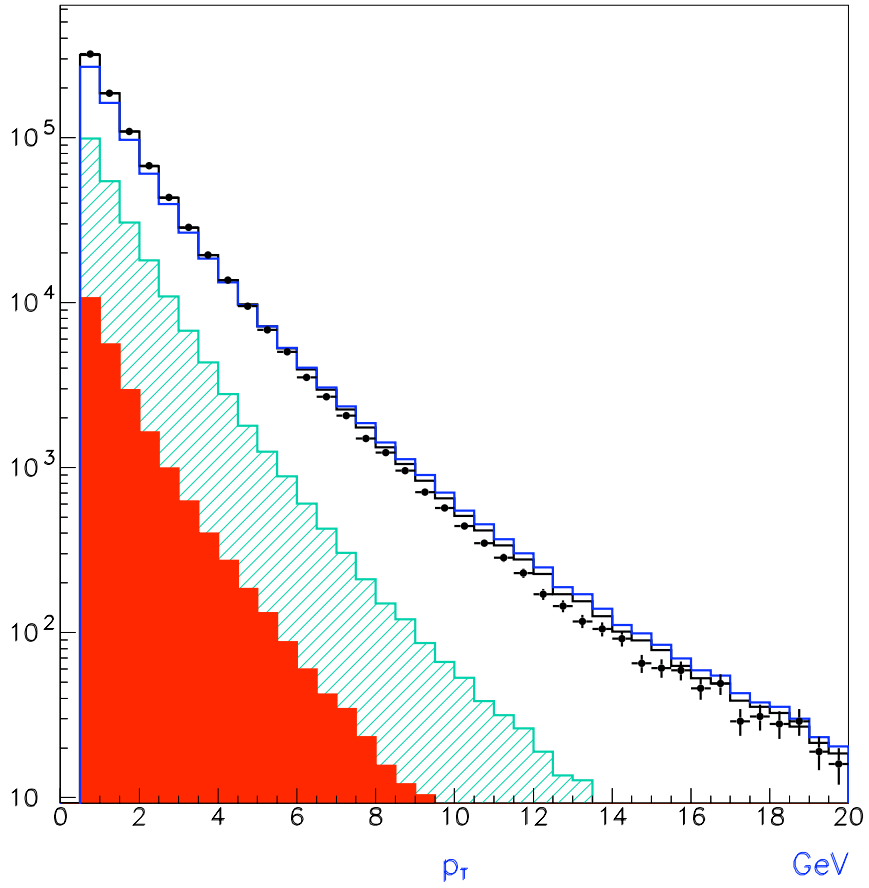

Figure 4.14: *Transverse momentum of the tracks passing the good quality selection.In full red the beauty component, in hatched green the charm, the blue histograms are light quarks and the black is the total. The data are represented by black dots.*

Chapter 5

Fit procedure and results

In this section the tecnique adopted to perform the measurements and the results obtained are presented.
First of all, the distributions of the observables used to extract the physical quantities are presented and motivated. Then the fit method is illustrated in detail together with the manipulations needed in order to derive the physical quantities. The goodness of the fit, the overall result and other technical aspects will be discussed, and finally the values obtained for all the measured quantities will be reported and commented.

5.1 Casting the observables for the fit

As alredy explained in the Section 3.2, the distribution of the signed impact parameter, sIP, is an observable quantity candidate to be sensitive to the flavour contents in each event.

To reduce the light quarks background, represented by events with a impact parameters simmetrically distributed, the negative part of the distributions is mirrored and subtracted from the positive part. With this expedient, only the excess in the positive side of the impact parameters distributions is left; this excess is proportional to the beauty and charm content. Therefore, all the IP distributions entering in the fit will undergo this treatment of mirroring the negative part and subtracting it to the positive side. This procedure appears to be convenient in order to enrich the distributions in signal and to reduce the sensitivity of the fit from the unknown light quark component. But it is very expensive in terms of statistics: after the subtraction the distributions to be fitted have much less events and the errors become bigger, being the statistical error of the subtracted bins added in quadrature. A large amount of the MC sample has been analysed keeping in mind these considerations.

It is worth to highlight that the IP method has never been applied in the ZEUS Collaboration without coupling it with other handles, this method has still to be firmly assessed. The limitated reliability of the detector simulation packages and of the reconstruction tools makes its application challenging, and the present analysis consitutes a pacer for further refinements.

In Section 3.3 it has been pointed out that, even with the implementation of a refined re-weighting procedure, the MC impact parameter poorly reproduces the data. This is one of the reasons why the sIP distribution alone has not enough discriminating power to permit the measurement of the beauty and charm fractions without other informations.

Since the tracks from heavy quarks, once long living light particles are removed, are expected to have the largest impact parameters, in each event the IP of all the tracks are ordered with respect to their absolute values. In such a way one obtains the distribution of the largest impact parameter, the second largest IP and so on. These two distribution, IP_1 and IP_2, are hence expected to have a sensitivity to the heavy quarks content larger than the overall disribution.
In order to get ditributions with a discriminating power even larger, one can distinguish events according to the number of good tracks associated to the most energetic jet. The first IP distribution is then defined collecting the IP when there is just one track associated to the jet, and is simply *the* IP of that track. On the other hand, the second largest IP distribution is built when there is more than one track associated to the jet and is the IP of the second highest IP in absolute value.

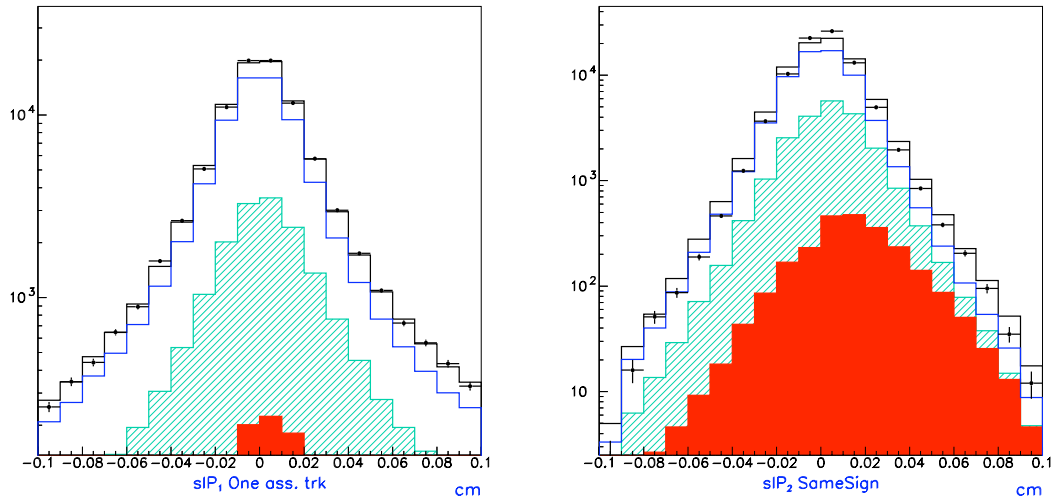

Figure 5.1: *Distribution of the signed IP for the track with the highest (left) and the second highest (right) absolute value of the impact parameter. The data are represented by black dots, whereas the inclusive MC is the dark histogram. The falvour components are also shown separatly: red for beauty, hatched green for charm and blue for light quarks.*

Furthermore, another specification is applied on the second IP distribution, IP_2: only events in which the first and second highest absolute IP have the same sign are selected for the IP_2 distribution. The reasons is that for heavy quarks, at least two tracks are usually produced with high IP, whereas for light quarks the chances for two tracks to deliver large IP values are small. The first and second IP distributions of data and MC are shown in Fig. 5.1, where beauty, charm and light quarks components predicted by the inclusive MC are shown separatly: red for beauty, hatched green for light and blue for light quarks.
The IP_2 distribution is seen to be more rich in signal and have more discriminating power.
IP_1 and IP_2 so defined will be fitted to extract the beauty and charm content. Then, in order to constrain the content of light quarks, the distribution of the IP of all the tracks retained by the global selection, shown in Fig. 5.2, will be fitted together with the IP_1 and IP_2 distributions.
Considerable discrepancies between data and MC are observed in the low values of the IP spectra. The contribution to the overall χ^2 of this region is sizable since the statistical error is smaller than in the other bins, beacuse of the large number of events. Those regions, dominated by the light quark, are featured by an angle α between the directions of the IP and the jet axis close to 90°; Fig. 5.3 shows as for those tracks, the IP distribution has the tail toward higher values larger than the others. The assignement of the sign to the IP is hence strongly subject to finite resolution and misreconstruction effects. Because of this, the first two bins are removed from the distributions of all the IPs. This corresponds to retain tracks with an IP larger than $200\mu m$.

Finally, to further enhance the sensitivity to the heavy quarks signal, a fourth distribution is fitted simultaneously to the three just mentioned. Since the tracks coming from the heavy quarks hadronisation are expected to be quite energetic, the invariant mass of the two tracks with the highest IP is a distribution candidate to carry informations, throughout its shape, about the flavour of the relative tracks This quantity, illustrated in Fig. 5.4 for data and MC is with the same color code as before, has been computed for each event, assuming them to be pions. The width of the bins was set accordingly to the estimated resolution.

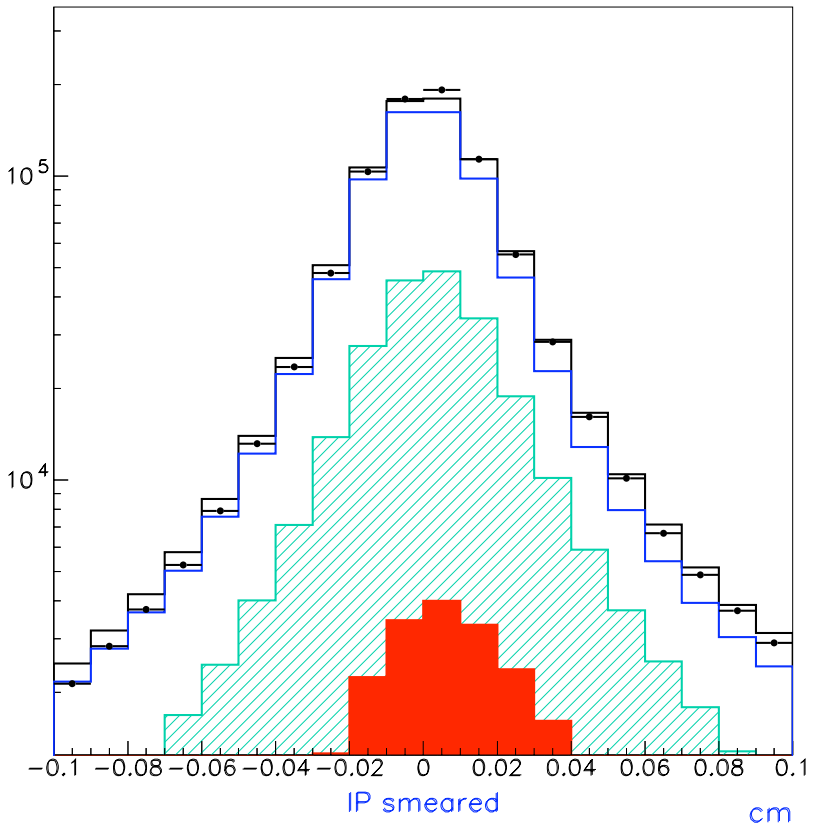

Figure 5.2: *Distribution of the signed IP for all the tracks fulfilling the whole selection. The data are represented by black dots, the inclusive MC is the dark histogram. The falvour components are also shown separatly: red for beauty, hatched green for charm and blue for light quarks.*

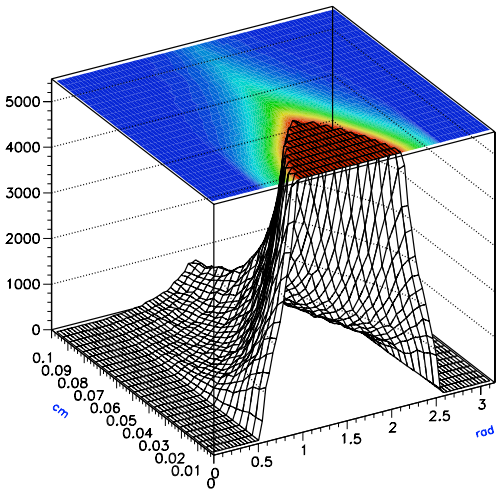

Figure 5.3: *Three dimentional representation of the correlation of the IP absolute value and the angle between the IP direction and the jet axis.*

Summarizing, to extract the heavy quarks content in the selected events, the following distributions are built:

- the highest IP absolute value, when just one track is associated to the more energetic jet: $\mathbf{IP}_1$;
- the second highest IP absolute value, when two or more tracks are associated to the more energetic jet and when IP_1 and IP_2 have same sign: $\mathbf{IP}_2$;
- the IP of all the track passing the selection criteria in all the event: $\mathbf{IP}_{TOT}$;
- the invariant mass of the first and second highest IP absolute value, assuming the pions mass for both the tracks: **M(IP$_1$,IP$_2$)**.

Then, the negative part of the IP distributions are mirrored and subtracted to the positive one; after this step, all the distributions are fitted simultaneously.
Each of the four distributions is obtained in different bins of y and Q^2, set to be equal to the binning chosen to compare directly the pubblished ZEUS results about $F_2^{c\bar{c}}/F_2$ [24].

5.2 Fit procedure

Each of the three components constituting the inclusive Monte Carlo, beauty, charm and light quarks, has been scaled by a factor given by the ratio between the luminosity of the analyzed data sample, $\mathcal{L}_D$, and the MC luminosity $\mathcal{L}_i$, provided by the total number of the processed events N_i divided by the nominal MC cross–section:

$$p_i^0 = \frac{\mathcal{L}_D}{\mathcal{L}_i} = \frac{\sigma_i \mathcal{L}_D}{N_i} \tag{5.1}$$

where the index i marks the flavours component b, c and lq and σ_i is the relative cross–section. Then the inclusive MC is built as the sum of the three components:

$$MC_{INCL} = p_b^0 \cdot MC_{beauty} + p_c^0 \cdot MC_{charm} + p_{lq}^0 \cdot MC_{light} \tag{5.2}$$

If the MC cross–sections (and the detector simulation) were correct, the MC distributions so obtained would have the same number of events of the data distributions.

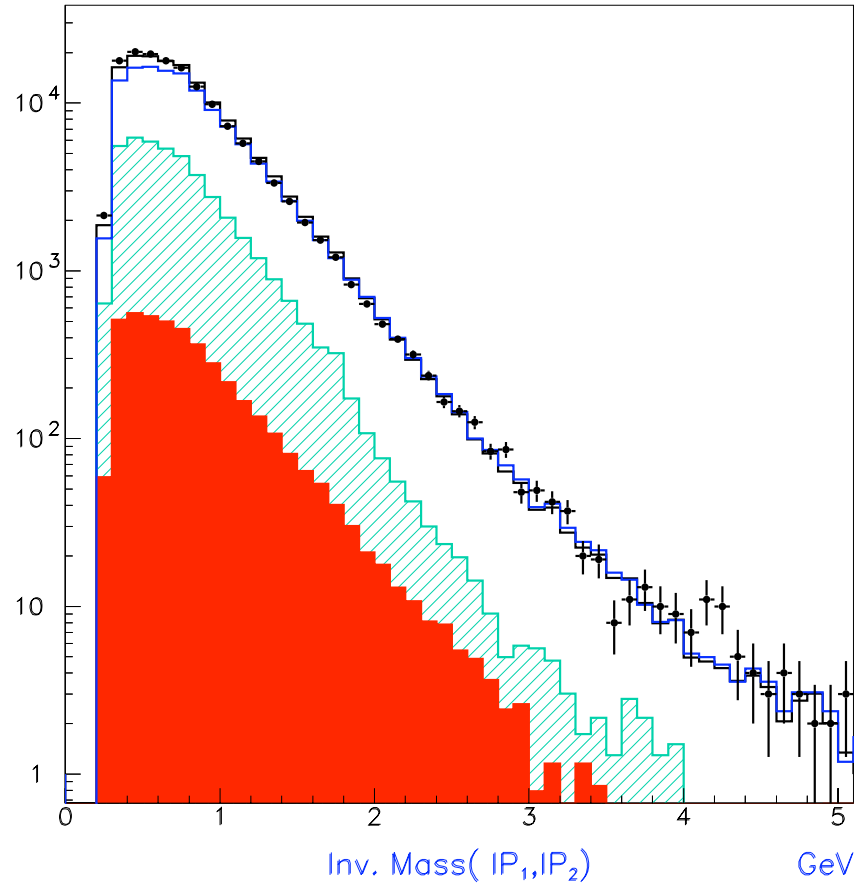

Figure 5.4: *Invariant mass of the two tracks with the highest IP, assuming them to be pions. The data are the black dots, the inclusive MC is the dark histogram, red the beauty component, hatched green the charm and blue the light quarks.*

$p^0_{b,c,lq}$ are the weights from which the fit starts its computation; then the three weights of 5.1 are let free to vary indipendently. For each combinations of the parameters, the total χ^2 is computed as the sum of the χ^2 of the fitted distribution:

$$\chi^2_{Tot} = \chi^2_{IP_1} + \chi^2_{IP_2} + \chi^2_{IP_{TOT}} + \chi^2_{M(IP_1,IP_2)} \tag{5.3}$$

On a single distribution, the χ^2 is computed as:

$$\sum_i \frac{(N_i^{Data} - p_b\, N_i^b - p_c\, N_i^c - p_{lq}\, N_i^{lq})^2}{\sigma^2(N_i^{Data}) + (p_b\, \sigma(N_i^b))^2 + (p_c\, \sigma(p_c\, N_i^c))^2 + (p_{lq}\, \sigma(p_{lq}\, N_i^{lq}))^2} \tag{5.4}$$

where i runs over the bins and N_i is the number of events in that bin. If the entries in a bin are less than 10, the poissonian error is accounted for.

Setting the range of the parameter to probe would require the knowledge of their approximated values, but they are unknown. For this reason the fit is performed iteratively: one starts varying the weight by an amount corresponding to $\pm 100\%$ around the values taken from the nominal value of the MC cross–sections. Once a minimum is found, one performs another fit shrinking the scanned region of the parameter around the previous minimum increasing the resolution, that is decreasing the step made by the single parameters.

It is worth to mention that this procedure appears to be convergent, and after at most three iteration, no significative gain is observed on the minimum χ^2 values.
Nevertheless, these values remains quite high, because of the poor description of the IP distributions of the data by the MC. The goodness of the fit changes a lot depending on the y and Q^2 range: the reduced χ^2, that is the χ^2 divided by the number of degrees of freedom, varies form $79/71$ to $304/71$, and on averages is about two. The higher values are obtained performing the fit on the region at low y and/or high Q^2. At low y values the events are mostly along the beam axis and this could lead to difficulties with the observables chosen to perform the signal extraction. Some examples of the agreement between data and MC with the heavy quarks fractions obtained from the fit are shown in Figs. 5.5-5.8, where the results on the medium y and Q^2 bins are reported: data (black dots) are compared with the inclusive MC (full light blue), with the different flavour components shown separatly: beauty in red, charm in hatched green and light quarks in blue.

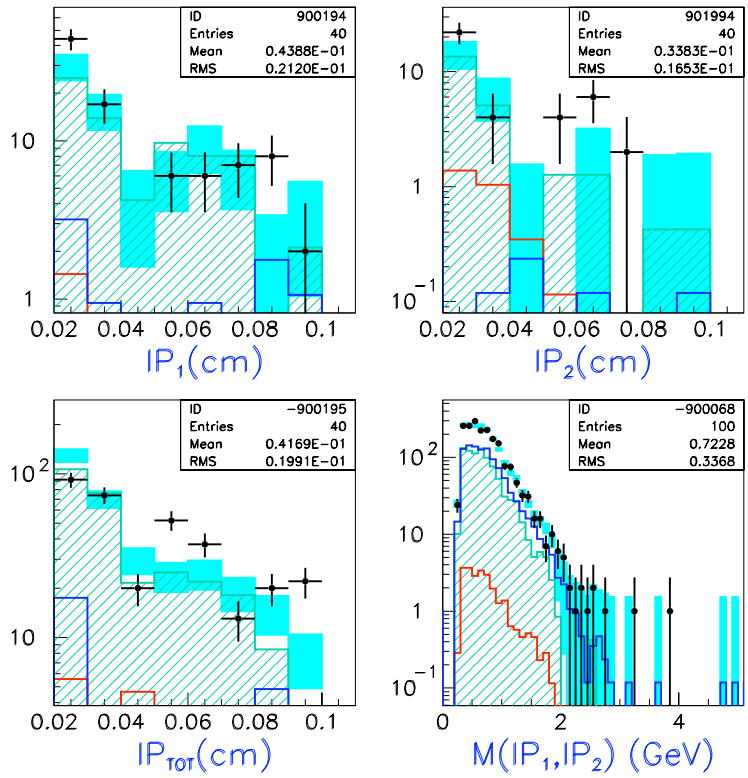

Figure 5.5: *Agreement between data (black dots) and inclusive MC (full light blue) for the fitted distributions* IP_1, IP_2, IP_{TOT} *and* $M(IP_1, IP_2)$ *after the fit's tuning. The amount of the different flavour components, beauty in red, charm in hatched green and light quarks in blue, are the fractions obtained from the fit and providing the minimum of the* χ^2*. The histograms shown here are relative to the bin with* $0.14 < y < 0.28$, $44 < Q^2 < 90\,GeV^2$.

5.3 $F_2^{b\bar{b}}/F_2$ and $F_2^{c\bar{c}}/F_2$ extraction

If the MC admixture obtained mixing the three flavours components with the weights $\hat{p}_{b,c,lq}$ provided by the fit really reproduces the data, for a given histogram one can write:

$$\begin{aligned} \hat{p_b}N_b + \hat{p_c}N_c + \hat{p_{lq}}N_{lq} &= N_D \\ &= \sigma_{DIS}\,\mathcal{L}^D\,\mathcal{A}^{Incl} \\ &= \mathcal{L}^D(\sigma_b\mathcal{A}^b + \sigma_c\mathcal{A}^c + \sigma_{lq}\mathcal{A}^{lq}) \end{aligned} \tag{5.5}$$

where $N_{b,c,lq}$ are the number of the beauty, charm and light quarks MC events of the given histogram and N_D those of the data, $\mathcal{A}^{b,c,lq}$ are the acceptancies for beauty, charm and light quarks MC events and $\mathcal{A}^{Incl}$ the overall acceptance, $\sigma_{b,c,lq}$ are the true production cross–sections for beauty, charm and light quarks and $\mathcal{L}^D$ is the luminosity of the analysed data sample.
For a given Q^2 and y interval, the acceptance $\mathcal{A}$ is defined as the ratio of the events reconstructed in that bin over the generated ones:

$$\mathcal{A} = \frac{N^{rec}}{N^{gen}} \tag{5.6}$$

and it can be computed for each MC flavour as well as for the inclusive MC.
So comparing 5.5 term to term, e.g. for the beauty production cross-section one can derive the expression:

$$\sigma_b = \hat{p_b}\frac{N_b}{\mathcal{L}^D\mathcal{A}_b} \tag{5.7}$$

an analogous expression holds for the charm cross-section.
The number of data and MC events $N_{b,c,lq}$ and N_D must be obtained after the same selection. It appears convenient to choose the DIS selection as the step after which to count the number of events entering in the expression 5.7. After having translate the y bins in the corresponding intervals in x, the differential cross-sections as a function of x and Q^2 in a given interval, $d^2\sigma_b/dxdQ^2$ and $d^2\sigma_c/dxdQ^2$, could be easily derived from 5.7 dividing by the bin widths Δx, ΔQ^2. In the analysed kinematic range one can safely neglet the contribution of the structure functions F_L and xF_3 to the production cross-section. Then, assuming the radiative corrections to be small, the beauty and charm contributions to the structure function F_2 are directly proportional to the beauty and charm production cross-section:

$$F_2^{bb} = k\frac{d^2\sigma_b}{dx\ dQ^2} \tag{5.8}$$

$$F_2^{cc} = k\frac{d^2\sigma_c}{dx\ dQ^2} \tag{5.9}$$

where $k = x\ Q^4/2\pi\alpha^2[1+(1-y)^2]$.

On the other hand, the inclusive cross-section is:

$$\sigma_{DIS} = \frac{N_D}{\mathcal{L}^D \mathcal{A}^{Incl}} \tag{5.10}$$

and, as before:

$$F_2 = k\frac{d^2\sigma_{DIS}}{dx\ dQ^2} \tag{5.11}$$

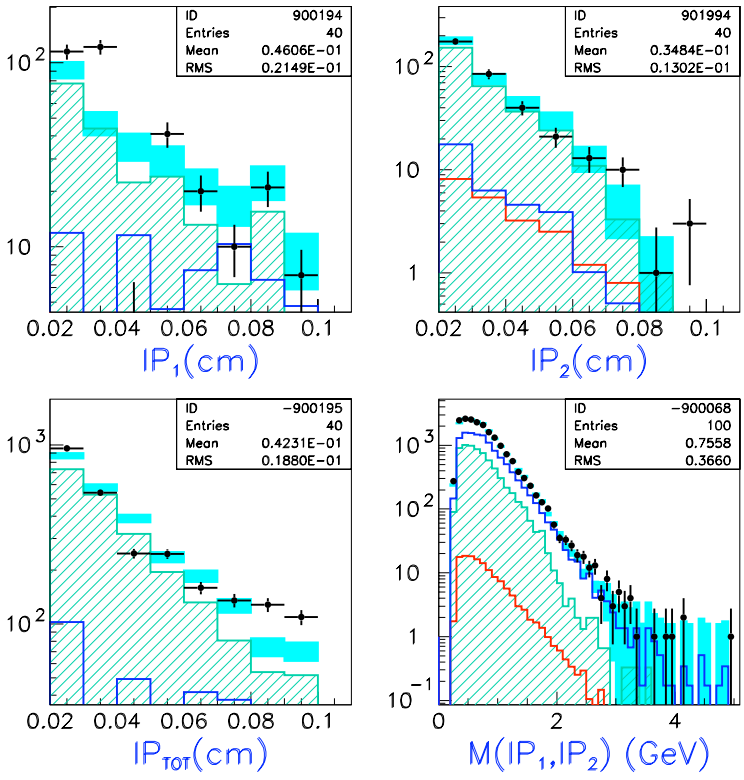

Figure 5.6: *Agreement between data (black dots) and inclusive MC (full light blue) for the fitted distributions IP_1, IP_2, IP_{TOT} and $M(IP_1, IP_2)$ after the fit's tuning. The amount of the different flavour components, beauty in red, charm in hatched green and light quarks in blue, are the fractions obtained from the fit and providing the minimum of the χ^2. The histograms shown here are relative to the bin with $0.14 < y < 0.28$, $90 < Q^2 < 200\,GeV^2$.*

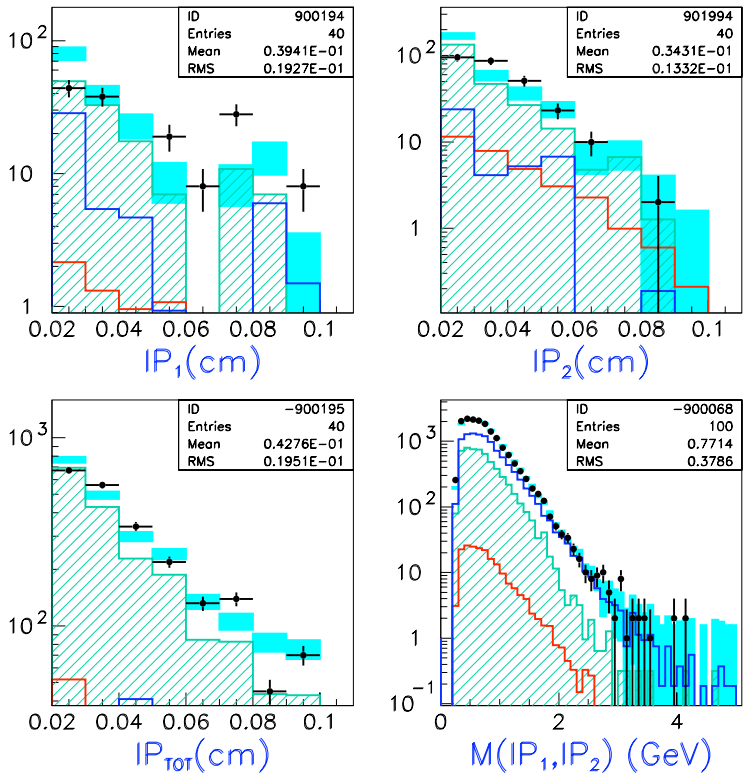

Figure 5.7: *Agreement between data (black dots) and inclusive MC (full light blue) for the fitted distributions* IP_1, IP_2, IP_{TOT} *and* $M(IP_1, IP_2)$ *after the fit's tuning. The amount of the different flavour components, beauty in red, charm in hatched green and light quarks in blue, are the fractions obtained from the fit and providing the minimum of the* χ^2*. The histograms shown here are relative to the bin with* $0.28 < y < 0.7$, $44 < Q^2 < 90\,GeV^2$.

Then, after some simple algebra one gets: one gets:

$$\begin{aligned} \frac{F_2^{bb}}{F_2} &= \hat{p_b}\frac{N_b}{N_D}\frac{\mathcal{A}^{Incl}}{\mathcal{A}^b} \\ \frac{F_2^{cc}}{F_2} &= \hat{p_b}\frac{N_c}{N_D}\frac{\mathcal{A}^{Incl}}{\mathcal{A}^c} \end{aligned} \tag{5.12}$$

These are the expressions used to derive the charm and beauty contributions to the structure function F_2.

The numerical values obtained in each y and Q^2 interval are reported in Tab. 5.1; the errors reported is the quadratic sum of the statistical errors on number of data and MC events N_b or N_c and N_D, and the error on the MC parameters, $\hat{p_b}$ or $\hat{p_c}$, coming from the fit. These ones are evaluated quoting the minimum and maximun values of the measured ratios F_2^{cc}/F_2 testing all the parameters provinding a total χ^2 between the χ^2_{min} and $\chi^2_{min} + 1$; the same has been done for F_2^{bb}/F_2. The acceptance correction appearing in 5.12 can be found in Tab. 5.2.

The measuremets of F_2^{cc}/F_2 obtained in this analysis have been compared with the published results from ZEUS [24] obtained with the D^* mesons; the comparison is shown in Fig. 5.9.
The firts observation to be made is that our points are extremely more precise with respect to the published ZEUS results. This reflects the larger data sample analysed, but expecially the much higher efficiency of our essentially inclusive measurement. Furthermore, the present measurement is not plagued by any extrapolation procedure. On the other hand, we quoted only the error coming from the fit procedure plus the statistical one, (see Sec. 5.5 for a brief discussion about the systematic errors). Keeping in mind what was said and that the determinantions coming from the

D^* analysis are affected by a statistical error obviously larger and a systematic error coming from the extrapolation to the full D^* phase space, the agreement between the two analysis is good.
The values found at high x for $22 < Q^2 < 44\,\mathrm{GeV}^2$ appear quite shifted with respect to the expectation; some effects not yet understood could be present; but it is worth to highlight that the behaviour of the fit in the low y bins is slightly unstable, due to small statistics and peculiar event topology.
In the high Q^2 bins the results found by this analysis are well below the values extracted with the D^*; but those measurements are affetced by large statistical errors and, as can be seen in [24], they are quite above the NLO predictions.

The mesaured values of F_2^{bb}/F_2 in the different y and Q^2 bins are report in Fig. 5.10. The error bars, representing the error coming from the fit procedure added in quadrature to the statistical error on the number of data and MC events, are bigger than in the case of the F_2^{cc}/F_2. The fitted distributions are largely dominated by the charm contribution, and the beauty fractions are seen to be small; therefore the fit is not so sensitive to the shape of the beauty IP distributions. Nevertheless the measurements are upstanding and the prcedure seems able to provide results comparable with other achievements.

5.4 Other informations from the fit

Once the three parameters $\hat{p_b}$, $\hat{p_c}$ and $\hat{p_{lq}}$ have been obtained from the fit, is straightforward to derive the percentages of events coming from beauty and charm in each bin. They are reported in Tab. 5.3.

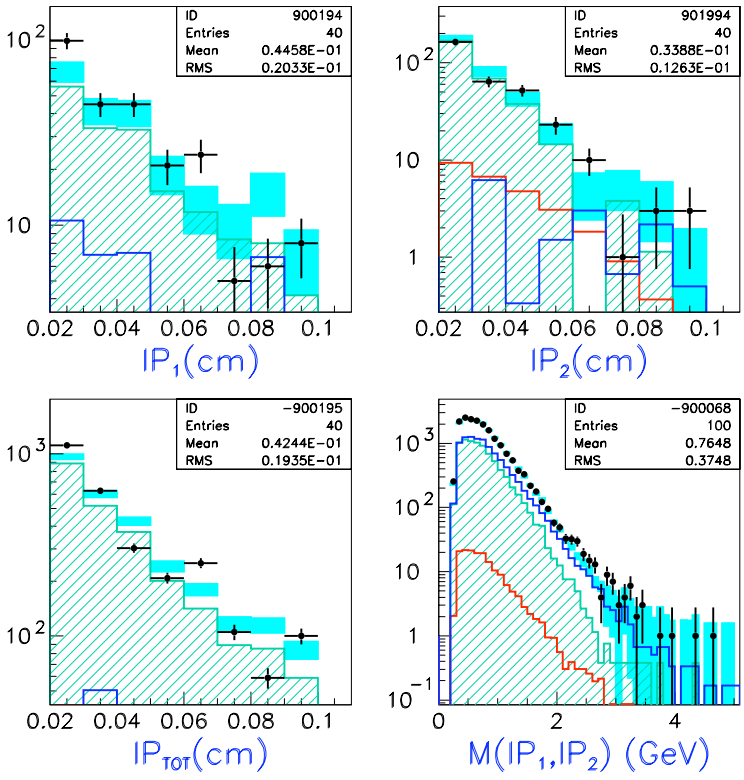

Figure 5.8: *Agreement between data (black dots) and inclusive MC (full light blue) for the fitted distributions IP_1, IP_2, IP_{TOT} and $M(IP_1, IP_2)$ after the fit's tuning. The amount of the different flavour components, beauty in red, charm in hatched green and light quarks in blue, are the fractions obtained from the fit and providing the minimum of the χ^2. The histograms shown here are relative to the bin with $0.28 < y < 0.7$, $90 < Q^2 < 200\,GeV^2$.*

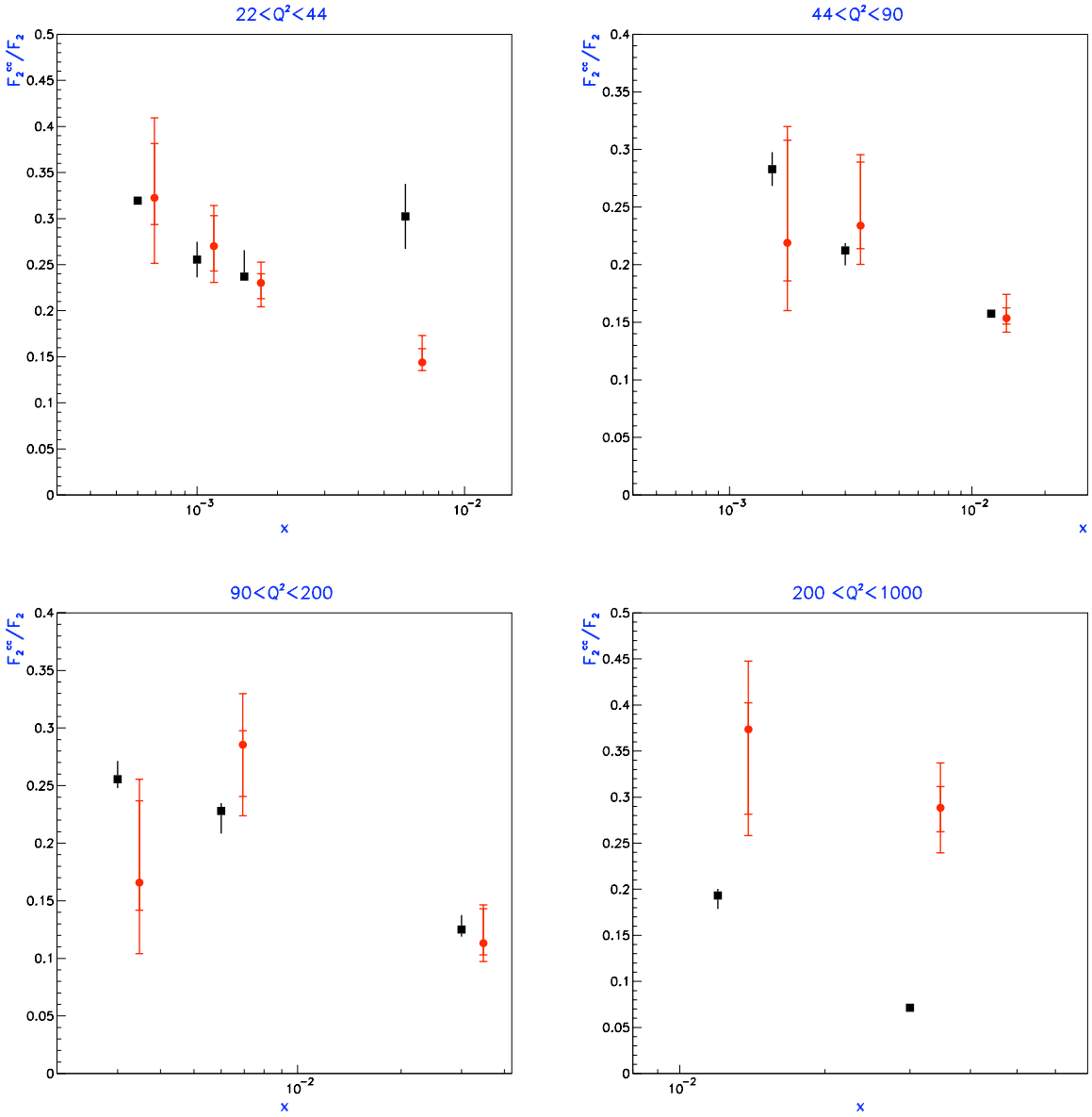

Figure 5.9: *Comparisons of the measured F_2^{cc}/F_2 values a function of x (black squares) with the analogue results obtained by the* ZEUS *Collaboration with the D^* mesons (red dots). The central Q^2 values of the bins are reported on the top of each plot. The statistical error and error from the fit procedure are taken into account for the ratios extracted in this analysis, whereas for the D^* mesons result the systemacic errors (outer bars) are added to the statistical ones (inner bars).*

Depending on x and Q^2 of the analysed bin, the percentage of events with beauty production varies from below one per mille to 1.7%, whereas charm production occurs from 16 to 42% of the cases. The overall percentages of heavy quarks component in the whole kinematic range exploited, that is $0.02 < y < 0.7,\ 22 < Q^2 < 1000\,\mathrm{GeV}^2$, are: $1.6^{+0.3}_{-0.6}\%$ for beauty, $32.23^{+0.02}_{-0.01}\%$ for charm. Considering the differencies in the analysed phase space, these values are comparable with what found by the H1 Collaboration in [24].

The nominal values of the heavy quarks cross–sections, reported in Tab. 4.1, enter in the determination of the bare parameters $p^0_{b,c,lq}$ from which the tuning procedure of the fit starts. So, the fit procedure can be thought as a variation on the heavy quarks cross-sections, and as a direct search for the their true value. The ratio between the MC weights providing the minimum of the χ^2 and their initial values $p^0_{b,c}$ constitutes an indication of how much the values of the

heavy quarks MC cross–sections are wrong. The fit output indicates that the beauty MC underestimates the production cross–section by a factor of about two. This appears to be consistent with other findings (see e.g. [113]).

5.5 Sources of systematic errors

The quantities extracted in this analysis and the method just illustrated appear to be scarcely affected by systematic errors, since most of them cancel in the ratio. In particular, all the contributions related to the requirements of the DIS selection are expected to be totally equivalent in the numerator and the denominator of 5.12, and hence vanishing.
Nevertheless, sources of systematic errors potentially large are anyway present in our measurement. In particular, the relevance of the performances of the MVD in the extraction of the physical quantities induces to consider them as the largest sources of systematic errors.
In the following we are going to briefly discuss the aspects of the present analysis believed to be affected by systematic uncertainties. Further elaborations of this study will have to investigate quantitatively all these aspects:

- the impact parameter resolution. This is expected to be the major source of systematic errors since the fit sensitivity strongly depends on it;

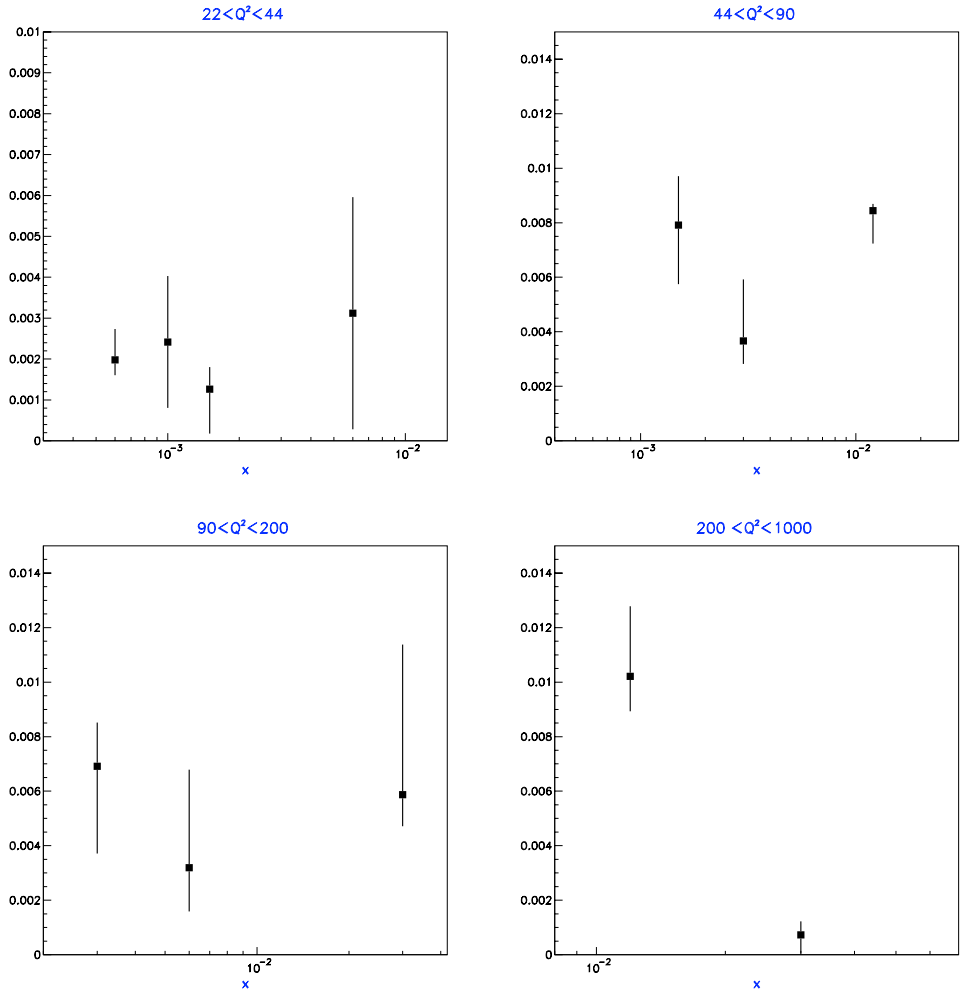

Figure 5.10: *Measured values of the ratio F_2^{bb}/F_2 as a function of x. The central Q^2 values of the bins are reported on the top of each plot. the error bars represent the error coming form the fit procedure added in quadrature with the statistical error on the number of data and MC events.*

- parameters of the smearing procedure; their variations are obviously related to the fit performances;
- the request IP$> 1mm$, to reject long living light particles. Since this cut sets the length of the tails in the fitted distributions, variations could produce sizable changing in the results;
- removal of the first two bins from the mirrored sIP distributions. This is a critical aspect of the analysis, and dedicated studies would be needed. The central part of the signed IP distribution is a region affected by large uncertainties, either from the experimental (larger sensitivity to the IP resolution in the assignment of the sign to the IP) and theoretical side (large contribution of light quarks, hard to model in the MC simulation);
- jet–related quantities:
  1. dependence on the jet finding settings and on the jet axis determination;
  2. jet energy scale and cut on the minimum E_T;
  3. jet–track association procedure: minimum distance in the $\eta - \phi$ plane to which the association is set. Furthermore, the jet–track association could be performed on each jet and not only with the most energetic one

Q^2 bin (GeV^2)	y bin	$F_2^{b\bar{b}}/F_2$	Δ_{stat}	$F_2^{c\bar{c}}/F_2$	Δ_{stat}
22, 44	0.70, 0.35	0.0020	$^{+0.0004}_{-0.0007}$	0.320	$^{+0.007}_{-0.008}$
	0.35, 0.22	0.0024	$^{+0.0016}_{-0.0016}$	0.256	$^{+0.019}_{-0.019}$
	0.22, 0.08	0.0013	$^{+0.0011}_{-0.0005}$	0.237	$^{+0.0004}_{-0.029}$
	0.08, 0.02	0.0038	$^{+0.028}_{-0.0028}$	0.372	$^{+0.035}_{-0.035}$
44, 90	0.70, 0.28	0.0079	$^{+0.0021}_{-0.0018}$	0.283	$^{+0.015}_{-0.015}$
	0.28, 0.14	0.0037	$^{+0.0008}_{-0.0023}$	0.212	$^{+0.013}_{-0.006}$
	0.14, 0.02	0.0089	$^{+0.0012}_{-0.0002}$	0.166	$^{+0.004}_{-0.0004}$
90, 200	0.70, 0.28	0.0069	$^{+0.0032}_{-0.0016}$	0.256	$^{+0.008}_{-0.016}$
	0.28, 0.14	0.0032	$^{+0.0016}_{-0.0036}$	0.229	$^{+0.020}_{-0.007}$
	0.14, 0.02	0.0061	$^{+0.0011}_{-0.0055}$	0.130	$^{+0.006}_{-0.013}$
200, 1000	0.70, 0.23	0.0103	$^{+0.0013}_{-0.0026}$	0.194	$^{+0.015}_{-0.007}$
	0.23, 0.02	0.0007	$^{+0.0007}_{-0.0005}$	0.0727	$^{+0.0004}_{-0.0004}$

Table 5.1: *Extracted values of structure functions ratios $F_2^{b\bar{b}}/F_2$ and $F_2^{c\bar{c}}/F_2$ for the corresponding intervals in y and Q^2. The error on the determinations reported is the sum of the error coming from the fit procedure added in quadrature with the statistical error on the number of data and MC events.*

Q^2_{centr}	x_{centr}	$\mathcal{A}^{Beauty}$	$\mathcal{A}^{Charm}$	$\mathcal{A}^{Incl}$
30	0.00060	0.999	0.995	0.843
	0.00100	1.289	1.250	1.065
	0.00150	1.411	1.336	1.159
	0.00600	1.359	1.519	1.597
60	0.00150	1.128	1.128	0.975
	0.00300	1.313	1.284	1.127
	0.01200	1.402	1.490	1.538
130	0.00300	1.120	1.111	0.962
	0.00600	1.318	1.320	1.157
	0.03000	1.378	1.477	1.559
500	0.01200	1.182	1.168	1.015
	0.03000	1.399	1.455	1.416

Table 5.2: *Values of the acceptancies for the different MC species, obtained as the ration of the number of reconstructed events over the generated ones in a given intervals of y and Q^2. The corresponding central values of y and Q^2 are also reported.*

Q^2_{centr}	x_{centr}	Beauty (%)	Charm (%)
30	0.00060	$0.25^{+0.10}_{-0.05}$	$42.0^{+0.2}_{-0.4}$
	0.00100	$0.3^{+0.2}_{-0.2}$	$33.1^{+2.5}_{-2.4}$
	0.00150	$0.17^{+0.07}_{-0.15}$	$31.29^{+3.00}_{-0.02}$
	0.00600	$0.3^{+0.2}_{-0.2}$	$36.7^{+4.0}_{-4.0}$
60	0.00150	$1.1^{+0.2}_{-0.3}$	$39.0^{+1.7}_{-2.2}$
	0.00300	$0.5^{+.03}_{-0.1}$	$30.2^{+1.1}_{-2.0}$
	0.01200	$0.84^{+0.8}_{-1.1}$	$18.7^{+0.2}_{-1.9}$
130	0.00300	$1.0^{+0.2}_{-0.5}$	$38.4^{+2.6}_{-1.3}$
	0.00600	$0.5^{+0.6}_{-0.2}$	$36.3^{+1.2}_{-3.2}$
	0.03000	$0.7^{+0.8}_{-0.1}$	$15.7^{+1.9}_{-0.9}$
500	0.01200	$1.7^{+0.4}_{-0.2}$	$31.1^{+1.3}_{-2.6}$
	0.03000	$0.08^{+0.06}_{-0.07}$	$8.65^{+0.01}_{-0.01}$

Table 5.3: *Percentages of beauty and charm quarks, as predicted by the MC admixture providing the best fit in the different x and Q^2 bins. The bin centering procedure is as in [24].*

Chapter 6

Conclusions and outlook

In this analysis, the measurement of the structure functions ratios $F_2^{c\bar{c}}$ and $F_2^{b\bar{b}}$ over F_2 has been carried out, differentially in x and Q^2, in the kinematic range $22 < Q^2 < 1000$ GeV^2, $0.02 < y < 0.7$. The analysis has been performed on the data sample collected by the ZEUS experiment during the year 2005 and corresponds to about 130 pb^{-1}.

The result has been achieved fitting simultaneously four distributions, all related to the geometrical properties of the tracks coming from the heavy quark decay. Taking advantage of the correlation between the heavy hadrons lifetime and the impact parameter of the track of their decay products, it has been possible to build distributions greatly enriched in signal, over which a simultaneous χ^2 fit has been performed. The extracted values of $F_2^{c\bar{c}}/F_2$ have been compared with the result obtained by ZEUS from the D^* meson analysis and found to be well compatible.

Since the MC distribution of the impact parameter badly reproduces the data, the MC sample used in the analysis underwent a refined reweighting procedure. In spite of that, and even if the regions of the impact parameter distributions where a large discrepancy between data and MC was present have been identified and discarded from the analysis, the goodness of fit remains not satisfactory, and further improvements appear needed on this side.
This aspect, together with the sources of systematic errors, has to be elaborated further before this result can be finalized.

The technique adopted, exploited in the ZEUS Collaboration for the first time in the contest of an almost inclusive analysis, appears to be very promising, showing that the achieved results are superior to what obtained with althernative strategies. The impact parameter method fully exploits the tracking performances of the ZEUS Micro Vertex Detector and shows all its potential, paving the way for further achievements.

Once performed on the whole HERA II data sample and with the MVD systematics fully understood, this analysis is candidate to become the best way to obtain precise measurements on the structure functions F_2^{bb} and F_2^{cc}, fundamental quantities for future experiments as the LHC.

Bibliography

[1] D.J.Griffiths, *Introduction to elementary particles*, John Wiley & Sons, (1987)

[2] F.Halzen, A.D.Martin,*Quarks and Leptons: An Introduction Course in Modern Particle Physics*, John Wiley & Sons, (1984)

[3] W.-M. Yao et al., Journal of Physics, G **33**, 1 (2006)

[4] S.Chekanov *et al*., ZEUS Collab., *Evidence for a narrow baryonic state decaying to K0(S) p and K0(S) anti-p in deep inelastic scattering at HERA*., Phys. Lett. B**591**, 7-22 (2004)

[5] M.Born, Optik, Springer, Berlin (1933)

[6] A.Gabareen Mokhtar, H1 Collab., *Recent electroweak measurements from the H1 and ZEUS experiments*, arXiv:hep-ex/0406036

[7] M.Gell.Mann, *A Schematic Model Of Baryons And Mesons*, Phys. Lett. **8**, 214 (1964); G.Zweig, CERN-8192/TH 401 (1964); G.Zweig, CERN-8419/TH 402 (1964)

[8] R.P.Feynman, *Very High-Energy Collisions Of Hadrons*, Phys. Rev. Lett. **23**, 1415 (1969)

[9] J.D.Bjorke, *Asymptotic Sum Rules At Infinite Momentum*, Phys. Rev. **179**, 1547 (1969)

[10] C.G.Callan, D.J.Gross, *High-Energy Electroproduction And The Constitution Of The Electric Current*, Phys. Rev. Lett. **22**, 156 (1969)

[11] Bloom *et al*., *High-Energy Inelastic E P Scattering At 6-Degrees And 10-Degrees*, Phys. Rev. Lett. **23**, 930 (1969)

[12] C.Glasman, *Jet production in deep inelastic e p scattering at HERA*, arXiv:hep-ex/0312011

[13] ZEUS Structure Functions and Electroweak Physics working group, Combined H1 and ZEUS proton PDFs (unpublished), 2004, available on `http://www-zeus.desy.de/physics/sfew/PUBLIC/sfew_results/preliminary/moriond04/zeush1.php`

[14] G.Altarelli, G.Parisi, *Asymptotic Freedom In Parton Language*, Nucl. Phys. B**126**, 298 (1977)

[15] G.Altarelli, G.Parisi, *Asymptotic Freedom In Parton Language*, Nucl. Phys. B**126**, 298 (1977)
V.Gribov, L.Lipatov, *Deep Inelastic E P Scattering In Perturbation Theory*, Sov. J. Nucl. Phys. **15**, 438 and 675 (1972)
L.Lipatov, *The Parton Model And Perturbation Theory*, Sov. J. Nucl. Phys. **20**, 94 (1975)
Y.Dokshitser, *Calculation Of The Structure Functions For Deep Inelastic Scattering And E+ E- Annihilation By Perturbation Theory In Quantum Chromodynamics. (In Russian)*, Sov. Phys. JETP **46**, 641 (1977)

[16] E.A.Kuraev, L.N.Lipatov, V.S.Fadin, *Multi - Reggeon Processes In The Yang-Mills Theory*, Sov. Phys. JETP **44**, 443 (1976); E.A.Kuraev, L.N.Lipatov, V.S.Fadin, *The Pomeranchuk Singularity In Nonabelian Gauge Theories*, Sov. Phys. JETP **45**, 199 (1977); I.I.Balitzki, L.N.Lipatov, *The Pomeranchuk Singularity In Quantum Chromodynamics*, Sov. J. Nucl. Phys. **28**, 822 (1978)

[17] M.Ciafaloni, *Coherence Effects In Initial Jets At Small Q**2 / S*, Nucl. Phys. B**296**, 49 (1988);
S.Catani, F.Fiorani, G.Marchesini, *CD Coherence In Initial State Radiation*, Phys. Lett. B**234**, 339 (1990) and Nucl. Phys. B**336**, 18 (1990)

[18] L.M.Jones, H.W.Wyld, *A Measurement of Beauty Production in High-Energy Positron-Proton Scattering*, Phys. Rev. D**17**, 759 (1978)

[19] I.Bloch, *Measurement of beauty production from dimuon events at Hera/Zeus* PhD thesis

[20] C.Peterson, D.Schlatter, I.Schmitt, P.M.Zerwas, *Scaling Violations In Inclusive E+ E- Annihilation Spectra*, Phys. Rev. D**27**, 105 (1983)

[21] D.Buskulic *et al*., ALEPH Collab., *Measurement of the effective b quark fragmentation function at the Z resonance*, Phys. Lett. B**357**, 699 (1995)

[22] B.Andersson, G.Gustafson, B.Sonderberg, *A General Model For Jet Fragmentation*, Z. Phys. C**20**, 317 (1983)
T. Sjöstrand, Nucl. Phys. 248 469 (1984).

[23] S.Catani, Dokshitzer, L.Yuri, B.R.Webber, *The K-perpendicular clustering algorithm for jets in deep inelastic scattering and hadron collisions*, Phys. Lett. B**285**, 291-299 (1992);
S.Catani, Dokshitzer, L.Yuri, B.R.Webber, *Longitudinally invariant K(t) clustering algorithms for hadron hadron collisions*, Nucl. Phys. B**406** 187-224 (1993)

[24] H1 Collab., C. Adloff et al., Z. Phys. C **72**, 593 (1996);
ZEUS Collab., J. Breitweg et al., Phys. Lett. B **407**, 402 (1997);
H1 Collab., C. Adloff et al., Nucl. Phys. B **545**, 21 (1999);
ZEUS Collab., J. Breitweg et al., Eur. Phys. J. C **12**, 35 (2000);
H1 Collab., C. Adloff et al., Phys. Lett. B **528**, 199 (2002);
ZEUS Collab., S. Chekanov et al., Phys. Rev. D **59**, 012004 (2004).

[25] H1 Collab., A. Aktas et al., Eur. Phys. J. C **40**, 349 (2005);
H1 Collab., A. Aktas et al., Eur. Phys. J. C **45**, 23 (2006).

[26] ZEUS Collab., S. Chekanov et al., Phys. Rev. D **67**, 012007 (2003).

[27] A.D. Martin et al., Eur. Phys. J. C **39**, 155 (2005).

[28] S. Kretzer et al., Phys. Rev. D **69**, 114005 (2004).

[29] R.S. Thorne, Phys. Rev. D **73**, 054019 (2006).

[30] ZEUS Collab., *The ZEUS Detector, Status Report 1993*, U. Holm ed. (1993).

[31] HERA - *A proposal for a large electron-proton colliding beam facility at DESY*, report DESY HERA 81/10, July 1981.

[32] G. Ingelman, A. De Roeck, R. Klanner, Proceeding of the Workshop *Future Physics at HERA*, DESY (1995-1996).

[33] U. Schneekloth, DESY-HERA-98-05.

[34] D. Bailey et al., *Study of beam-induced backgrounds in the ZEUS detector from 2002 HERA running* (unpublished), 2002, available on $http://www-zeus.desy.de/\ kuze/zeusbg/$. ZEUS-Note 02-018.
D. Bailey et al., *Study of beam-induced backgrounds in the ZEUS detector from 2002 HERA running* (*Addendum 1*) (unpublished), 2002, available on $http://www-zeus.desy.de/\ kuze/zeusbg/$. ZEUS-Note 02-020. D. Bailey et al., *Study of beam-induced backgrounds in the ZEUS detector from 2002 HERA running* (*Addendum 2*) (unpublished), 2003, available on $http://www-zeus.desy.de/\ kuze/zeusbg/$. ZEUS-Note 02-027.

[35] DESY HERA 81-10 (81, REC. AUG.) 292p.

[36] M. Seidel, DESY HERA-00-01.

[37] B. Parker et al., *HERA Luminosity Upgrade Superconducting Magnet Production at BNL*, BNL-68284.

[38] E. Hilger, *Zeus Coordinate System*, ZEUS-Note 86-17.

[39] N. Harnew et al., Nucl. Instr. Meth. A279 290 (1989).
B. Foster et al., Nucl. Phys. Proc. Suppl. B32 81 (1993).
B. Foster et al., Nucl. Instr. Meth. A338 254 (1994).

[40] R. Hall Wilton et al., *The CTD Tracking Resolution* (unpublished), ZEUS-Note 99-024 (1999).

[41] E. Maddox, *Study of heavy quark production at HERA using the ZEUS miccrovertex detector*, PhD thesis (2004).

[42] K. Kleinknecht, *Detectors for particle radiation*, Cambridge Press.

[43] ZEUS Collab., J. Breitweg et al., Eur. Phys. J. C18 625 (2001).

[44] M. Derrick et al., Nucl. Instr. Meth. A309 77 (1991); A. Andersen et al., Nucl. Instr. Meth. A309 101 (1991); A. Caldwell et al., Nucl. Instr. Meth. A321 356 (1992);

[45] A. Berstein et al., Nucl. Instr. Meth. A336 23 (1993).

[46] A. Barbenger et al., Nucl. Instr. Meth. A382 419 (1996).

[47] H. Bethe and W. Heitler, Proc. Roy. Soc. Lond. A146 83 (1934).

[48] J. Andruszkow et al., Acta Phys. Polon B32 2025 (2001).

[49] S.M. Fisher, P. Palazzi, *ADAMO Reference Manual for Version 3.3*. CERN ECP, available on: $http://adamo.web.cern.ch/Adamo/refmanual/Document.html$.

[50] ZEUS Collab., M. Derrick et al., Phys. Lett. B297 404 (1992).
ZEUS Collab., M. Derrick et al., Phys. Lett. B322 287 (1994).

[51] A. Garfagnini, *The ZEUS Micro Vertex Detector*, Nucl. Instr. and Meth. A435 34 (1999).

[52] V. Chiochia, *Measurement of beauty quark production in deep inelastic scattering at HERA*, DESY-THESIS-03-031.

[53] C. Coldewey, Nucl. Instr. and Meth. A447 44 (2000).

[54] M. Feuerstack-Raible, *Overview of microstrip readout chips*, Nucl. Instr. and Meth. A447 (2000), procedings VERTEX 99;
W. Fallot-Burghardt et al., *HELIX! User Manual V2.1*, 03/02/1999, HD-ASICS-33-0697.

[55] A. Polini, *apblib: an Event Building and Buffering Package for the Microvertex and Global Tracking Trigger Online Environment*, ZEUS-Note 04-021.

[56] B. West, *Charm and the Virtual Photon at HERA and a Global Tracking Trigger*, PhD thesis (2001).

[57] V. Chiochia, Nucl. Instr. Meth. A501 60 (23).

[58] J.C. Collins, D.E. Soper and G. Sterman, Nucl. Phys. B308 833 (1988).

[59] G. Marchesini et al., Comp. Phys. Comm. 67 465 (1992).

[60] G. A. Schuler, Nucl. Phys. B299 21 (1988).

[61] D. Amati and G. Veneziano, Phys. Lett. B83 87 (1979);
Yu. L. Dokshitzer and S.I. Troian, Leningrad Nuclear Physics Institute preprint N922 (1984);
Ya. I. Azimov et al., Phys. Lett. B165 147 (1985), Z. Phys. C27 65 (1985).

[62] *The ZEUS Detector Status Report 1993*, DESY 1993.

[63] R. Brun, *Geant 3.13*, CERN DD/EE/84-1 (1987).

[64] W.A. Bardeen et al., Phys. Rev. D18 3998 (1978).

[65] C.F. Von Wezsaecker, Z. Phys. 88 612 (1934);
E.J. Williams, Phys. Rev. 45 729 (1934).

[66] H.L. Lai et al., Eur. Phys. J. C12 375 (2000).

[67] S. Frixione et al., Nucl. Phys. B412 225 (1994).

[68] Z. Shi, D. J. Kouri, G.W. Wei, D. K. Hoffman, Computer Physics Communications 119 (1999) 194-218

[69] T. Sjöstrand, Proceedings del Workshop *Physics at HERA*, vol.3, Hamburg 1991, 1405

[70] `http://www-zeus.desy.de/components/funnel/MONTE_CARLO/mozart.html`

[71] H. Jung, Comp. Phys. Comm. 86 (1995) 147.

[72] H. Jung, *The RAPGAP Monte Carlo for Deep Inelastic Scattering*,

[73] G.A.Schuler, H.Spiesberger, Physics at HERA proceedings **3**, 1419 (1991)
version 2.08/01, `http://www-h1.desy.de/jung/rapgap.html`.

[74] A. Kwiatkowski, H. Spiesberger, H.-J. Mohring, *HERACLES 4.1 – An event generator for ep interactions at HERA including radiative processes*, in Proc. of the Workshop on Physics at HERA, Vol. 3, edited by W. Buchmuller, G. Ingelman (1991), p. 1294.

[75] A. Kwiatkowski, H. Spiesberger, H.-J. Mohring, *HERACLES – An event generator for ep interactions at HERA including radiative processes*. version 4.6, 1996,
`http://www.desy.de/\~hspiesb/heracles.html`.

[76] L. Adamczyk et al., *Luminosity measurement in the ZEUS experiment*, ZEUSNOTE 01-004.

[77] H.Abramowicz, A.Caldwell, R.Sinkus, *Neural Network Based Electron Identification in the ZEUS Calorimeter*, DESY 95-054. R.Sinkus, Nucl. Instrum. Methods **A361** (1995) 290.

[78] ZEUS Collab., M. Derrick et. al., Phys. Lett. B384 401 (1996).

[79] H1 Collab., A. Aktas et al., hep-ex/050210.

[80] ZEUS Collab., S. Chekanov et al., Phys. Lett. B599 173 (2004).

[81] B.W. Harris and J. Smith, Phys. Rev. D57 2806 (1998).

[82] H. Jung, Comput. Phys. Commun. 86 147 (1995).

[83] H1 Collab., DESY 06-039.

[84] H. Jung and G.P. Salam, Eur. Phys. J. C19 351 (2001).

[85] T.Sjostrand *et al.*, *High-energy-physics event generation with PYTHIA 6.1*, Comput. Phys. Commun. **135**, 238 (2001)

[86] L.Lönnblad, *ARIADNE version 4: A Program for simulation of QCD cascades implementing the color dipole model*, Comp. Phys. Commun. **71**, 15 (1992)

[87] *HECTOR 1.00 - A Program for the Calculation of QED, QCD and ElectroweakNeutral and Charged Current Scattering*, A. Arbuzov *et al.* hep-ph/9511434

[88] H1 Collab., A. Aktas et al., Phys. Lett. B621 56 (2005).

[89] G. Hartner, *VCTRAK: Offline Output Information*, ZEUS-Note 97-064.

[90] G. Hartner, *VCTRAK: ZEUS Track & Vertex Reconstruction*, 15.07.200.

[91] G. Hartner,*VCTRAK Briefing: Program & Math*, ZEUS-Note 98-058.

[92] G. Hartner, private communication.

[93] S. Miglioranzi, *Sviluppo di algoritmi per la misura della produzione di quark b all'esperimento ZEUS ad HERA* (in Italian), Diploma thesis, Bologna University (2002).

[94] G.M. Briskin, *Diffractive Dissociation in ep Deep Inelastic Scattering*, DESY-THESIS 1998-036.

[95] J. Huth et al., *Proceedings of the PDF Summer Study on High Energy Physics*, 1990, ed. L. Berger, 134 (1992).

[96] S. Catani, Yu.L. Dokshitzer and M.H. Seymour, Phys. Lett. B285 291 (1992).

[97] S. Catani et al., Nucl. Phys. B406 186 (1993).

[98] A. Bassetto, M. Ciafaloni and G. Marchesini, Phys. Rep. 100 202 (1983);
Yu.L. Dokshitzer et al., *Basics of perturbative QCD*, Ed. Frontieres, Gif-Sur-Yvette, 1991.

[99] T. Namsoo, *Three- and Four-Jet States in Photoproduction at HERA*, PhD thesis (2005).

[100] V. Innocente, M. Maire and E. Nagy, *GEANE: average tracking and error propagation package*, proceedings of MC91: Detector and event simulation in High Energy Physics, Amsterdam (1991).

[101] R. E. Kalman, Transaction of the ASME-Journal of Basic Engineering 82 35 (1960);
R. Fruhwirth, Nucl. Instr. Meth. A262 444 (1987).

[102] G. F. Hartner et al., *VCTRAK(3.07/04): Offline Output Information*, ZEUS-Note 97-064.
G.F Hartner, *VCTRAK Briefing: Program and Math*, ZEUS-Note 98-058.

[103] R. Sinkus, H. Abramowicz and A. Caldwell, Nucl. Instr. and Meth. A365 508 (1995).

[104] F. Jaquet and A. Blondel, *Proceedings of the Study of an ep facility for Europe*, Ed. U. Amaldi, DESY 79/48, 391.

[105] V. Kuzmin, Nucl. Instr. Meth. A435 (2000) 336.

[106] E. Maddox, *Study of heavy quark production at HERA using the ZEUS microvertex detector* (unpublished). Amsterdam preprint, December 2004.

[107] E. Maddox *A Kalman filter track fit for the ZEUS mirovertex detector*, ZEUS-Note 03-008 (2003).

[108] U. Schneekloth *HERA Report*, talk ZEUS Collaboration Meeting, Padova October 2004.

[109] G. D'Agostini, *Bayesian Reasoning in High Energy Physics: Principles and Applications*, CERN Yellow Report CERN-99-03.

[110] M. Turcato, *Measurements of beauty photoproduction at HERA*, DESY-THESIS-03-039.

[111] R. Mankel, ZEUS Phys. Coord. talk (internal page), 07-02-2006.

[112] S. Miglioranzi *beauty production at* HERA *II with the* ZEUS *experiment*, PhD thesis (2006).

[113] Physics Letters B **599** (2004) 173-189

[114] A. Longhin, *Misura delle sezioni d'urto di fotoproduzione di Open Beauty ad HERA*. (In Italian, unpublished). Diploma Thesis Padova University (2000)

[115] M. Turcato, *Measurement of beauty photoproduction at HERA* (unpublished), DESY-THESIS-2003-039.

List of Figures

List of Tables

Ringraziamenti

Trovo doveroso ringraziare anzitutto i miei mentori e maestri.
Il Prof. Riccardo Brugnera, che sedendosi mille volte al mio fianco con pazienza e affabilità mi ha instillato quella proficienza che lo ha reso un sì noto luminare, e trasmesso molta parte delle conoscenze che lo han portato a librarsi alto nell'olimpo della scienza.
Poi Alessandro Bertolin, che mi ha accompagnato dalla tesi di laurea a quella di dottorato, glissando con benevolenza sui miei limiti ed aiutandomi a spostarli un pò più in là. Il suo approccio aggressivo ed audace ;-p all'analisi ha consentito di raggiungere risultati certi in tempi brevi.
Debbo poi enorme gratitudine a due meravigliose donne, senza le quali questo lavoro non avrebbe mai potuto giungere al termine: Monica e Silvia, l'altra metà del cielo di DESY. La loro *materna* dolcezza mi è stata d'aiuto quasi quanto le loro conoscenze.
Un grazie anche a Massimo Corradi, che non ha mai negato una parola ad un pollo di un altro ovile. Con lui ringrazio anche tutti i membri del *Heavy Flavour Group*, ed in particolar il suo benamato leader Achim (thank you Achim!), per gli stimoli e le discussioni. Grazie anche a Elisabetta, a lungo *first lady* di ZEUS, per aver apprezzato in maniera tangibile il mio lavoro (EPS!).
Un enorme grazie a tutti la ghenga di canaglie di DESY: Lorenzo, Marcello, Michele, Salvatore. Con loro, ed assieme a molti altri che sarebbe troppo lungo menzionare, il soggiorno in terra tedesca è stato sempre lieto. Più che amici, son stati una famiglia per me, e di certo tali resteranno.
Devo ancora una volta ringraziare Luca Stanco, grazie al quale son diventato mio malgrado un quasi–esperto *hardware*, un navigato *shift leader*, grazie a cui i foglietti gialli arrivavano con periodicità, e grazie al quale almeno per i prossimi due anni non sarò disoccupato.
Infine, ma sopra tutto e tutti, ringrazio mia madre, che mi ha sempre guidato col suo esempio e la sua forza d'animo, e le cui *conoscenze altolocate* mi sospingono sempre come una brezza leggera: le preci che volge a Dio per me infatti non mancan mai di venir ascoltate.